Universitat Politècnica de Catalunya

Departament de Física i Enginyeria Nuclear
Institut de Tècniques Energètiques

First measurement of β-decay half-lives and neutron emission probabilities in several isotopes beyond N = 126

(Revised edition October 2015)

Author:
Roger Caballero-Folch

Supervisors:
Dr. César Domingo-Pardo
Dr. Guillem Cortès Rossell

Barcelona, Abril de 2015
Programa de Doctorat: Enginyeria Nuclear i de les Radiacions Ionitzants
Tesi presentada per obtenir el títol de Doctor per la Universitat Politècnica de Catalunya

Resum

En aquest treball s'han determinat, experimentalment i per primera vegada, vides mitjanes i valors de probabilitat d'emissió de neutrons de diversos nuclis amb més de 126 neutrons. Per tal d'obtenir les dades es va realitzar un experiment a les instal·lacions del centre d'investigació d'ions pesats GSI a (Alemanya), combinat amb el separador de fragments FRS. El sistema de detecció d'ions i desintegracions β va consistir d'un detector de partícules carregades anomenat SIMBA, que estava envoltat per una matriu de comptadors proporcionals d'^{3}He que conformen el detector de neutrons BELEN. En total s'han determinat valors de vida mitjana de divuit isòtops d'or, mercuri, tal·li, plom i bismut, així com també la probabilitat d'emissió de neutrons (o llindars superiors) de set d'ells. Comparant els resultats amb les mesures de vides mitjanes anteriors en aquesta regió de nuclis s'observa un bon acord, reflectint la validesa de la sistemàtica de les dades existents. D'altra banda, fent la comparació amb els models teòrics, els resultats mostren un acord raonable per la meitat dels isòtops analitzats, i grans discrepàncies, de fins a un factor 10, per l'altra meitat. Pel que fa a les probabilitats d'emissió de neutrons mesurades, essent la primera mesura experimental a la regió per a diversos nuclis, no és possible comparar amb altres els valors obtinguts. La única comparació que es pot avaluar és amb les prediccions teòriques. En resum, els resultats són compatibles amb el model FRDM + QRPA, no obstant s'observen discrepàncies considerables en alguns isòtops de fins a un factor 5, com és el cas del valor obtingut per ^{215}Tl, que correspon al nucli més exòtic del qual s'ha determinat la probabilitat d'emissió de neutrons.

Abstract

In this work β-decay half-lives and neutron-emission probability values have been experimentally determined for first time in several nuclei beyond the neutron-shell closure at N=126. To this aim the accelerator complex at the GSI center for heavy ion research (Germany), in combination with the FRS fragment separator, were employed. The β-decay detection system consisted of a charged particle detector named SIMBA, which served to detect both ion- and β-particles, surrounded by an array of ^{3}He-based neutron counters named BELEN. The half-life values of eighteen isotopes of Au, Hg, Tl, Pb and Bi were determined, as well as the neutron-branching ratios (or upper limits) for seven nuclei. A comparison of the present results with previous half-life measurements in this mass-region shows a generally good agreement, thus reflecting the systematic validity of the decay data available in this region. Compared to theoretical models, our results show a reasonable agreement for half of the analyzed isotopes, and large discrepancies of up to a factor of 10 for the other half. The measured neutron-branching ratios represent the first set of experimental data available in this mass-region for several isotopes. Owing to the absence of previous experimental results, the values reported here can be only compared with theoretical predictions. In summary, a fair compatibility is found between FRDM+QRPA calculations, which however are underestimating by a factor of 5 the neutron-branching ratio of ^{215}Tl, which is the most exotic nucleus measured in this work.

KEYWORDS: β-delayed neutron emission, β-decay half-life, r-process, nucleosynthesis, nuclear structure, neutron detector.

En primer lloc, sóc un home; després, un artista. Com a home, la meva primera obligació és lluitar pel benestar de la humanitat. Intentaré d'acomplir aquesta obligació mitjançant la música -aquest do que Déu m'ha atorgat-, perquè ultrapassa tota frontera lingüística, política i nacional. La meva contribució a la pau del món pot ésser minsa, però hauré donat tot el que puc per aconseguir un ideal que considero sagrat.

First of all, I am a human; later, an artist. As a human, my first duty is to fight for the welfare of humanity. I will try to fulfill this obligation through music -a gift granted by God- because it transcends all linguistic border, politics and nations. My contribution to world peace may be scarce, but I have given everything I could to get what I considered sacred ideals.

Pau Casals
(El Vendrell 1876 - San Juan de Puerto Rico 1973)

Als meus Pares i l'Ari,
a la Sònia i al Martí

Acknowledgments

Al final d'un treball com aquest hi ha molta gent a qui agrair la seva contribució. Algunes persones han format part de l'equip que l'ha fet possible i han aportat coneixements que han enriquit el seu contingut, altres senzillament han donat un recolzament vital i imprescindible. Probablement em deixaré molta gent i des d'aquest primer paràgraf ja els demano disculpes.

En primer lloc vull agrair a tots aquells professors que han permès que aquest treball s'hagi pogut realitzar. Als membres del grup GRETER de la SEN per haver-me permès poder formar part del projecte [1] i, en especial, al codirector d'aquesta tesi i company de viatges arreu del món, el Guillem Cortès. A més també vull agrair la concessió de la beca associada a la Càtedra Argos del Consejo de Seguridad Nuclear (CSN) durant els dos primers anys de la tesi i, molt especialment, al Departament de Física i Enginyeria Nuclear (DFEN) per l'aval d'aquesta beca pels dos anys restants. A l'INTE per la possibilitat de prorrogar sis mesos més la beca i pels mitjans tècnics i humans que he tingut a disposició.

També vull agrair el suport del grup d'espectrometria gamma de l'Institut de Física Corpuscular de València. Ells han donat sentit als experiments que he pogut participar activament, i la crítica necessària per aconseguir desxifrar una informació encriptada en unes dades molt enigmàtiques. En especial a José Luis Taín, Alejandro Algora i a tot el grup, Berta, Kike, Ana, Ebhelixes, Loli, Bill, Sonja, Ela, Víctor i a l'amic i company de travesses i calçotades, el capità Jorge Agramunt. Ep! i sense oblidar també l'amic EUROMED!

I would also thank to the technical staff of the GSI accelerators for their support during the experimental campaign. And particularly all the collaborators who participated in the S410 experiment [2] between summer and autumn 2011, specially doctors Karl Smith, Michele Marta, Fernando Montes, Alfredo Estrade and Ian Kurcewicz. Also thanks to Dr. Iris Dillmann for her hospitality during the stays at GSI and for her patience and commitment that will allow me to continue in this world of science.

Also thanks to other colleagues met during these years in experiments and

[1] This work has been partially supported by the Spanish Ministry of Economy and Competitivity under grants FPA 2011-28770-C03-03, CSD200700042, FPA200804972C0303, AIC-D-2011-0705, FPA2011-24553 and FPA2008-6419.

[2] This experiment was also supported by the European Community FP7 - Capacities, contract ENSAR num 262010 and by the Helmholtz Association via the Young Investigators Project VH-NG 627 (LISA- Lifetime Spectroscopy for Astrophysics).

conferences I attended, specially people from IGISOL facility of Jyväskylä (Finland), the group of Universidade de Santiago de Compostela for the Euroschool 2010 and their support, and the fellowships obtained from several institutions to attend schools such as the Nuclei in the Cosmos satellite school in Canberra (Australia) in 2012, the International Scientific Meeting on Nuclear Physics. La Rábida 2012, Huelva (Spain) and the Nuclear Structure 2014 in Vancouver (Canada).

Finally I would like to specially mention the person who made possible this experiment and this analysis. Thanks to him I felt supported to follow with this complex labyrinth of data and to finish a thesis that sometimes I have not seen clear. His character and the passion for the field of work helped me to be centered and open my mind in many occasions when necessary. César moltes gràcies per la teva aportació i per la paciència.

La ciència ha estat part important de la meva vida durant aquests anys, però, des d'una vessant més humana, també vull dir que no tot allò que ha succeït durant la tesi ha sigut física i nuclis. Probablement són coses molt extranyes per a moltes persones amb les quals convivim el dia a dia. En primer lloc, els viatges han estat molt freqüents i han suposat un esforç, però l'enriquiment que m'han donat penso que és una de les coses més importants que m'emporto. També hi ha hagut moltes estones entrenyables, recordaré sempre les tertúlies de l'hora del dinar: des de les aventures que explicava un rus anomenat Vitaly (ja doctor!) als desapareguts menjadors universitaris, fins a les dels darrers anys als esmorzars de la facultat de física i a la taula rodona del menjador del soterrani de l'INTE. Les trifulkes quotidianes han format part d'aquest dia a dia i, amb la Maria, la M.Amor, la Sonia, la Natàlia (amb casament inclòs), l'Alex, l'Albert, el Juan Antonio, la Isa, l'Antonia, la Maria Carme i l'entrenyable Vicente, han estat força amenes. Tot, amb converses que intenten fugir de la política però que amb uns bons calçots o unes gambes s'empassen molt millor.

Tinc també un especial record dels dies que anava a dinar a l'Hospital Infantil de Sant Joan de Déu amb l'Esther i la Maria. Una experiència familiar molt dura que probablement també m'hagi ensenyat moltes de les coses que no estan a l'ordre del dia d'una feina com la de fer un doctorat i que són una realitat que pot tocar molt de prop.

I finalment als qui han sofert de prop tot aquest calvari que suposa una tesi tan llarga. Alguns preguntant-se "per a què serveixen totes aquestes coses rares que estàs fent" i, d'altres que entenen perfectament certs estats d'ànim, ja sigui d'eufòria o de caiguda, per reciprocitat. És amb la Sònia amb qui hem patit més el túnel del final que mai arriba i cal reconèixer l'esforç i valorar la paciència. Suposo que el qui ho ha entès millor tindrà clar que seguir posant una rialla en qualsevol moment és garantia de felicitat als qui l'envolten. Als pares i l'Ari, a la Sònia i al Martí!

Thanks, Gracias, Danke, Kiitos, Merci, Gràcies!

Contents

List of Figures

List of Tables

Chapter 1

Introduction

1.1 Motivation

The discovery of the elements and their isotopes has been a successful challenge along the XX^{th} Century, specially since the discovery of radioactivity by Becquerel in 1896 [2]. At present about 3000 isotopes are known and recent calculations estimate that about 7000 isotopes are bound with respect to neutron and proton emission [3]. In order to improve the knowledge of their properties it becomes necessary to produce them artificially in very specific Rare Isotope Beam (RIB) facilities and to interpret the measured quantities on the basis of theoretical models. There exist several RIB facilities in the world and some of them are being upgraded in order to increase their possibilities of nuclei production.

Nowadays, part of the nuclear physics studies are intended to push further the limits of knowledge towards more exotic nuclei with the aim of determining their physical properties. For very exotic neutron-rich nuclei, half-lives ($T_{1/2}$) and β-delayed neutron emission probability (P_n) are often the only decay properties that can be experimentally obtained due to the very low production cross sections. Such data provide an important contribution to nuclear structure investigations, specially in those regions where other measurements, such as γ-ray spectroscopy, are not possible with present facilities and technology. The decay properties of neutron-rich nuclei far from stability have also a direct impact in nucleosynthesis studies, such as the rapid neutron capture process (r-process). Finally, β-delayed neutrons of fission products produced in nuclear power plants play an important role in the design and operation of nuclear reactors. β-delayed neutrons enhance the effective lifetime of free neutrons in the reactor core, thus making it feasible to adjust the criticality conditions in human timescales.

Theoretical models have been developed on the basis of experimental data of nuclei at or near the valley of stability and, therefore, cannot describe precisely the properties of nuclei far from stability. So far, there is no P_n data reported in the region around $N = 126$, except the only experimental value available for ^{210}Tl, measured in 1961 [4, 5]. Previous experimental studies focused mainly on the light nuclei and the fission-products, up to $A \approx 150$, which can be produced with relatively high yields [6, 7].

1.1.1 β delayed neutron emission

The β-delayed neutron emission is a decay mode of neutron-rich nuclei. It occurs when the disintegration of a precursor nucleus via β-decay is followed by the emission of a neutron by the daughter nucleus instead of only γ-rays (see figure 1.1). The mechanism for this process was originally proposed by [8] and reported by [9] in 1939.

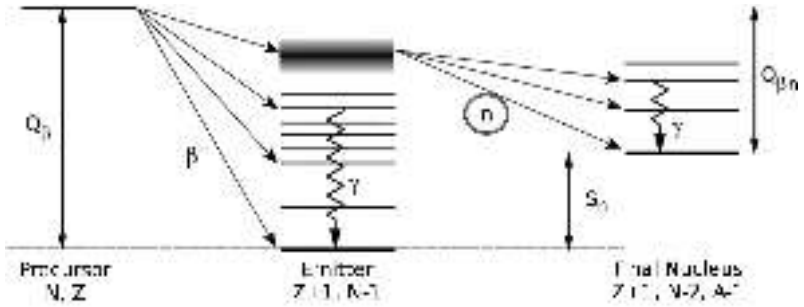

Figure 1.1: β-delayed neutron emission scheme.

This phenomenon is energetically allowed if the β-decay populates an excited state higher than the bounding energy S_n of a neutron in the the daughter nucleus. Therefore, the maximum energy associated to the emitted neutron is defined as $Q_{\beta n} = Q_\beta - S_n$, which must be positive for the process to be allowed, being the Q_β the maximum β-decay energy of the precursor. Normally, the neutron emission probability, P_n, increases when Q_β-values are larger and the S_n-values smaller, however, high energy neutrons are rather suppressed due to the Fermi function.

Today more than 200 β-delayed neutron emitters have been measured [10]. When Q_β is larger than the separation energy ($S_{2n,3n,\ldots}$) for the emission of $2, 3, \ldots$ neutrons, two or more neutrons can be emitted after a β-decay ($\beta 2n$,$\beta 3n$,...). Such exotic multiple neutron emission was first observed in 1979 [11] but so far only eighteen $\beta 2n$ emitters have been measured [12]. Out of them, there are only three $\beta 2n$ emitters heavier than iron: ^{86}Ga [13], ^{98}Rb [14] and ^{100}Rb [15]. Given this situation, it becomes difficult to test the performance of theoretical models in terms of βn-to-$\beta 2n$ competition, particularly towards the heavy mass region.

1.2 Nuclear structure

The half-lives and neutron branching ratios provide relevant information about the structure of nuclei determining the β-decay [1]. These are usually the first properties accessible to experimental studies for new discovered isotopes

far from stability, providing, together with the Q_β and S_n values, relevant characteristics about the r-process path. The two decay gross properties of half-life ($T_{1/2}$) and β-delayed neutrons (P_n) are integral quantities of the β-strength function S_β [16]. Thus, $T_{1/2}$, which is defined as

$$\frac{1}{T_{1/2}} = \sum_{0 \leq E_i \leq Q_\beta} S_\beta(E_i) \times f(Z, R, Q_\beta - E_i) \tag{1.1}$$

provides information about the average β-feeding over the entire Q_β-window. In the latter expression f(Z,R,Q_β-E_i) is the Fermi function.

The second main decay "Gross Property", the β-delayed neutron emission probability (P_n), is defined by the ratio of integrals,

$$P_n = \frac{\sum_{S_n}^{Q_\beta} S_\beta(E_i) \times f(Z, R, Q_\beta - E_i)}{\sum_{0}^{Q\beta} S_\beta(E_i) \times f(Z, R, Q_\beta - E_i)} \tag{1.2}$$

Thus, in a similar manner as $T_{1/2}$ provides information on the average β-feeding over the full energy window of the decay, P_n yields information on the integral β-feeding above the neutron separation energy, which means, at high excitation energies in the daughter nucleus.

Finally, by combining both integral quantities, $T_{1/2}$ and P_n, one can infer valuable information about the rough shape, the hardness or the softness, of the β-strength distribution.

One of the most common theoretical model is the one which combines the Finite-Range Droplet-Mass (FRDM) model with the Quasi-Particle Random-Phase Approximation (QRPA) [1]. Perhaps the main advantage of the FRDM + QRPA model is the fact that it can be applied to calculate ground state and decay properties of almost any nucleus in the nuclear chart. Thus, properties for 8979 nuclei beyond ^{16}O are reported in [17], which is of great help for both experimental and theoretical studies. This model uses the FRDM model to predict nuclear masses and other quantities required for the calculation of half-lives and β-delayed neutrons such as Q_β and S_n-values [18]. The Gamow-Teller (GT) part of the β-strength distribution is obtained in the framework of the QRPA, whereas First-Forbidden (FF) transitions are added on top of it by using the "Gross Theory" [19, 20]. If the shape of the ground state is known, nuclear deformation can be also taken into account in the calculation of $T_{1/2}$ and Pn-values [1].

More recent theoretical studies employ the DF3 density functional in combination with continuum QRPA (cQRPA) [21,22] in order to include consistently both GT and FF transitions. Unfortunately, this model has not been applied over such a large number of nuclei as the FRDM + QRPA, but it is expected to incorporate more reliably the contribution of FF-transitions in the β-strength distribution.

There are also empirical parametrizations of the β-delayed neutron emission probability, also called phenomenological models. The latter use experimentally known properties, such as the half-life [23] in order to parameterize the neutron branching ratio. The most recent contribution to this model [24] makes use of level-density functions to model β-delayed neutrons using different mass ranges. However, the absence of an underlying microscopic model casts doubts on the extrapolability far from stability, particularly in the $N \approx 126$ mass region, where no parametrization was possible owing to the absence of P_n data in this region.

For heavy nuclei Shell Model calculations are restricted to regions at or around the shell closures. This model accounts for allowed Gamow-Teller (GT) and first-forbidden (FF) transitions in a self consistent way. Thus, it is expected that Shell Model-calculations provide rather reliable $T_{1/2}$ and P_n predictions at and near the neutron and/or proton shell closures. This has been indeed confirmed for light to medium-heavy nuclei [25,26] in the regions where experimental data is available.

1.3 Astrophysics calculations. R-process nucleosynthesis

The nucleosynthesis of the elements in the Universe includes several processes which convert the elementary hydrogen and helium to heavier elements. Fusion reactions in the stars produce the elements up to the iron peak, starting from the burning of light elements in several nuclear processes such as the p-p chain, CNO cycles, helium burning and heavy element fusion. Beyond iron ($A >56$) fusion reactions are not possible energetically and mainly another nucleosynthesis mechanism starts. Depending on the strength of the neutron source in the stellar environment, one can distinguish between the slow neutron-capture process (s-process) and the rapid neutron-capture process (r-process) in regions with low and high neutron density, respectively [27].

All these processes make possible to understand the existence and the abundance of the chemical elements in the Solar System and in other stars. Figure 1.2 [28] shows the solar abundance, detailing the astrophysical processes which are responsible of each peak observed. Currently the characterization of this abundance pattern is a challenge to explain the formation of the elements and the precise contribution of each process to it.

1.3.1 s-process

The s-process allows to understand the existence of half of the nuclei beyond iron up to ^{209}Bi and, together with other processes, is also the responsible of the synthesis of lower mass elements, such as nuclei between Na ($A = 23$) and

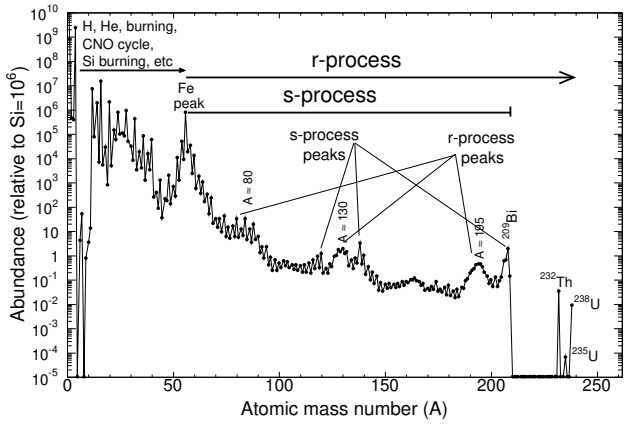

Figure 1.2: Solar abundance pattern observed and processes responsible of each peak.

Ti ($A = 46$). It occurs close to the stability valley in hydro-static stages of stellar evolution such as massive stars and low mass AGB stars. It takes a long time-scale that can span up to thousands of years for each capture and it occurs with a slow rate compared to the β-decays. This process produces the abundance peaks of $A = 90$, 138 and 208, related to the neutron shell closures at $N = 50$, 82 and 126 respectively, where the cross-section of the neutron capture is very small.

This nucleosynthesis mechanism became revealed by the observation of Tc in the atmosphere of red-giant stars [29]. Tc has no stable isotope, being ^{99}Tc the longest lived Tc-isotope with a half-life of $T_{1/2} = 2.1 \times 10^5$ years. This value is remarkably shorter than the age of such stars, thus indicating that some kind of heavy elements nucleosynthesis was happening in such stars [30, 31].

1.3.2 r-process

The r-process occurs in explosive stellar environments. The exact site of the r-process is still unknown. However, it is accepted that it comprises very high neutron density environments ($>10^{23}$ n/cm^3) and high temperatures of $T \sim 10^9$ K. Under such conditions neutron captures take place faster than β-decays and the r-process path in the nuclear chart proceeds through a chain of extremely neutron rich nuclei. Due to the large neutron separation energies at the neutron shell closures (N =50 82 and 126), the flow of matter slows down when the r-process path crosses nuclei with magic neutron numbers, thus accumulating matter at these r-process waiting points, producing the characteristic r-process abundance peaks at $A \approx 80$, 130 and 195 [27], as shown in figure 1.3. Some candidates are type II Supernova explosions and

neutron star mergers [32, 33]. The r-processes involves an enormous amount of very exotic neutron-rich nuclei and is considered the main responsible for the existence of half of the elements heavier than iron and, in particular, the unique process that explains the formation of heaviest nuclei beyond ^{209}Bi and the actinides.

Up to now, many measurements have been performed along the r-process path in the regions which give rise to the two peaks located at $A \approx 80$ and $A \approx 130$, related to magic numbers of $N = 50$ and 82 respectively. Experiments provide properties including P_n-values around the second peak at $N = 82$ [34, 35, 36, 37, 38, 39, 40]. For the third peak located at $A \approx 195$, related to the neutron shell closure of $N = 126$, there is no experimental data available. Figure 1.3 [41, 42, 43] shows the chart of nuclei with r-process path isotopes in red detailing the solar abundances peaks with their correspondence to the neutron shell closures.

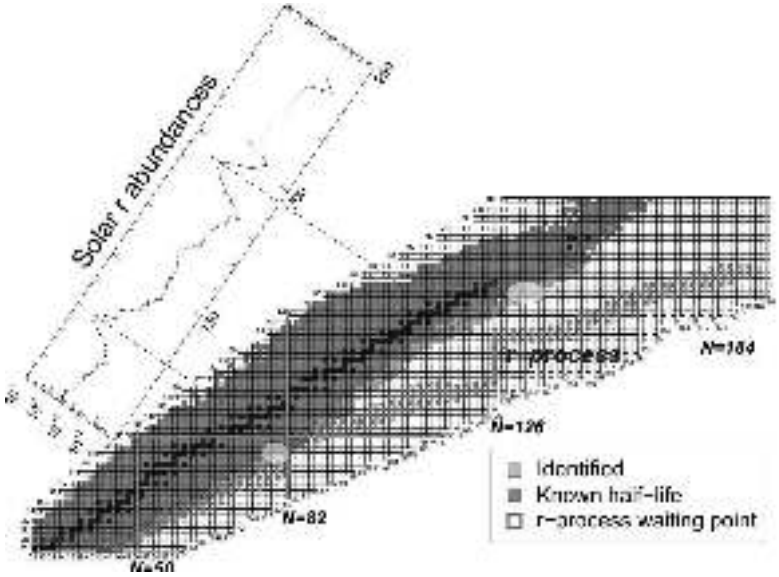

Figure 1.3: Chart of nuclei detailing stable nuclei (black), r-process path (red), those isotopes identified and those with known half-life. The r-process abundance peaks on Solar observations are associated with their correspondence neutron shell closure. The circles detail regions studied at the *Helmholtzzentrum für Schwerionenforschung GmbH* (GSI) during the experimental campaign.

Long term hydro-dynamical simulations of the neutrino driven wind which follows a Supernova explosion [44] are capable of reproducing the r-process abundances at $N = 50$ and $N = 82$. However they fail in reproducing the environment entropy necessary for the appearance of the abundance maximum

at $A \approx 195$. To which extent this is related to a bias in the calculations, or to the largely uncertain unclear physics input remains an open question. Thus, improvements in both theory and experiments are needed in order to find a proper answer.

1.3.3 P_n on r-process nucleosynthesis

As described previously, the r-process has an important role in the nucleosynthesis of heavy nuclei. In this process the β-delayed neutron emission is a common phenomenon due to the neutron-rich nuclei involved in it. It has a relevant influence in the final abundances, which are shifted towards lower isobaric distributions if considering a pure β-decay during the freeze-out of the r-process. On the other hand, it enhances the number of neutrons able to be captured during freeze-out.Therefore, the final abundance pattern reflects the contribution of these two effects, which depend on the particular neutron branching ratios of the involved nuclei.

1.4 Objectives of this thesis

This thesis consists of realization and analysis of data acquired in an experiment carried out at the GSI facility [45], in which very exotic nuclei in the neutron-rich region were produced.

The analysis aims to determine β-decay half-lives and β-delayed neutron emission probabilities (P_n) of Au, Hg, Tl, Pb and Bi isotopes, in the neutron-rich region beyond $N = 126$ [46].

1.5 Structure of this document

Chapter 2 details the experimental setup, which includes the nuclei production via fragmentation reactions and the selection and identification of the nuclei of interest. Once the isotopes have been selected, they are implanted and the decay products detected by means of the apparatus and methodology described in chapter 3. This chapter comprises the calibrations and corrections applied to both the implantation and neutron detectors and describes the characteristics of each event analyzed either implant, decay or neutron. The latter information makes possible to implement the implant-β and implant-β-neutron time-correlations for the final half-life and neutron branching analysis. This analysis is presented in chapter 4, where the half-lives and the neutron branching ratios P_n are determined. Chapter 5 covers the discussion and interpretation of the results. A comparison between the results here obtained and those from previous experiments is reported. Finally, a comparison with the main theoretical

models is also presented. Chapter 6 summarizes the main conclusions of this thesis.

Chapter 2
Experimental setup and ion identification

The main objective of this PhD-work is the experimental determination of β-decay half-lives and β-delayed neutron emission probability (P_n-values) of several neutron-rich heavy nuclei using the RIB facility of GSI, Germany.

The experiment took place in September 2011 using the high efficiency neutron detector Beta dELayEd Neutron (BELEN) detector. BELEN will be a dedicated system for neutron detection in the future Facility for Antiproton and Ion Research (FAIR). Previously to this experiment, other measurements with BELEN prototypes were successfully performed in 2009 and 2010, at the Ion Guide Isotope Separation On-Line (IGISOL) facility [47, 48] at the *Jyväskylän Yliopiston Fysiikan Laitos* (JYFL) - University of Jyväskylä (Finland), where several P_n-values of isotopes around $A \approx 85$ were measured with improved accuracy [49, 50].

The experimental proposal presented at GSI [46] included isotopes with unknown half life and the challenge to measure, for the first time, P_n-values beyond $N = 126$. Previous to the experiment, simulation tools were used to calculate and evaluate production rates for the nuclei of interest using the *Helmholtzzentrum für Schwerionenforschung GmbH* (GSI) facility accelerators [45] and the Fragment Separator (FRS) [51].

This chapter details the aspects of the experiment related to ion selection using FRS and the ion identification via the $B\rho$ - ΔE - $B\rho$ method, by means of tracking detectors.

2.1 GSI accelerator facility

The GSI facility operates a complex of acceleration systems for heavy ions and it allows the production of very exotic nuclei, which can be analyzed with a dedicated detection system. The main GSI accelerator systems comprise several devices starting with the Universal Linear Accelerator (UNILAC) which can accelerate all kind of ions up to 20% of the speed of light, with energies of 3-20 MeV per nucleon. The accelerated beam can be injected in the *Schwerionensynchrotron* SIS-18 for further acceleration, where velocities around 90% the speed of light can be achieved, which corresponds to ion energies of up to 1 GeV per nucleon [52]. The extraction of the beam from SIS-18 to FRS has the challenge to maintain the high vacuum using a special window, to avoid beam

losses [53], and to allow the beam to enter in the FRS spectrometer. Other systems such as the Experimental Storage Rings (ESR) and a number of experimental halls completes the present facility. Figure 2.1 shows the schematic view of the GSI facility and its experimental areas [45].

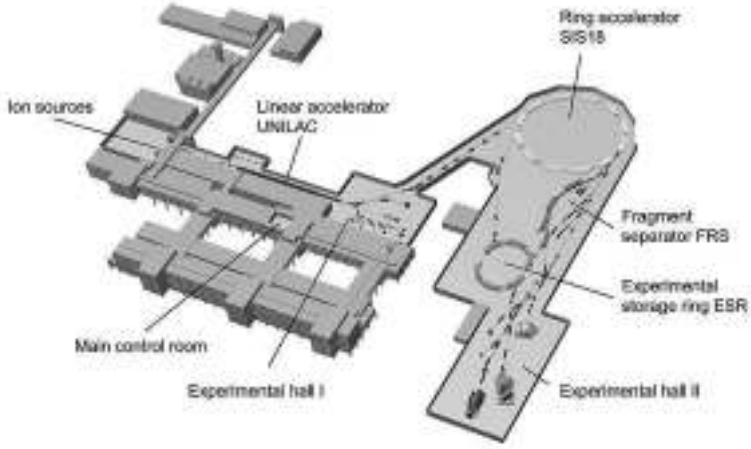

Figure 2.1: GSI facility scheme, which comprises the linear accelerator UNILAC, the SIS-18 synchrotron, the Fragment Separator (FRS), the Experimental Storage Ring (ESR) and a number of experimental halls to host the detection systems for each experiment.

2.1.1 Beam properties and structure

The characteristics of the primary beam have a direct impact in the analysis method. In this experiment the beam delivered by the synchrotron was a ^{238}U beam with an energy of 1 GeV per nucleon and an average intensity of 2×10^9 ions/spill. Its time structure consisted of spills of 1 second duration over a repetition period of 4 seconds. Thus, implantation events were detected during the spill.

As explained in the next chapter, two trigger types were used in order to indicate the start and the end of the spill during the experiment. With them, it is possible to determine if a decay event occurs inside the spill or not.

In order to show the spill structure figure 2.2 presents the amount of each type of event in a time interval during the experiment. The beam structure can be clearly identified by following the amount of neutrons (blue) detected during the spill. The distribution of decay events (red) was rather flat in time, whereas for implant events (green) the rate is very low (two implant events are observed inside the 2^{nd} and the 3^{rd} spills in the example of figure 2.2).

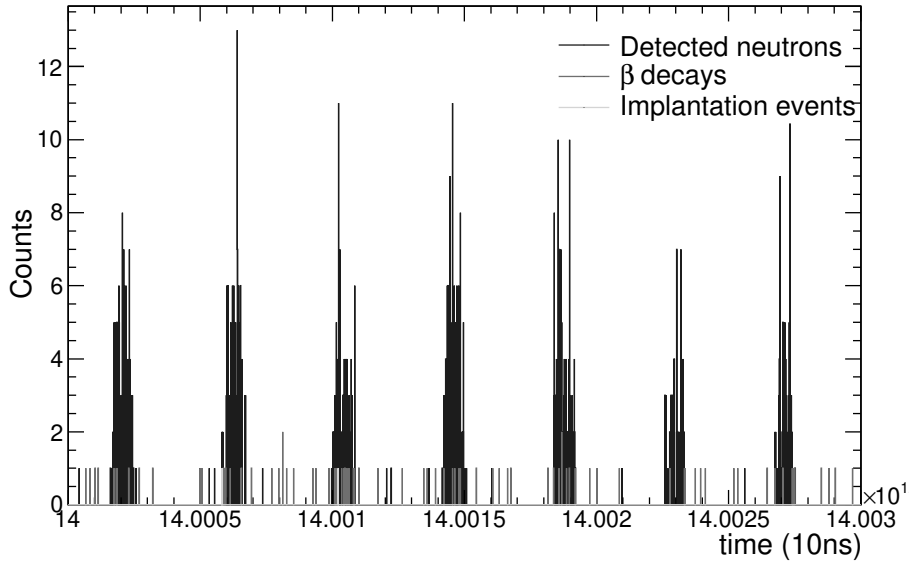

Figure 2.2: Neutron (blue), β-decay (red) and implant (green) counting rates for a random time interval during the experiment.

2.2 The Fragment Separator (FRS) facility

The FRS was used as an achromatic spectrometer. It has a length of 70 m with four 30^o dipole magnets that allow the transmission of ions of interest. Following each dipole there are quadrupoles which determine the ion-optical properties at the four focal planes S1, S2, S3 and S4 shown in figure 2.3 [51,54].

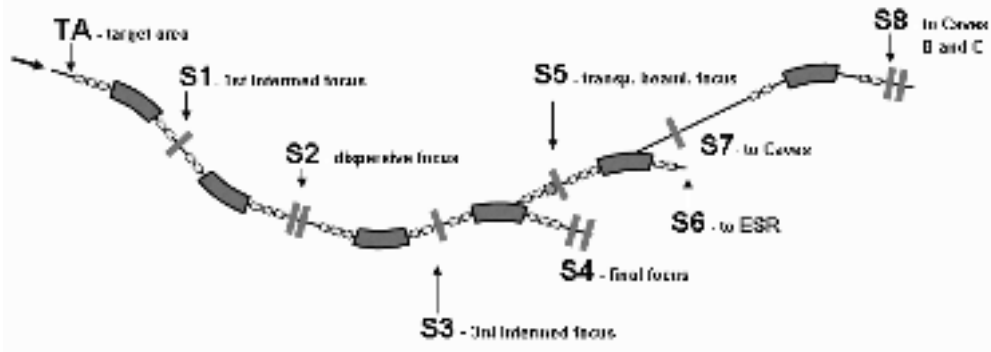

Figure 2.3: Fragment Separator (FRS) facility scheme and its areas.

At the entrance of the FRS, once extracted from the SIS-18 synchrotron, the beam enters the Target Area (TA), where the primary production target is located. There are 72 targets of different materials and thicknesses, as shown in figure 2.4 [54]. The most common by used materials are beryllium, carbon, aluminum, cooper and lead, all of them available in different thickness. The FRS configuration can be optimized for each projectile-target combination in order to maximize the transmission of the nuclei of interest and the beam purity.

Figure 2.4: Picture of the 72 production targets at the entrance of the FRS with its support. The optimum target can be selected remotely.

2.2.1 Ion production

The most important constraint for this kind of studies concerns the low production of the ions of interest, due to very low cross sections for these very exotic nuclei. Before the experiment several simulation tools such as Lise++ [55, 56] and MOCADI [57, 58] were used to calculate the yields and transmission of fragments produced. These calculations provided the optimal settings of the FRS elements to obtain the desired nuclei at the final focal plane S4. The largest production was obtained with a Beryllium (^{9}Be) target of 1.6 g/cm^2 thickness. Nuclear reactions such as fission and fragmentation took place generating a large amount of different nuclear species in the secondary beam [46]. In order to minimize the number of charge states, a 223 mg/cm^2 Niobium layer was placed after the target acting as a charge stripper. Two different spectrometer settings centered at ^{211}Hg and ^{215}Tl allowed to cover the nuclei of interest.

The magnetic fields set on each dipole and, more specifically, the $B\rho$ set in both sections of the FRS, are the most important parameters of each setting to center a given isotope along the FRS. Equation (2.1) describes the $B\rho$ in the first half,

$$B\rho_{S1-S2} = \frac{B_0 + B_1}{2} \cdot r_{12}(1 - \frac{x_2}{D_0}) \tag{2.1}$$

where r_{12} is the magnet radius between S1 and S2 (11.2030 m), D_0 is the dispersion measured between the target area and S2 with a value of -6.4743 m, and x_2 is the horizontal transversal ion position. On the second half of the FRS the $B\rho$ is given by equation (2.2),

$$B\rho_{S3-S4} = \frac{B_2 + B_3}{2} \cdot r_{34}\big((1 - \frac{x_4 - M_1 x_2}{D_1}\big) \tag{2.2}$$

where r_{34} is the effective radius (11.264 m), D_1 the optical dispersion (7.2203 m) and M_1 the magnification of the first half (1.1152).

For a better ion selection and suppression of fission fragments, two degraders were placed at the first and the second focal planes, S1 and S2, both used as charge selectors. Finally, slits at different stages of the FRS acted as a beam collimator reducing contaminants. Figure 2.5 shows the setup at S2 including degrader and the slits located at S4.

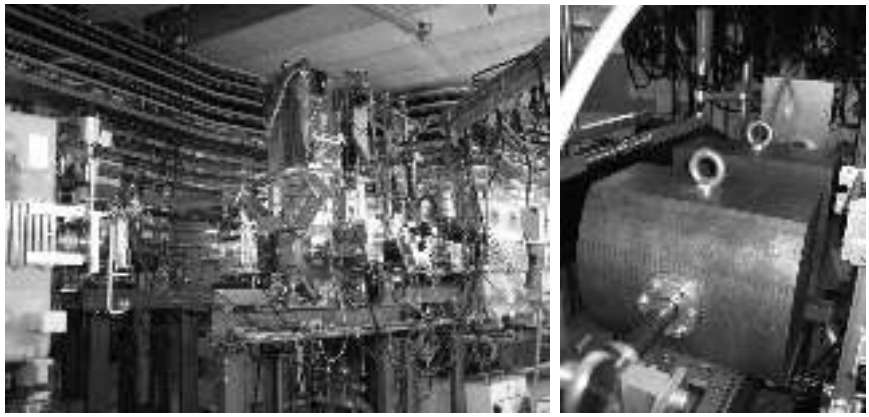

Figure 2.5: Left: Setup at S2 including the degrader. Right: Part of S4 setup showing the slits.

2.3 Ion identification

The first step of the data analysis is to obtain a good particle identification diagram (PID) of the ions passing through the FRS. This means to determine the atomic number (Z) and the mass-over-charge ratio (A/Z) for each detected ion.

Standard FRS tracking detectors were used during the experiment for an event-by-event identification. Several detectors located at S2 and S4 allow to determine the properties of nuclei passing through. Plastic scintillators, ionizing chambers and position detectors provided information on the time-of-flight, the atomic charge, and position and trajectory, respectively. With this information it is possible to identify each ion.

The schematic drawing in figure 2.6 shows the location of each detector in the experimental hall including the detection system, consisting of the SIMBA and BELEN detectors described in the next chapter.

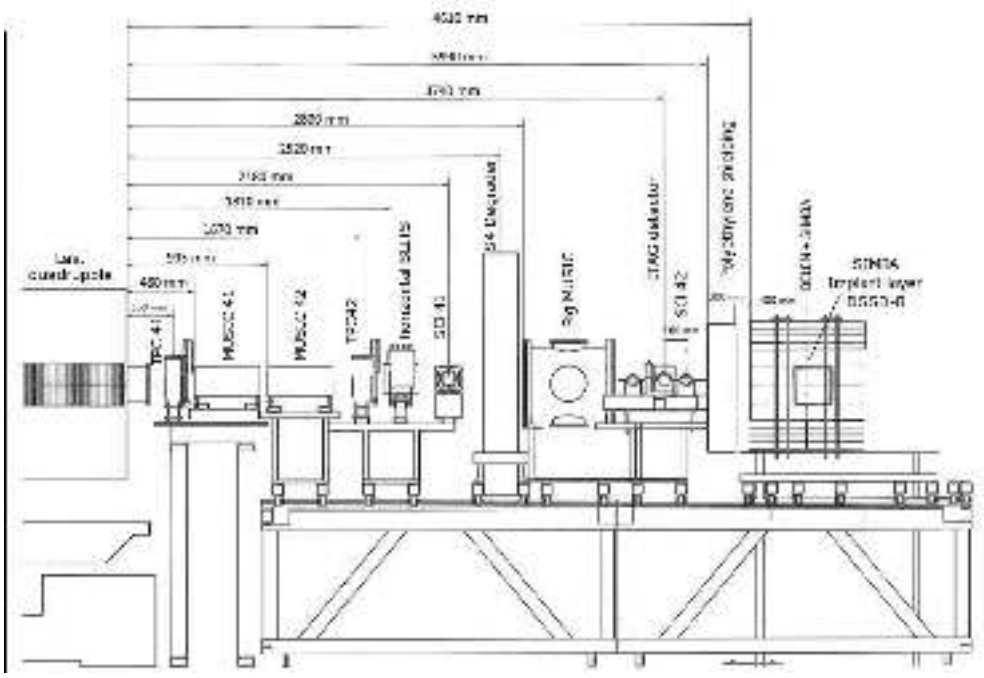

Figure 2.6: Schematic figure of the experimental setup at the S4-hall. (Adapted figure from S410 experiment team)

2.3.1 Mass-over-charge (A/Q) determination

The mass-over-charge ratio (A/Q) was determined from the measurement of the time-of-flight (t_{TOF}) between two plastic scintillators, *sci*21 and *sci*41, located at the intermediate focal plane (S2) and at the last focal plane (S4), respectively.

Each scintillator had two photomultipliers, one on each side (right and left) and the distance (L) between them was 36.71 m. The t_{TOF} is determined as the average of the t_{TOF} measured between the right (t^r_{TOF}) and the left (t^l_{TOF}) photomultipliers. In order to determine the relationship between the velocity β and the measured t_{TOF}, three calibration runs were carried out using a ^{238}U primary beam at 1 GeV per nucleon, with a S2 degrader thickness of 3 g/cm^2, and different target conditions. Each run had different amounts of material in the beam-path to obtain t_{TOF} calibration values for several known velocities β. Table 2.1 summarizes the calibration measurements.

With these values, figure 2.7 shows the linear calibration curve, which relates the t_{TOF} with the velocity β as described by equation (2.3). The resulting calibration for the t_{TOF} reflects the distance (L) between *sci*21 and *sci*41,

Beam run	FRS setup	β calculated with LISE++	Measured t_{TOF} (ps)
^{238}U	90 mg/cm^2 Cu Target	0.831293	54037.4 ± 50.9
^{238}U	1.6 g/cm^2 Be Target	0.797873	47888.5 ± 61.9
^{238}U	1.6 g/cm^2 Be Target + 2.5 g/cm^2 at S1 degrader	0.721750	31719.9 ± 127.9

Table 2.1: Time-of-flight calibration parameters.

which is of 36.7 m approximately (122448.0 ps normalized by the speed of light c), and an offset ($t_{TOF}|_{offset} = 201184.0\ ps$) due to the different length of the cables attached to the photomultipliers of the scintillators.

$$\beta = \frac{1}{c} \cdot \frac{L}{t_{TOF}} = \frac{1}{c} \cdot \frac{L}{t_{TOF}|_{offset} - t_{TOF}|_{measured}} \tag{2.3}$$

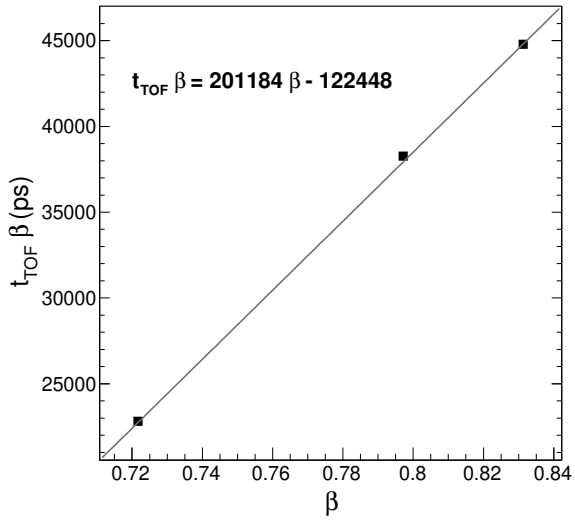

Figure 2.7: The time-of-flight (t_{TOF}) calibration is determined with this fit according to the values of table 2.1 with an expression like $t_{TOF}\beta = a\beta + b$, where $a = 201184 \pm 90\ ps$ and $b = -122448 \pm 70\ ps$.

The β calculated with the t_{TOF} combined with the $B\rho$ set on the magnets allows to determine the mass-over-charge (A/Q) ratio via equation (2.4).

$$B\rho = \frac{m}{q}\ \gamma v = \frac{A\mu}{Qe_0}\ \gamma \frac{L}{t_{TOF}} \rightarrow \frac{A}{Q} = B\rho\ \frac{e_0}{\mu}\frac{1}{\gamma}\frac{t_{TOF}}{L} = B\rho\ \frac{e_0}{\mu c}\frac{1}{\gamma\beta} \tag{2.4}$$

where A is the atomic mass, $\mu = 1.66 \times 10^{-27}\ kg$ the atomic mass unit, Q the ion charge, $e_0 = 1.602 \times 10^{-19}\ C$ the electron charge and γ the relativistic factor.

Trajectory correction via TPC position measurements

The beta (β) value obtained using equation (2.3) assumes that all ions follow a central trajectory whose length coincides with the exact distance between both scintillators. In order get a more precise A/Q determination, an angle correction is applied using the position information from Time Projection Chambers (TPC) [59]. This correction allows one to take into account the extra-flight path for non-central trajectories.

The way to implement this correction is based on the angle measured with the TPC's at S2 along the A/Q range obtained via equation 2.4. Owing to the high production yield, fission fragments were used for this purpose. In order to reduce statistical uncertainties, an isotope with large statistics is used to determine the correction parameters. Figure 2.8-left shows the selected element in terms of charge and figure 2.8-right the measured angle versus A/Q for this element.

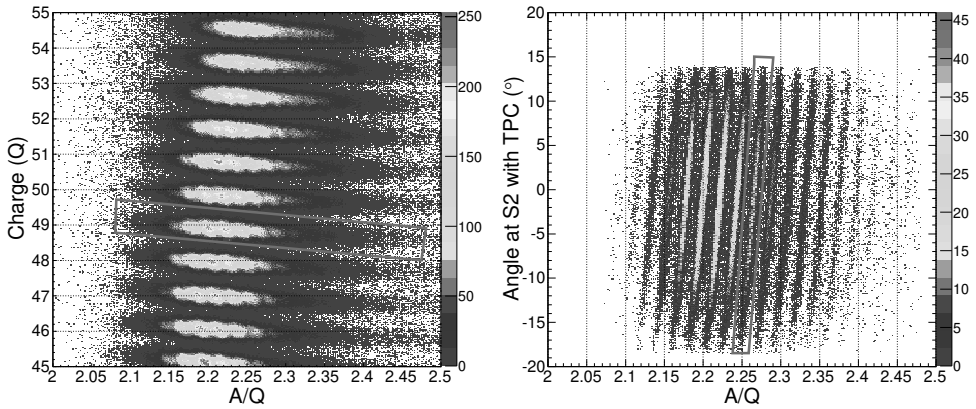

Figure 2.8: Left: PID before the correction where an element, in the fission fragments region is selected. Right: Measured angle versus A/Q of the selected element.

Once the calibration ion has been selected, the dependency of A/Q on the measured angle (α) is adjusted (figure 2.9-left), using a linear relation (equation (2.5)). When this correction is applied the improvement is remarkable, as can be appreciated by comparing figure 2.8-left with the new PID shown in figure 2.9-right. In terms of resolution the improvement is about 70%; changing from a relative FWHM of 1.40% for the initial A/Q to 0.44% for the corrected

value A/Q_{corr}. Figure 2.10 shows the improvement for a particular element.

$$A/Q_{corr} = A/Q - 0.001 \cdot \alpha \tag{2.5}$$

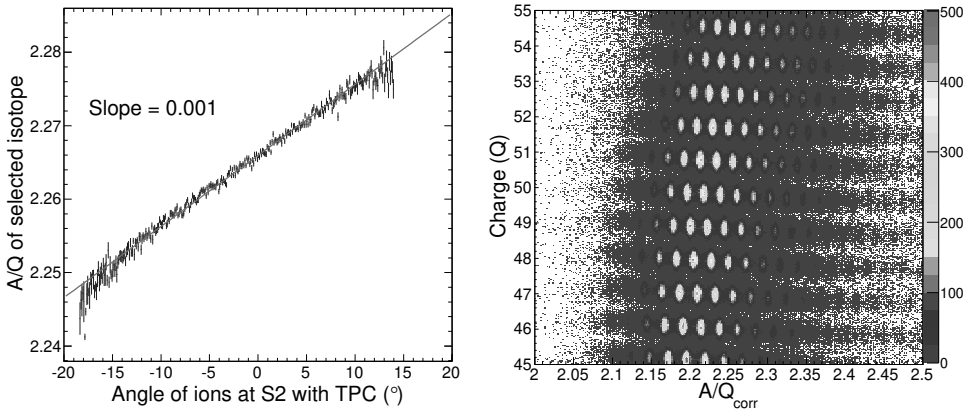

Figure 2.9: Left: A/Q versus the angle for a selected isotope. The red straight line corresponds to a linear fit. Right: PID after angle correction.

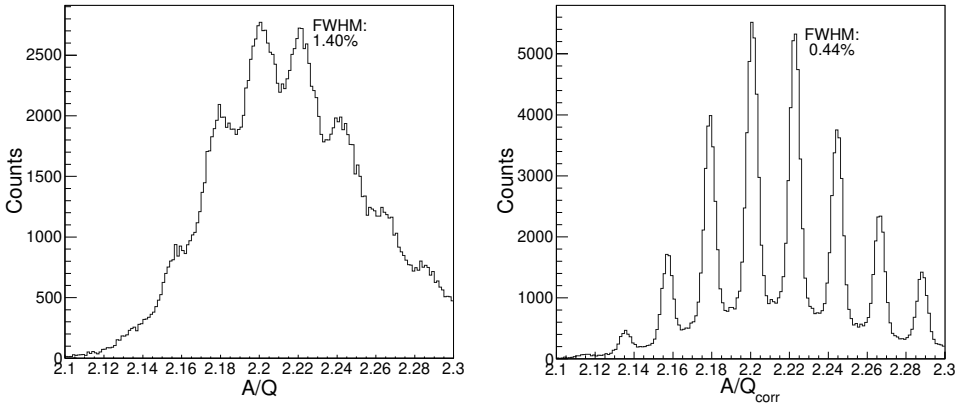

Figure 2.10: Projection of isotopes for a particular element in the region of the fission fragments from figures 2.8-left and 2.9-right. The indicated FWHM values show the resolution improvement for a selected isotope, with a determined raw charge of $Q = 49$ and a raw A/Q centered between $A/Q = 2.22$ and $A/Q = 2.23$. Left: Before the angle correction. Right: After the correction.

2.3.2 Atomic charge determination

In order to determine the charge (Q) of the ions passing through the FRS on an event-by-event basis, two fast MUltiple Sampling Ionization Chambers (MUSIC) [60] were placed at the last stage of the FRS in $S4$. Figure 2.11 shows pictures of one of them, while figure 2.6 shows their precise location in the experimental hall.

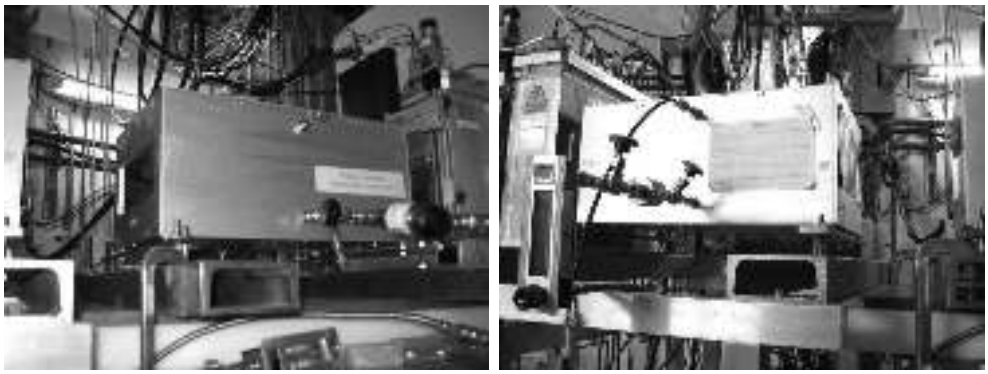

Figure 2.11: MUSIC chambers at the entrance of S4 experimental hall

These chambers consist of 8 anode strips and a vertical drift length of 80 mm. They operate with pure CF_4 as counting gas at room temperature and atmospheric pressure. They give the information of the energy loss (ΔE) of a particle crossing the detector calculated as the geometric mean of all anode segments (equation (2.6)).

$$\Delta E = \left(\prod_{i=0}^{8} \Delta E_i \right)^{1/8} \tag{2.6}$$

According to the Bethe-Bloch formula [61, 62], the energy deposition ΔE of a particle in these chambers is proportional to the ion charge squared (Q^2) and depends on its velocity (β). Following this formula and simplified parameterizations from previous experiments at FRS, a simplified equation (2.7) [54] is deduced to obtain the nuclear charge (Z),

$$Q = Z - n_e = Z_0 \sqrt{\frac{\Delta E}{v_{corr}}} \tag{2.7}$$

where Z_0 is the primary beam nuclear charge ($Z_0 = 92$ for ^{238}U) and v_{corr} is the measured velocity (β) from the t_{TOF} measurement, corrected according to the energy loss (ΔE) measured with the MUSIC, see the correction below. The atomic number (Z) can be assumed to be the measured charge (Q) by adding the charge state or the number of electrons (n_e) in the nucleus. If the nucleus is fully stripped $Z = Q$.

In addition to the two MUSIC, a third MUSIC was placed behind the S4 degrader in order to detect changes in the particle atomic charge. However, the large energy loss of the ions in the degrader hindered a reliable calibration of this third MUSIC. For that reason it was excluded from the analysis.

The following paragraphs describe in detail the data analysis and corrections applied to raw data acquired with MUSIC chambers. An isomer tagging (ITAG) identification provides the charge reference, and the other three corrections allow to improve the resolution of the atomic charge obtained.

Isomer tagging (ITAG) identification

With the aim of determining a reference calibration point in terms of atomic charge, a ^{205}Bi setting was configured at the FRS. This isotope has a high production and γ-rays unexciting its isomers are well known from previous experiments. The PID obtained from the measured charge Q at MUSIC 1 with respect to A/Q_{corr} of this calibration measurement is presented in figure 2.12-left. The identified nuclei were implanted in a passive stopper surrounded by a HPGe detector. The so-called isomer tagging station was inserted in the beam line for this measurement and afterwards removed (see its location in figure 2.6).

The energy and efficiency calibration of this HPGe detector was performed with calibrated ^{152}Eu and ^{137}Cs gamma sources, by following the method presented in [63]. Figure 2.12-right shows the energy spectrum of the detected γ-rays, where several well known isomeric transitions of ^{205}Bi (E_γ = 286.2, 697.4, 881.4 keV) can be clearly identified.

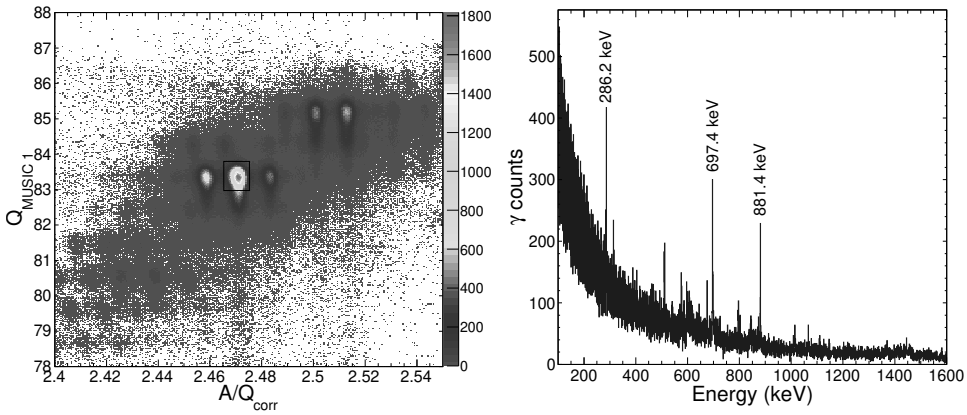

Figure 2.12: Left: PID of a ^{205}Bi setting with its events selected. Right: Raw γ-ray energy spectrum measured via isotope- γ-ray coincidence method.

A cleaner ^{205}Bi isomeric spectrum is obtained when several software cuts

are implemented. The first cut corresponds to the selection of ^{205}Bi events (shown in figure 2.12-left). The second cut is applied in time-domain (see figure 2.13-left) and allows one to effectively suppress the γ background. As a result an almost background free γ-ray spectrum is obtained (figure 2.13-right), and several ^{205}Bi γ isomers are identified at E_γ = 176.1, 286.2, 314.1, 340.0, 404.4, 469.1, 697.4, 796.0, 873.6, 881.4, 1110.2 keV. All these γ-rays are listed in the ^{205}Bi level scheme presented in figure 6 [10] in the appendix A.

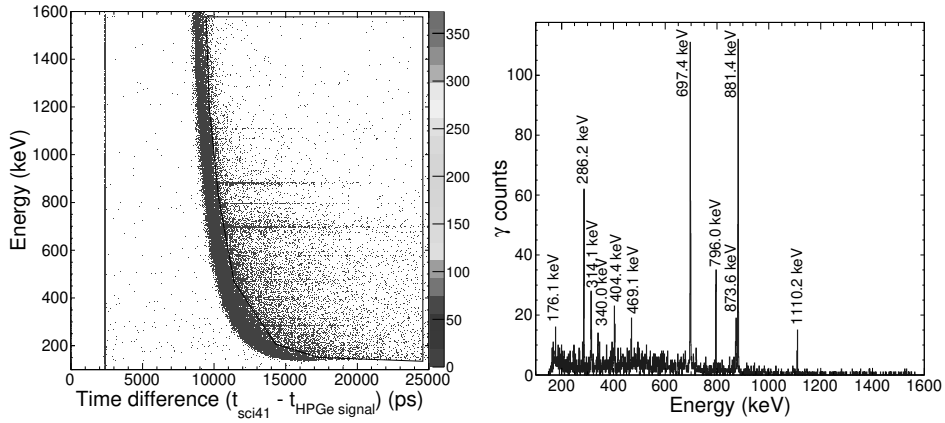

Figure 2.13: Left: Energy with respect to dt of *sci*41 and HPGe signals, with a gate to avoid the background γ-rays. Right: Improved γ-ray spectrum once the gates shown in figures 2.12-left and 2.13-left were applied.

This analysis allows to establish a reference value of the atomic charge (at $Z = 83$), for all settings in the experiment.

Velocity correction: MUSIC energy loss (ΔE) vs β

As expected from the Bethe-Bloch formula, the ΔE of the ions measured with MUSIC detectors depends not only on the atomic charge (Q) but also on their velocity β. In order to improve the resolution in Q, this dependency has to be corrected. This can be accomplished by introducing a velocity correction term, which allows one to improve the resolution in nuclear charge (Z). The coefficients of this velocity correction (equation 2.8) were determined by analyzing the dependency of the measured energy loss (ΔE) as a function of fragment velocity (β) for reference beams such which are listed below with a description of all the material traversed.

- ^{238}U - SEETRAM [64] + 90 mg/cm^2 Cu target + 3 g/cm^2 degrader + 0.97 mm at *sci*21.
- ^{238}U - SEETRAM + 1.6 g/cm^2 Be target + 3 g/cm^2 degrader + 223 mg of Nb stripper + 0.97 mm at *sci*21.

- ^{205}Bi - SEETRAM + 1.6 g/cm^2 Be target + 3 g/cm^2 degrader + 223 mg of Nb stripper + 0.97 mm at *sci*21 + 2.5 g/cm^2 at S1 degrader.

ΔE values obtained in these beam settings and used for this correction are listed in table 2.2. The calibration of the velocity correction is assumed linear (equation (2.8)) and is shown in figure 2.14. Higher order corrections did not improve the results and were therefore disregarded.

$$v_{corr} = a[0] + \beta \cdot a[1] \tag{2.8}$$

RUN and Beam fragment	Z	β max measured	ΔE (a.u) corrected to ref. Z=92 MUSIC 1	MUSIC 2
17 (^{238}U)	92	0.8311(2)	3442(4)	3377(4)
18 (^{238}U)	92	0.7979(3)	3675(8)	3623(8)
37 (^{205}Bi)	83	0.7367(3)	3459 → 4250(6)	3449 → 4238(4)
	85	0.7318(5)	3660 → 4288(8)	3651.4 → 4278(8)
Fit parameters			a[0]	a[1]
MUSIC 1			10551.5±57.4	-8563.64±72.21
MUSIC 2			10976.2±51.2	-9154.2±65.1

Table 2.2: ΔE values for ^{238}U and ^{205}Bi settings. The latter includes a correction of a factor of $\left(\frac{92}{Z}\right)^2$. Velocity correction parameters for MUSIC 1 and MUSIC 2 obtained are given in the two bottom rows.

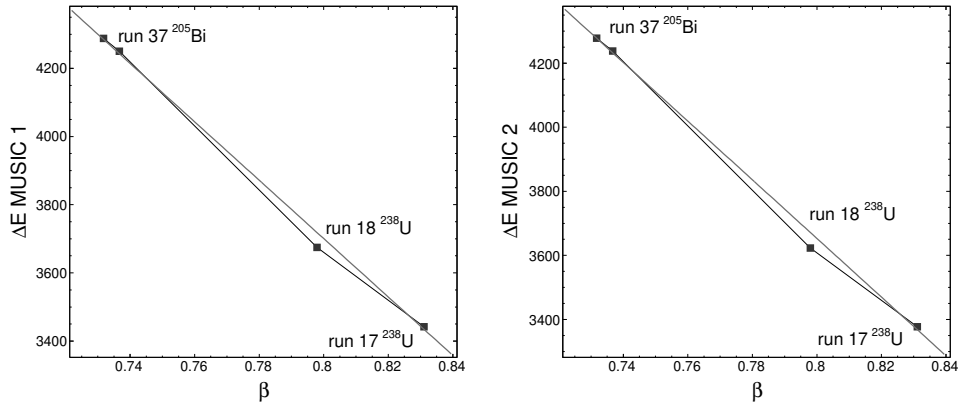

Figure 2.14: Linear calibrations for the velocity correction of the MUSIC detectors. Left: first MUSIC in the beam direction. Right: second MUSIC in the beam direction.

Finally, the charge (Q) of the particles is calculated by introducing this velocity correction, v_{corr}, in equation 2.7. The resolution in terms of charge improved considerably after implementing this correction, as it is demonstrated in figures 2.15 and 2.16 for both MUSIC detectors. This improvement can be quantified with the change in the FWHM-values of the corresponding distributions, which are reported in table 2.3. The values given in the latter table have been calculated for $Z = 82$ and $Z = 83$ in figures 2.15 and 2.16.

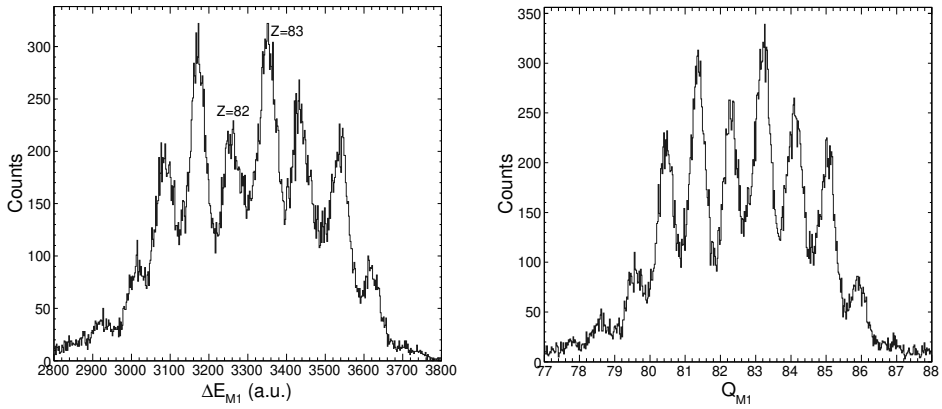

Figure 2.15: Energy loss measured with MUSIC 1 for the ^{211}Hg setting. Left: Raw energy loss (ΔE_{M1}) before the correction. Right: Energy loss (Q_{M1}) after introducing the velocity correction v_{corr}.

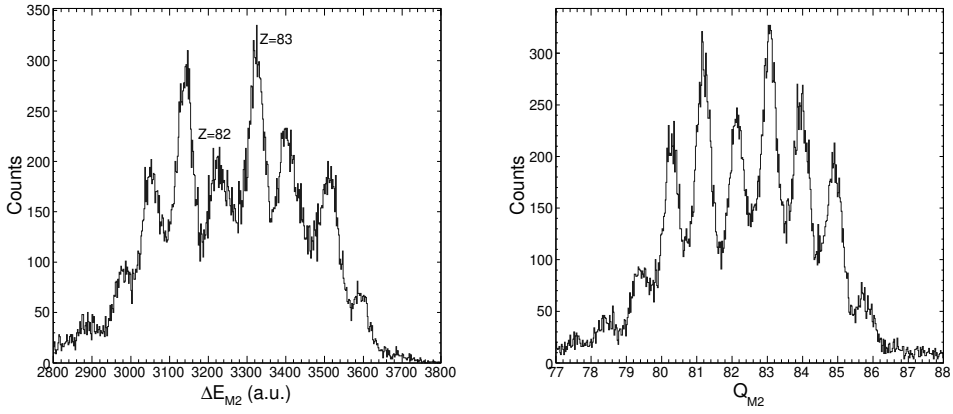

Figure 2.16: Energy loss measured with MUSIC 2 for the ^{211}Hg setting. Left: Raw energy loss (ΔE_{M2}) before the correction. Right: Energy loss (Q_{M1}) after introducing the velocity correction v_{corr}.

	$\text{FWHM}_{\Delta E}$	$\text{FWHM}_{(Q)}$	Improvement factor
MUSIC 1			
Q=82	2.78%	0.85%	3.3
Q=83	2.66%	0.98%	2.7
MUSIC 2			
Q=82	3.58%	0.91%	3.9
Q=83	2.38%	1.02%	2.3

Table 2.3: Evaluation of the improvement in resolution of MUSIC detectors applying an ion velocity correction.

Energy loss (ΔE) selection for each ion

Following a similar approach as reported in previous works in this region of the nuclear chart [53, 65, 66, 67], the effective charge (Q_{eff}) is defined as the charge corresponding to the highest value of the measured ΔE at MUSIC 1 and MUSIC 2 (ΔE_{M1} and ΔE_{M2}), determined with equation (2.7), (the maximum ΔE determined corresponds to the most probable measurement of the ion nuclear charge). Furthermore a Nb-foil was placed between both MUSIC chambers in order to enhance electron charge exchange from heavy ions flying through it. Figure 2.17-left shows the correlation of the determined charge on both MUSIC (Q_{M1} vs Q_{M2}), where it can be observed a large amount of events detected as H-like ($n_e = 1$) in one MUSIC and fully stripped in the other one. Q_{eff} is displayed in figure 2.17-right. The relative FWHM obtained is of 0.71% and 0.72% for $Z = 82$ and $Z = 83$ respectively, which means at least an improvement of 20% compared with the FWHM obtained using only one MUSIC detector (see table 2.3 and figures 2.15 and 2.16).

Correction of the measured energy loss time fluctuations

Another physical effect that needs to be taken into account is the MUSIC sensitivity to temperature fluctuations. This effect produces a drift of the gain for both MUSIC detectors along the time. The period of these fluctuations is of 24 hours, which corresponds to the daily cycle of temperature variations. If this effect is not corrected, it worsens the resolution of the measured ΔE and thus the calculated ion charge during the experiment. The drift can be clearly appreciated in figure 2.18-left, where the charge Q_{eff} is displayed as a function of time. The right panel in figure 2.18 shows the charge Q_{eff} from figure 2.17 projected in the vertical axis (Y).

In order to correct this effect in the region of interest ($78 \leq Q_{\text{eff}} \leq 88$), a numerical correction approach was applied. The latter consisted of an interpolation method with fixed correction values for period intervals of 5000 s. Once the correction is applied these fluctuations were practically eliminated for the

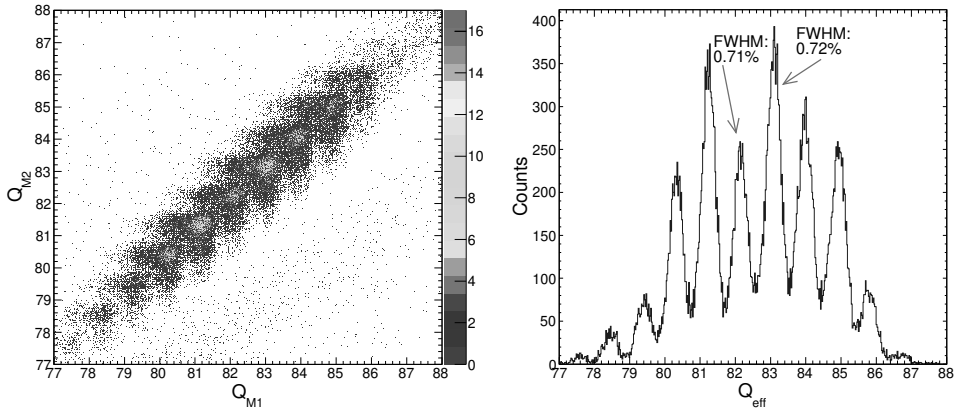

Figure 2.17: Left: Correlation of the charge calculated from the information of both MUSIC (Q_{M1} and Q_{M2}). Right: Determined Q_{eff} statistics for the amount of events tracked by the FRS in the ^{211}Hg setting.

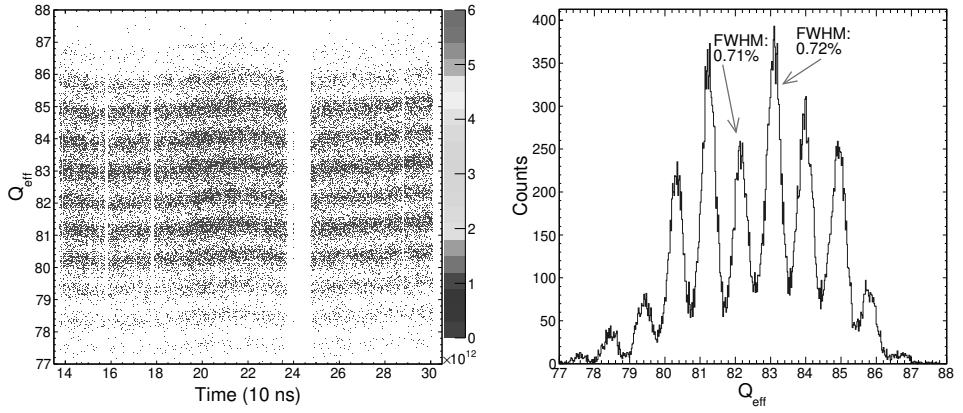

Figure 2.18: Left: Correlation of Q_{eff} along the time (before the drift correction). Right: Projection of the vertical axis, corresponding to the Q_{eff} accumulated during the ^{211}Hg setting.

new defined drift corrected Q_{eff}, (Q_{effdc}), as it can be observed in figure 2.19-left. Compression effects in charge Q_{eff} (see X axis in figure 2.18-right) were also corrected by means of this numerical approach, as shown in figure 2.19-right. Compared with Q_{eff}, the improvement of Q_{effdc} in terms of resolution is of around 20%, according to the evaluation of the FWHM, reported in table 2.4. Comparing with the raw charge measured with one MUSIC, the improvement is of around 80%.

In summary, the implemented corrections using the information given by

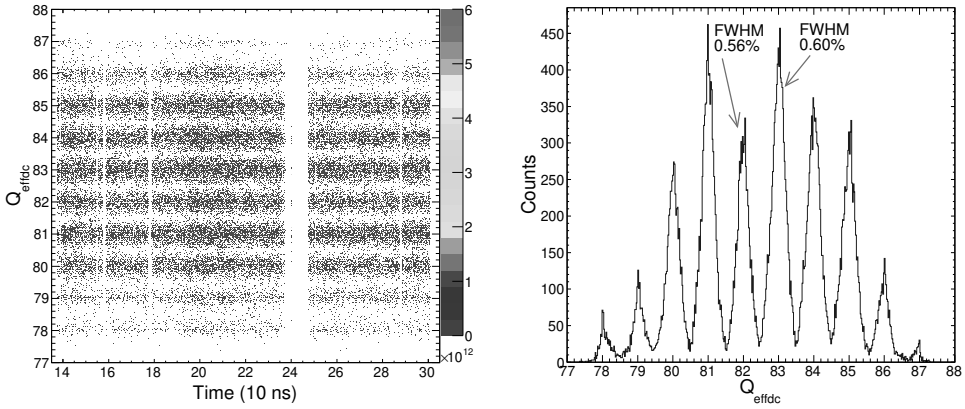

Figure 2.19: Left: Correlation of Q_{effdc} along the time (after the drift correction). Right: Projection of the left figure, Q_{effdc} corrected for the ^{211}Hg setting).

Peak	FWHM$_{Q_{\mathrm{eff}}}$	FWHM$_{Q_{\mathrm{effdc}}}$	Improvement factor
Q=82	0.71%	0.56%	1.3
Q=83	0.72%	0.60%	1.2

Table 2.4: Evaluation of the resolution improvement of the drift correction along the time for Q_{eff}.

the tracking detectors allowed us to improve the identification resolution both in mass-over-charge (A/Q) and nuclear charge (Z). At this point of the analysis it is interesting to compare the PID obtained before and after several correction steps. Figure 2.20-left shows the PID with the charge from the raw MUSIC signal after the velocity correction and A/Q from the direct t_{TOF} measurement. In figure 2.20-right one can appreciate the improvement when the PID is made using the corrected charge value Q_{effdc} and the A/Q with the angle correction.

2.3.3 Ion charge states correction

Most of the ions passing through the FRS are expected to flybe fully stripped. However, the probability to detect H-like or He-like ions, and even Li-like ions increases at high Z. Thus, for the present experiment this is a non-negligible effect which needs to be taken into account.

Following previous studies in this mass region [53,65,66,67], the energy loss at S2 degrader ΔE_{S2} was experimentally determined. With this value, it is

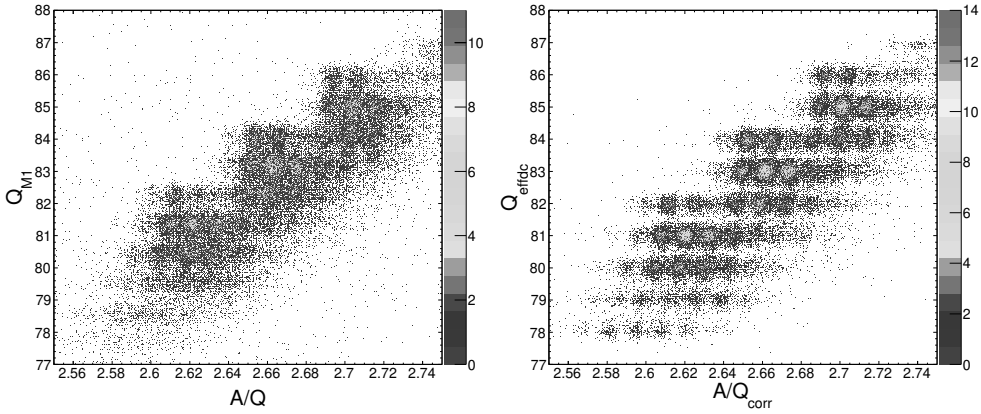

Figure 2.20: Identification diagrams PID in several steps of the presented corrections (statistics of ^{211}Hg setting). Left: Q_{M1} vs A/Q. Right: Q_{effdc} vs A/Q_{corr}.

possible to get the distribution of charge states and to implement a correction according to the number of electrons for each ion when flying through the FRS.

This correction is based on the comparison between the Lorentz factor of the expected ion velocity before the degrader, γ_1, and the measured velocity after it, γ_2, obtained from the time-of-flight (t_{TOF}) and described in subsection 2.3.1. The latter quantity becomes sensitive to the precise charge state of the ion passing through FRS. Equations (2.9) and (2.10) describe the dependency of the energy loss ΔE on γ_1 and the velocity after the degrader.

$$E = mc^2 \cdot \gamma(v) \tag{2.9}$$

$$\frac{\Delta E_{S2}}{q} = \frac{mc^2\,(\gamma_1 - \gamma_2)}{q} = \frac{\mu A c^2}{Q e_0} \cdot (\gamma_1 - \gamma_2) = \frac{\mu c^2}{e_0} A/Q_{corr} \cdot (\gamma_1 - \gamma_2) \tag{2.10}$$

where the atomic mass unit $\mu = 1.66 \times 10^{-27}\ kg$, the speed of light $c = 299.8 \times 10^6 m/s$ and the electron charge $e_0 = 1.602 \times 10^{-19}\ C$.

The relation between the mean value of $B\rho$ at the first half of the FRS (from Target Area to S2) with the momentum $\overrightarrow{p}$ of the particle is presented in equation (2.11), from where, the value of γ_1 can be derived (equation (2.12)).

$$\overrightarrow{B}\rho = \frac{\overrightarrow{p}}{q} = \frac{\gamma(v) \cdot m\overrightarrow{v}}{q} \rightarrow \gamma(v) = \frac{\overrightarrow{B}\rho \cdot q}{m\overrightarrow{v}} \tag{2.11}$$

$$\gamma_1 = \frac{B\rho_1 \cdot Qe_0}{A\mu \cdot c\beta} = \frac{e_0}{\mu c} \cdot \frac{B\rho_1}{A/Q \cdot \sqrt{1 - 1/\gamma_1^2}}$$
$$\gamma_1 = \sqrt{\left(1 + \left(\frac{e_0}{\mu c}\right)^2 \cdot \left(\frac{B\rho_1}{A/Q}\right)^2\right)} \tag{2.12}$$

On the other hand, γ_2 is directly obtained from the velocity β determined via the t_{TOF} measurement (equation (2.13)).

$$\gamma_2 = \sqrt{\left(\frac{1}{1 + (v/c)^2}\right)} = \sqrt{\left(\frac{1}{1 + \beta^2}\right)} \tag{2.13}$$

Combining equations (2.12) and (2.13) with the expression (2.10) for the energy loss at S2 degrader, ΔE_{S2} can be represented as a function of the nuclear charge Q_{effdc}. This dependency is shown in figure 2.21-right. In this figure three regions, corresponding to each charge state can be identified: fully stripped ($n_e = 0$), H-like ($n_e = 1$) and He-like ($n_e = 2$). This information allows to implement a numerical method to correct the charge states for each identified ion. Then, following the prescription given by equation (2.14), a correction is applied on an event-by-event basis according to its charge state. With this correction a PID with a horizontal axis based on A/Z instead of A/Q_{corr} can be build.

$$\frac{A}{Z} = \left(\frac{A}{Q}\right)_{corr} \cdot \frac{Q_{\text{effdc}} - n_e}{Q_{\text{effdc}}} \tag{2.14}$$

where n_e is the number of electrons in the nuclei along the second half of the FRS.

In order to obtain a better correction, events with unclear charge state value near the boundaries of each region (see figure 2.21-right) were rejected in the analysis. With this method an excellent resolution in Z is eventually obtained. This is reflected in figure 2.22, where the FWHM values are of 0.36% and 0.38% for lead and bismuth, respectively. This means approximately an improvement of 85% with respect to the raw ΔE given by the MUSIC detectors.

Concerning the mass-over-charge (A/Z) ratio, the obtained resolution after the charge states correction is of around FWHM = 0.25% for the lead isotopes with more statistics, which allows for a reliable identification of the ions. The resulting identification diagram PID, after applying all these corrections, is presented in figure 2.23. This figure presents the nuclear charge Z versus the A/Z-value obtained after applying equation (2.14). Being the last correction applied, it corresponds to the final PID for the half-lives and neutron branching

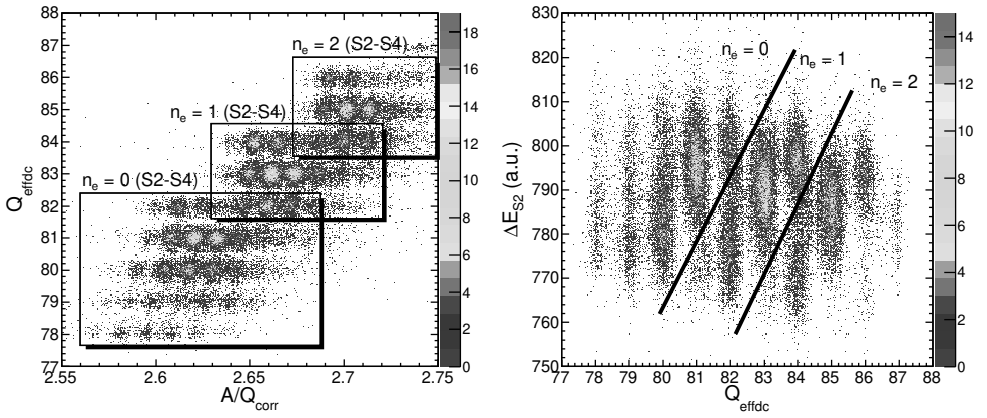

Figure 2.21: Charge states identification according to energy loss at S2 degrader, ΔE_{S2}. Left: preliminary PID with the charge states regions clearly identified. Right: correlation between the nuclear charge Q_{effdc} and the calculated ΔE_{S2}.

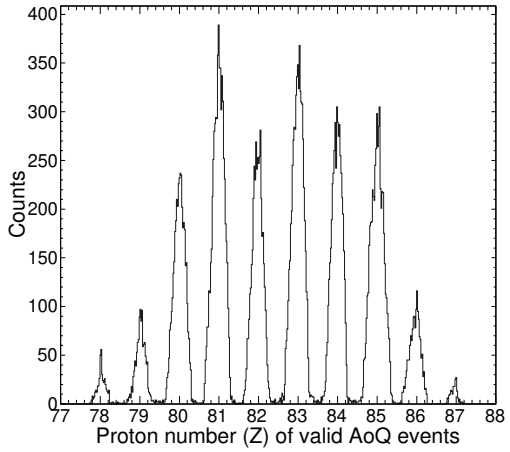

Figure 2.22: Z-distribution determined once the charge states correction was applied. ^{211}Hg setting.

analysis described in chapter 4. A total of 30822 events have been precisely identified in the region of interest, which comprises isotopes of gold, mercury, thallium, lead, bismuth, polonium, astatine and radon. All identified isotopes were also identified in previous experiments [68, 69].

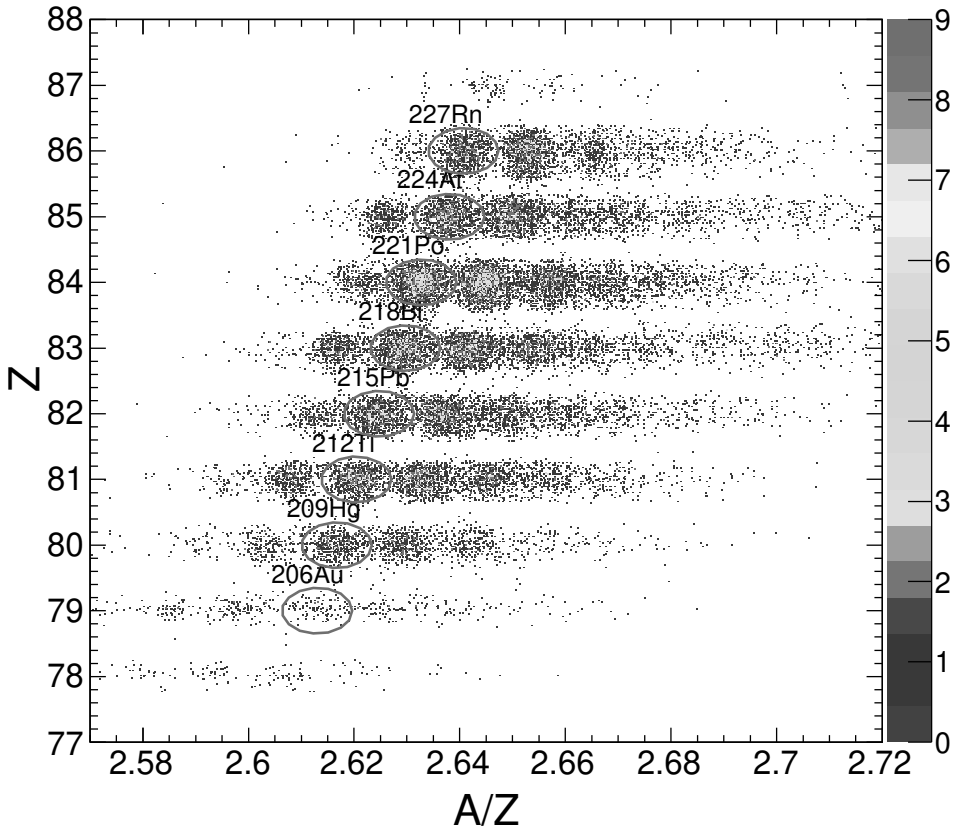

Figure 2.23: Final PID with the total statistics of the identified events (^{211}Hg and ^{215}Tl settings).

Chapter 3
Detection system

The detection system was located at the final focal plane of the FRS. It consisted of two main elements: The Silicon IMplantation Beta Absorber (SIMBA) detector and the Beta dELayEd Neutron (BELEN) detector. Two photographs of the detection apparatus are shown in figure 3.1. SIMBA served as an active stopper, which allowed to detect implanted ions as well as charged decay-particles such as β- and α-particles. On the other hand, neutrons were detected with high efficiency by means of the BELEN detector. This chapter describes their main technical characteristics. For SIMBA we show energy- and position-calibrations and the methodology developed in order to accurately characterize each event as either ion-implant or β-decay. A similar description is made for the reliable identification of neutron events in BELEN.

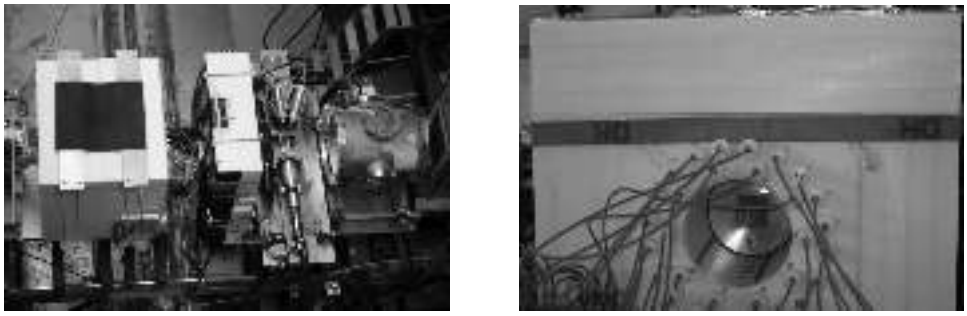

Figure 3.1: Left: Top view of BELEN at the end of the beam line. Right: Detail of SIMBA detector inside the BELEN polyethylene matrix.

3.1 The Silicon Implantation Beta Absorber detector

3.1.1 Technical description

SIMBA consists of a stack of highly segmented silicon detectors and has been developed at the Technical University of München (TUM) [70, 71]. It was specifically designed for the detection of both light (α- and β-particles) and heavy charged ions. The SIMBA apparatus implemented in this work corresponds to an upgraded version of the same detector used successfully in

previous experiments [72] at FRS. The main modification corresponds to the external housing of the device, which was adapted to fit inside the cylindrical central hole of BELEN. The final assembled system is shown in figure 3.1-right.

The core of SIMBA is an array of nine segmented planar silicon detectors. This stack can be divided in four sections (see figure 3.2, adapted from [70,71]), which are described below.

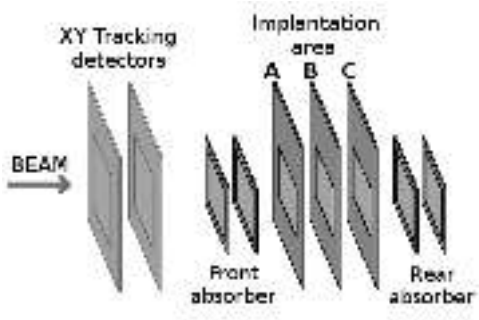

Figure 3.2: Schematic view of the SIMBA silicon detectors: From left to right (beam direction) the two XY-tracking silicons, the front absorbers, the implantation layers A, B and C and the rear absorbers.

The first group of two silicon detectors (in the beam direction) corresponds to the so-called XY-tracking detectors. These are single-sided strip detectors and their main role is to provide an accurate determination of the beam-transversal (XY) position of the ion passing through. These two tracking detectors have an active area of $60\times60\text{mm}^2$ with a thickness of 0.3 mm each one and are separated by 4.5 mm. Their segmentation is of 60 strips for each detector (1 mm/strip). The first tracking detector is oriented with its strips in horizontal position and thus provides the vertical position (Y) of the ions. The second tracking detector is arranged with the strips oriented vertically and thus provides the horizontal ion position (X). For the analysis of these detectors a software-threshold is set in order to suppress electronic noise of each strip-electrode. No precise energy calibration is needed for the tracking detectors because the energy deposited by the ions flying through them is very well separated from the electronic noise.

Separated 27.55 mm from the second tracking detector, the next group are two Single-Sided Strip Detectors (SSSD) named front absorber. Each one has an active area of 60×40 mm^2 a thickness of 1 mm and a 7 fold segmentation along the X direction (8.57 mm/strip). These two detectors were used only to determine, more accurately, the depth of the ion implant events as described below in section 3.2.1.

Behind the front absorbers is the next group of three Double Sided Segmented silicon Detectors (DSSD), also designated as implantation layers A, B

and C. The active area of each DSSD is of 60×40 mm^2 with a thickness of 0.7 mm and 2.6 mm separation between each layer. According to their thickness, the total implantation length along the beam line is of 2.1 mm of silicon. A-, B- and C-detectors are highly segmented, 60-fold along the X-direction and 40-fold in the Y-direction (1 mm/strip). As a particularity, due to technical constraints, the six strips located in the edges of the Y direction are processed in two channels being the total number of readout channels of 32. With this reduction the total grid in the implantation area consists of 60×32×3 (5760) effective pixel positions, with each pixel, in the central region, with an area of 1 mm^2.

The last two layers consist of SSSD named rear absorbers, with the same functionality and properties as front absorbers. They are used to confirm an implant in the last DSSD and to identify non implanted ions passing through SIMBA. The technical properties of these silicon layers can be found in [71]. Figure 3.3 shows a picture of SIMBA without its housing, where layers are placed on the right of the picture and the readout system on the left.

Figure 3.3: Picture of SIMBA without its housing, picture by K.Steiger.

3.1.2 Implant XY position via SIMBA tracking detectors

The main functionality of SIMBA tracking detectors is to allow one to determine the ion position in the beam transversal plane (XY). Hereby, the first tracking detector is employed for the determination of the ion Y-coordinate, whereas the second one is used for the X-coordinate. The heavy ions arriving to SIMBA typically have sufficient energy to cross these two thin detectors (0.3 mm) and the energy deposition is lower than the amount of energy deposited in the implantation area. The position determination consists of a complex method involving mathematical corrections of several physical effects, as described below in three steps:

i) The ion position in X and Y detectors is obtained by means of the center

of gravity of the charge shared over all strips and read out at the two sides of a serial resistor network chain. The signal collected on each side, E_r (right) and E_l (left), is proportional to the number of resistors crossed, one per strip, and the distribution of the deposited energy along the strips in the detector. Using the information of these signals, equation (3.1) is used to obtain the raw position of the ions. Figure 3.4 shows the resulting relative position for X during a large run of ^{211}Hg.

$$Pos_{raw} = \frac{E_r - E_l}{E_r + E_l} \tag{3.1}$$

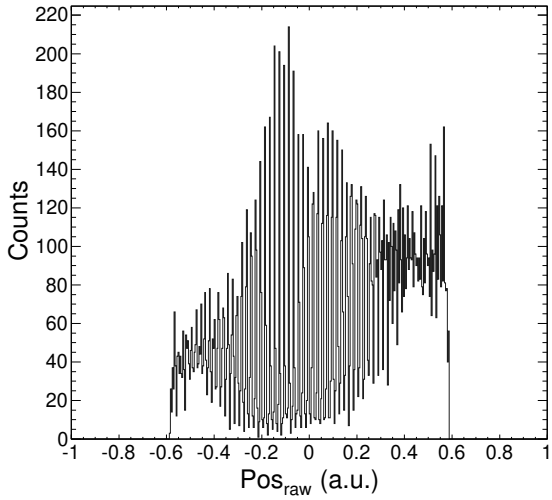

Figure 3.4: Raw position obtained from equation (3.1).

ii) When the raw position thus obtained is represented against the deposited energy (figure 3.5-left), there is a strong correlation, specially at low energies. In order to compensate this effect, a correction is applied along the whole energy range. It consists of a complex method similar to the one described in [73], following the prescription given by equation (3.2), and applied on each side of the silicons.

$$Pos_{corr} = \frac{\frac{E_r}{a_0 \cdot (E_r + E_l - a_1)^{a_2} + a_3} - \frac{E_l}{b_0 \cdot (E_r + E_l - b_1)^{b_2} + b_3}}{E_r + E_l} \tag{3.2}$$

Its parameters, represented as a_0-a_3 and b_0-b_3 in table 3.1, can be determined by fitting the projection of the events at the first strip on each

side (see the zoom in figure 3.5-left, for X-left correction), once normalized to the maximum value. After implementing this correction, a more homogeneous response is obtained, as shown in figure 3.5-right.

Parameter	X-left (b)	X-right (a)	Y-left (b)	Y-right (a)
0	0.367	0.357	0.353	0.295
1	1194.62	1222.91	956.72	985.94
2	0.0558	0.0609	0.0613	0.0912
3	0.423	0.412	0.422	0.382

Table 3.1: SIMBA tracking energy dependence calibration parameters.

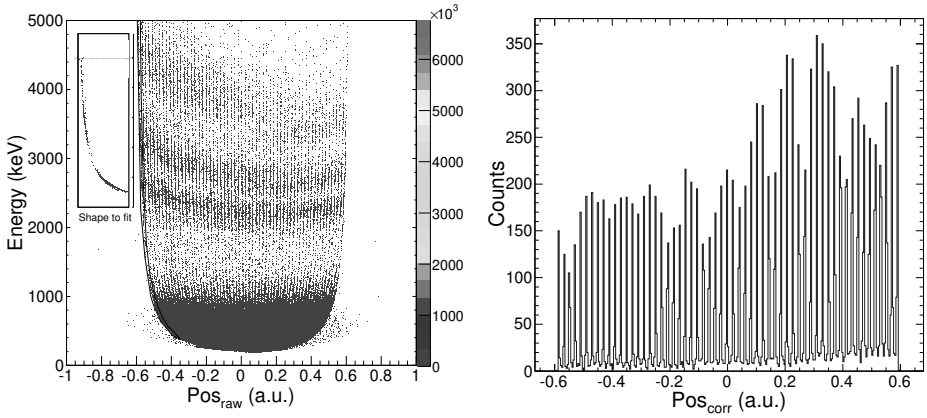

Figure 3.5: Left: Raw position versus the sum of deposited energy on both sides. Right: Relative position corrected by means of equation (3.2). See text for details.

iii) Finally, the relative corrected position was expanded by means of a 4^{th} degree polynomial into DSSD strip units. The thus obtained position calibration parameters are reported in table 3.2.

Tracking detector	p_4	p_3	p_2	p_1	p_0
X	0.545867	3.53266	-0.678538	48.0377	29.0728
Y	-0.184994	3.73492	0.356272	48.9512	28.0407

Table 3.2: Parameters of the 4^{th} degree polynomials for the XY tracking detectors position calibration according to DSSD strip units.

The quality of the full procedure is demonstrated in figure 3.6, where

it can be appreciated that the position is distributed over 60 channels, 1 mm per channel.

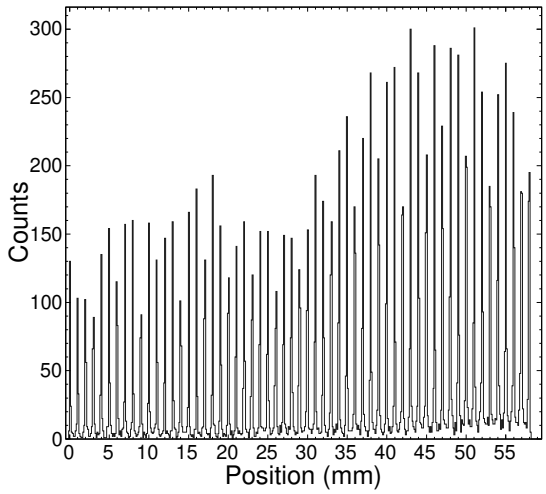

Figure 3.6: X tracking detector position calibrated according to DSSD strip units (1 mm).

For the vertical (Y) calibration the procedure is equivalent to the horizontal method here described. As a particular observation, for the presented case of the X axis, it only shows 59 channels instead of 60 due to a slight misalignment of the XY-detectors. The first strip of X was not crossed by Y strips, which makes it not feasible to assign a good position to the events passing through it.

In addition, it was checked that the ion trajectories measured with the TPC's are consistent with the positions measured with SIMBA, confirming the proper alignment of SIMBA in the beam-line.

3.1.3 Energy and position characterization of the SIMBA implantation layers A, B, and C

The three DSSD layers of SIMBA, A, B and C, are the region where ions of interest selected with the FRS are implanted. In particular, the S4-degrader thickness was adjusted in order to implant the setting fragment and its closest neighbors. The analysis of the DSSD signals comprises mainly two aspects: to determine the position where an event occurs and to evaluate the deposited energy to be able to assign the type of charged particle. The Y strips are readout by logarithmic preamplifiers, which allow one to clearly separate decays from heavy ions passing through. The X strips were connected to linear

preamplifiers and they were readout by a GASSIPLEX [74, 75] system, which is a specific ADC multiplexer system.

Energy calibration

The energy calibration consists of two steps: a gain matching of the response of all strips and the conversion of the measured energy information into energy units. The latter has been achieved by means of a linear polynomial calibration, by using the clear signature in the spectra of well identified α-decays. By means of a common energy calibration it was possible to establish common upper thresholds to clearly distinguish between β-particles and ion events. This procedure can only be implemented in the Y direction of DSSD's thanks to their logarithmic preamplifier, which helped to distribute the deposited energy with a wide range to make easier the identification of an ion deposition or a decay particle. The X strips were not well suited to distinguish between implants and decays due to the linear preamplifier used.

The overall performance of the calibration can be observed by comparing figures 3.7-top and 3.7-bottom. Left figures show the deposited energy as a function of the strips, and right figures present the projection of them along the energy range. Here one can appreciate the alignment of the implantation area (high energies) and the two main α peaks detected (see the detailed zoom), which correspond to the decay of ^{211}At produced during a ^{205}Bi setting at the beginning of the experiment.

β-decay position

The position of decay particles in the DSSD's is determined thanks to the information given by the energy deposited in each strip. In the vertical direction (Y), the response of the logarithmic preamplifiers give a signal distribution similar to a Gaussian shape, whose maximum corresponds to the ion position strip. For the horizontal strips (X) the energy deposition saturates in several strips both for ions and β-decays. In these cases the position is taken as the central strip of those saturated.

For a reliable implant-β position correlation the XY ion tracking position has to be consistent with the β-decay position measured in the DSSD detector. In order to proof this consistency the alignment of the three DSSD and the tracking detectors has been checked. Figure 3.8 shows the corresponding correlation between the first DSSD and the position measured by the tracking for the X strips. Top and central histograms correspond to the tracking and DSSD positions, accumulated for a large run, respectively. The bottom histogram details some examples of DSSD strips position with a condition on the position in the tracking detector, showing a good agreement for both position calculations.

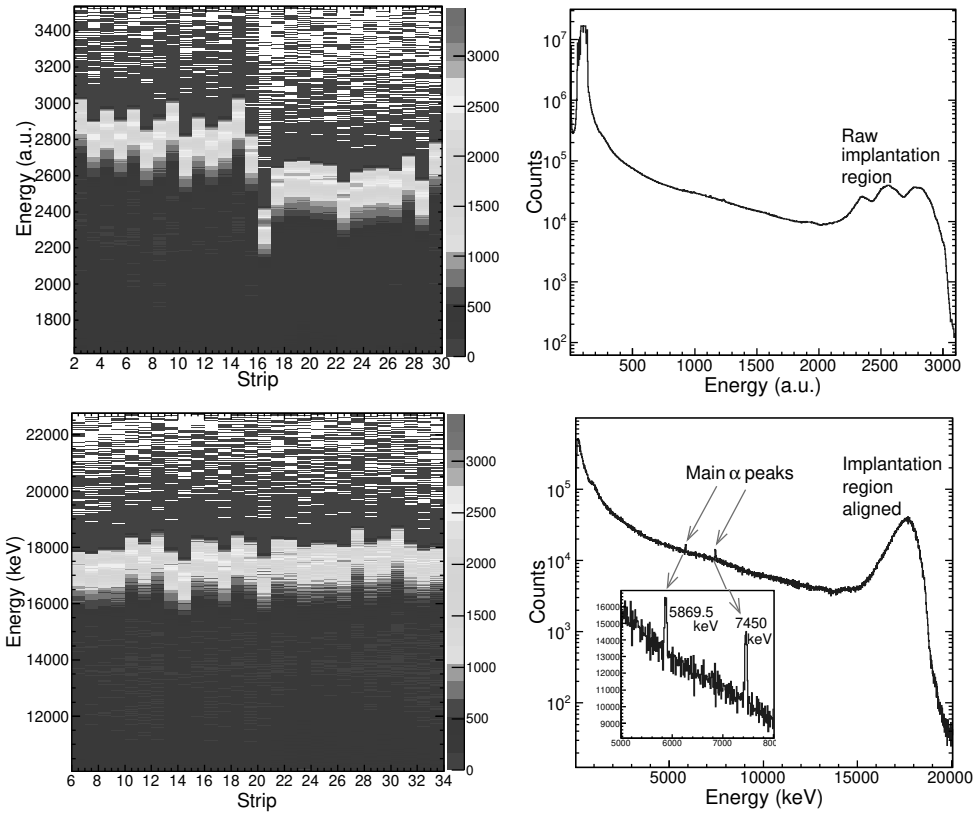

Figure 3.7: Energy spectrum measured for the vertical Y direction in DSSD-A. Top: Raw energy before the gain matching and calibration. Bottom: Once calibrated. Left: Detailed for each Y strip with a zoom in the implantation energies. Right: Projection of left diagrams in the full energy range.

Apart from the alignment of the detectors, several tests were performed in order to check the position of ions passing through the silicons. The most significant check is shown in figure 3.9, where the difference between the measured position at the first DSSD (A) and the others B (left) and C (right), results in a Gaussian distribution centered at 0, thus confirming the consistency of the position calibration between implant layers.

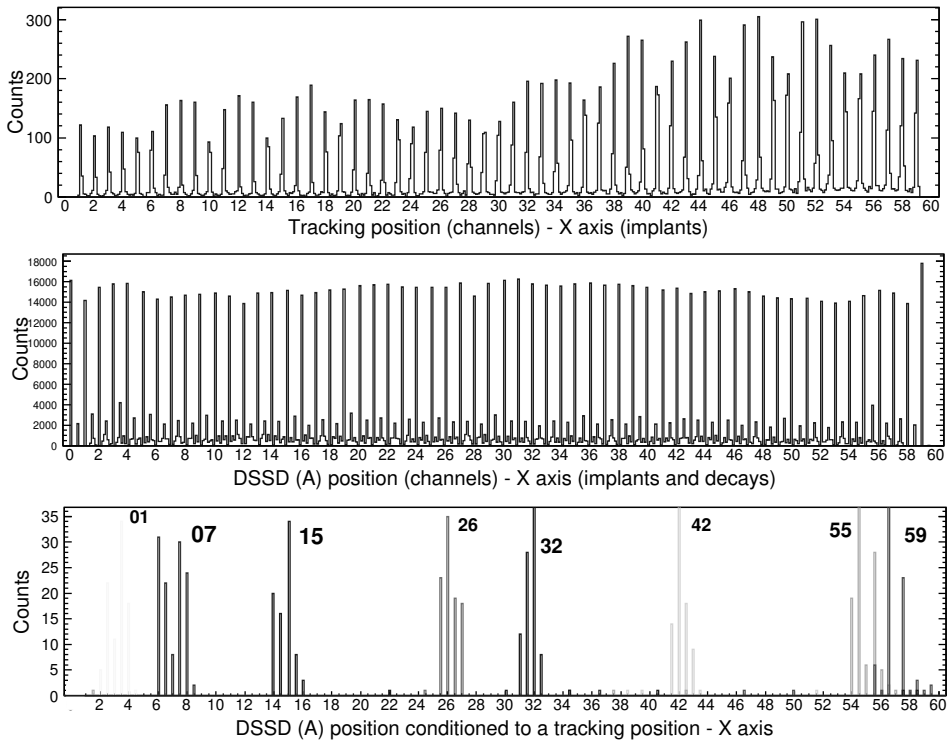

Figure 3.8: Alignment checking between tracking and DSSD layers of SIMBA.

3.2 Implant and decay events

The trigger system set in the acquisition system allows to identify each detected event as an ion (trigger associated to a signal on *sci*41) or a decay particle in SIMBA. This information, together with the energy deposited in each silicon layer makes it possible to determine the properties of the event by assigning the event type as an implant or a decay such as α- or β-particle.

3.2.1 Characterization of implantation events

The first condition for an event to be considered as an ion implant in SIMBA is to be in time coincidence with the scintillator *sci*41. Indeed, when the response of *sci*41 exceeded a certain threshold level, the so called implant-trigger activated the data acquisition over a predefined time window of all FRS tracking detectors and SIMBA. A further condition for the event to be considered as a valid implant, was that the position measured with the XY-detectors falls in the range of 0-60 mm for the X direction and 10-50 mm for the Y direction.

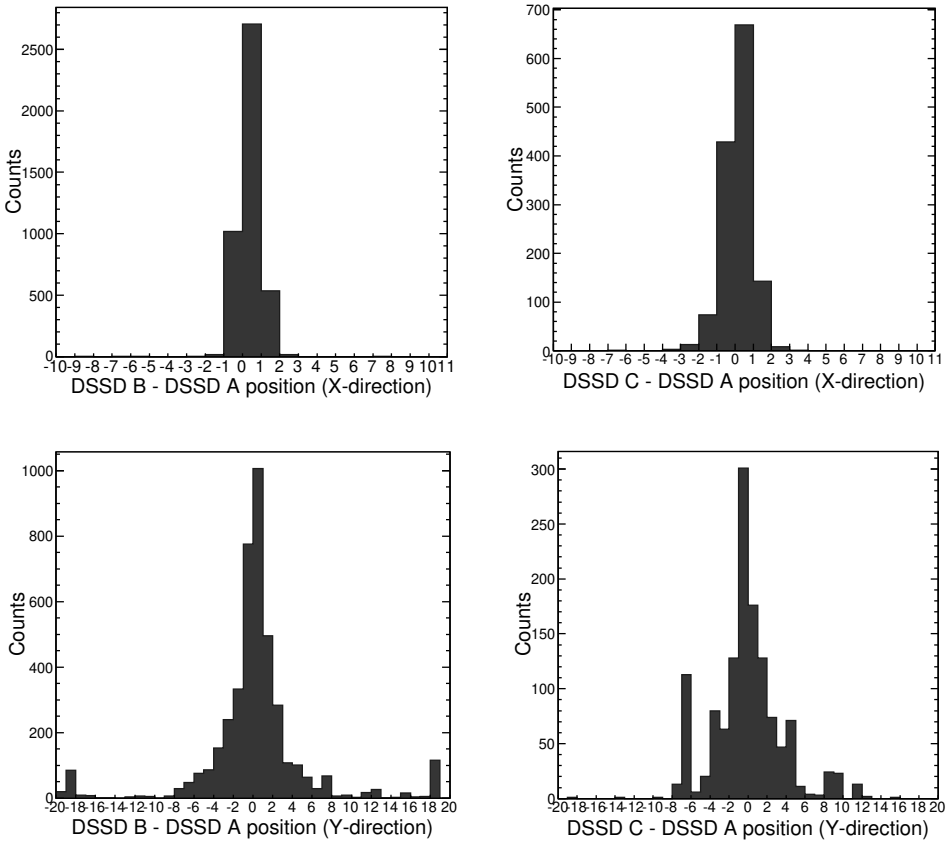

Figure 3.9: Position checking of DSSD layers: X-direction (top) and Y-direction (Bottom).

When these two conditions are met it is considered that the event may be a potentially good implant and thus the energy deposition in each SIMBA layer is examined. Along the Y DSSD's direction it must exceed a specific threshold, and along the X direction the multiplicity of saturated strips must be at least three. This condition was empirically established after visual inspection of a large number of decay and implant events. The implantation depth corresponds to the last layer accomplishing these conditions. However, when there was an energy deposition above a threshold in the rear SSSD layers the ion was not considered as implanted.

As examples of the implant position along the beam direction (Z), figure 3.10 shows the implantation depth for ions of ^{209}Hg (left) and of ^{213}Tl (right). It can be observed that most of the ions are implanted in DSSD (A,

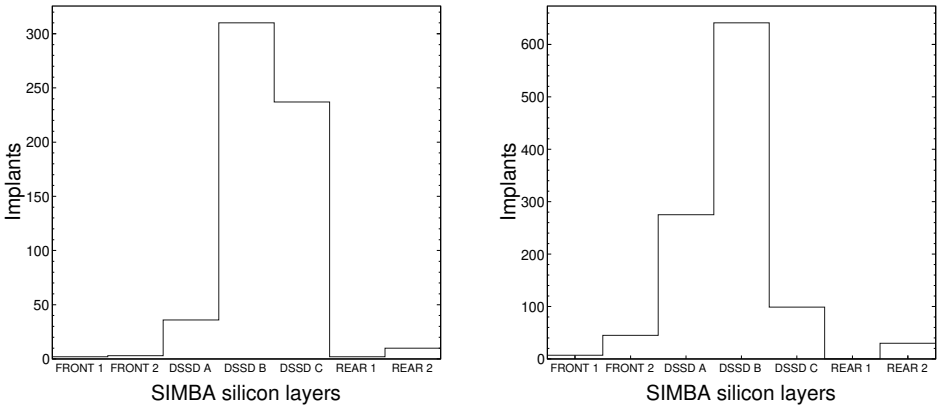

Figure 3.10: SIMBA implantation depth for ^{209}Hg (left) and ^{213}Tl (right). Silicon layers are detailed on X axis and the histogram bars present the number of implants on each one.

B or C) layers, being the implantation depth for ^{209}Hg slightly larger than for ^{213}Tl ions, as it was to expect from their lower charge Z.

Implantation statistics

After implementing the previous conditions in the data analysis, it was found that mainly isotopes of gold, mercury, thallium, lead and bismuth were efficiently implanted in SIMBA. Figure 3.11 shows the amount of implanted ions for each isotope, several of them with sufficient statistics to analyze and determine their decay properties reliably.

3.2.2 Characterization of decay events

The decay events are identified thanks to a trigger activated when an event occurs in SIMBA and no particle is detected in scintillator *sci*41. Decay events are defined by continuum energy collection in both X and Y strips and occurs most of the time in a single DSSD. Thus the 3D coordinates of the decay position (x,y,z) can be directly determined. As expected, the spectrum for each layer, has associated specific energy peaks, corresponding to α-particles, and a broad bump at low energies from β-particles. In order to illustrate this statement, figure 3.12 shows the decay energy spectra obtained on each DSSD (A, B, C) along the two settings of the experiment, ^{211}Hg and ^{215}Tl. The main features of these spectra are discussed in the following paragraphs.

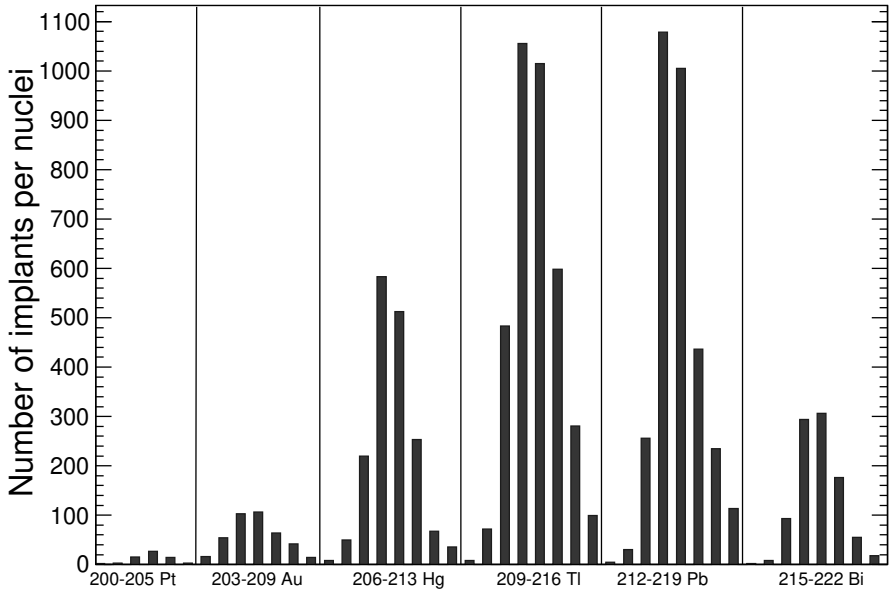

Figure 3.11: Number of implanted nuclei of each isotope. Analyzed ones were those with enough statistics: $^{204-206}$Au, $^{209-211}$Hg, $^{211-216}$Tl, $^{215-218}$Pb and $^{218-220}$Bi

Alpha decays

Alpha lines observed in layers A and B of SIMBA are associated to specific isotopes from the decay chain of some of the implanted ions. A total of 15 alpha peaks have been identified [10] in the measured settings. Table 3.3 shows the energies observed and the corresponding isotope.

Few of these alpha lines overlap with others in the spectra. Their identification has been possible thanks to literature values [10], which allows the understanding of some wide peaks. The peak at 6778.3 keV from the ^{216}Po decay, turned out to be particularly helpful to determine the ^{216}Pb half-life as described in the next chapter. The other main α peaks, including the 3 highest lines in DSSD A (see figure 3.12 top-left), are related to isotopes from previous settings. Some of them are used to calculate the energy calibration coefficients for A and B silicons, in particular the most intense lines at 5869.5 keV and 7450.3 keV for layer A and 5304.3 keV for layer B. They are related to implanted ions of ^{211}At during the ^{205}Bi setting used for isomer tagging identification (see previous chapter).

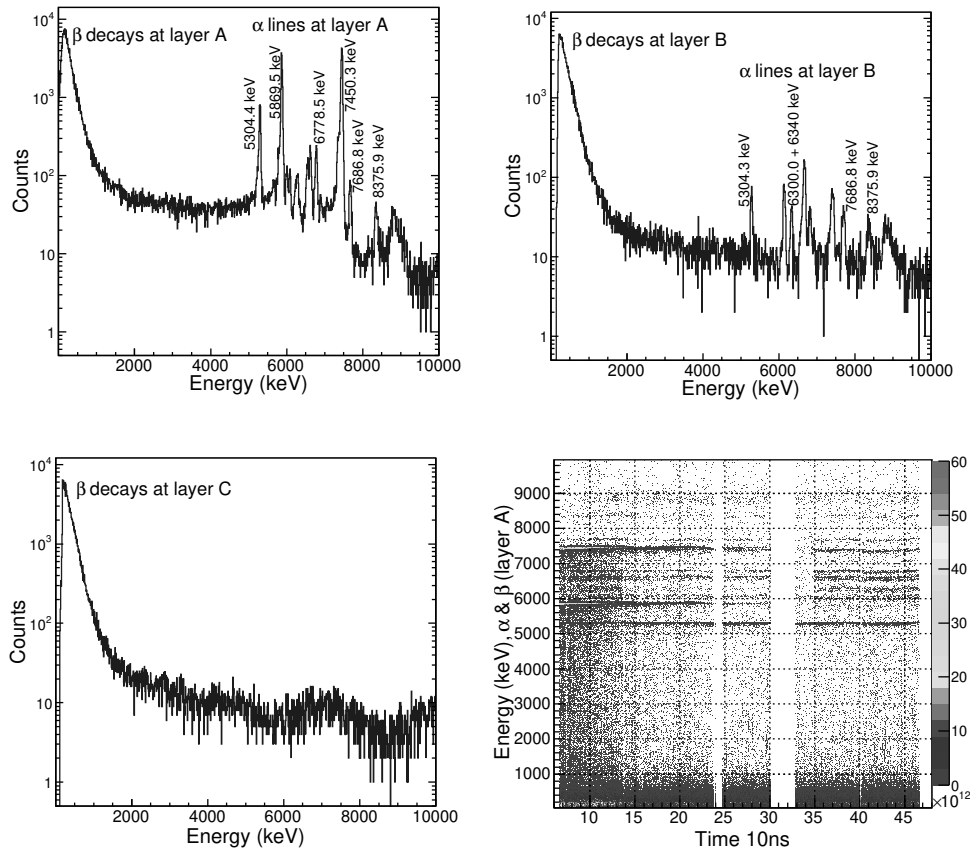

Figure 3.12: Decay energy spectra of SIMBA silicon layers: A (top-left), B (top-right), C (bottom-left). Both α peaks and the β continuum can be appreciated. Bottom-right shows the decay energy spectrum of layer A along the experiment time.

β-decays

The energy deposition of β decays is distributed at low energies and presents, as expected, a continuum spectrum. In order to establish an upper threshold to select β-particles, 2.6 MeV was considered a proper value to separate the β-continuum region from α signals and implants and to prevent possible gain fluctuations.

Electrons in silicon can reach up to few millimeters in the range of few MeV, and thus, implant-β correlations have to include not only the pixels in the implant layer, but also from neighboring DSSD layers. The information of front

α energy (keV)	SIMBA layer	α emitter	Precursor implanted	Setting
5304.3	A, B	^{210}Po	(Implanted)	^{205}Bi
5869.5	A	^{211}At	(Implanted)	^{205}Bi
6002.4	A	^{218}Po	^{218}Bi, ^{218}Pb	^{215}Tl
6050.8	A	^{212}Bi	^{212}Tl	^{211}Hg, ^{215}Tl
6208.0	A	^{219}At	^{219}Bi	^{215}Tl
6288.1	A	^{220}Rn	^{220}Bi	^{215}Tl
6300.0	B	^{212}Bi	^{212}Tl	^{211}Hg, ^{215}Tl
6340.0	B	^{212}Bi	^{212}Tl	^{211}Hg, ^{215}Tl
6537.0	A	^{217}Po	^{217}Pb	^{215}Tl
6622.9	A	^{211}Bi	^{211}Tl	^{211}Hg, ^{215}Tl
6778.5	A	^{216}Po	^{216}Pb	^{211}Hg, ^{215}Tl
7386.1	A	^{215}Po	^{215}Pb	^{205}Bi
7450.3	A	^{211}Po	^{211}At	^{205}Bi
7686.8	A,B	^{214}Po	^{214}Pb, ^{214}Tl	^{211}Hg, ^{215}Tl
8375.9	A,B	^{213}Po	^{213}Tl	^{211}Hg, ^{215}Tl

Table 3.3: Alpha lines observed and identified at SIMBA and their associated nuclei.

and rear SSSD's is not used for position correlation due to their segmentation in only one direction.

3.3 Beta dELayEd Neutron detector

The BELEN detector is a nearly 4π neutron detector, which has been developed at the Universitat Politècnica de Catalunya (UPC) and the Institut de Física Corpuscular (IFIC) [76, 77, 78] and upgraded for this experiment in collaboration with the LISA Helmholtz young investigators group at GSI and the University of Giessen (Germany).

3.3.1 Principle of operation

The detection mechanism of BELEN is based on the collection of the kinetic energy released from the reaction between ^{3}He and thermal neutrons. The neutron thermalization is achieved by means of a polyethylene matrix covering the ^{3}He proportional counters. Specifically, when a thermal neutron is captured by ^{3}He, a tritium and a proton with a total associated kinetic energy of 765 keV are released, following the reaction presented in equation (3.3):

$$^3He + n \longrightarrow ^3H + ^1H + 765\ keV \tag{3.3}$$

In case that this interaction occurs close to the wall of the ^{3}He tube, part of the kinetic energy can be absorbed in the wall, generating a *wall effect*. This is reflected with the long plateau region at low energies, where the energy deposition related to the tritium (^{3}H), at 191 keV, or the proton (^{1}H), at 574 keV can be observed (see figure 3.13).

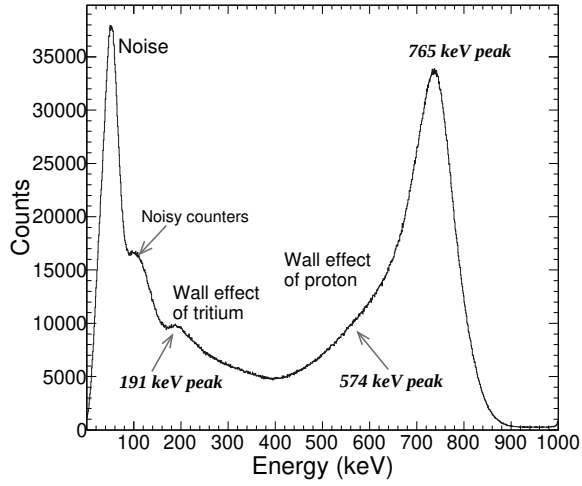

Figure 3.13: Neutron spectrum obtained during the ^{211}Hg setting with BELEN.

3.3.2 BELEN prototypes

All BELEN prototypes consist of an array of ^{3}He counters embedded in a polyethylene matrix. The principle of operation is schematically displayed in figure 3.14. The main difference between each prototype are the number of counters, their geometric distribution and the implantation β detector used [78]. Before the experiment analyzed in this thesis, BELEN was used in two experiments in IGISOL-JYFL (Finland) with 20 counters [49, 79] (see figure 3.15-left). Furthermore, after the present experiment performed at GSI, two more prototypes have been developed and assembled, both of them with 48 counters [77]. One of them was tested in 2013 at PTB in Braunschweig (Germany), to validate the efficiency obtained in the simulations along the energy range up to 5 MeV, shown in figure 3.15-right. The second one was used in new experiments at IGISOL-JYFL, in November 2014 [80, 81]. Table 3.4 summarizes the characteristics of each prototype, including the BELEN-30 version used for this experiment [77]. Note that the efficiency varies depending on the diameter of the central hole, the number of counters and the range of energy where it is desired to obtain a flat efficiency.

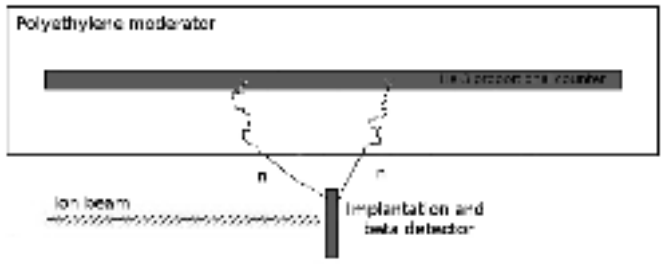

Figure 3.14: Scheme of neutron detection with an ^{3}He proportional counter of BELEN.

3.3.3 Characteristics of the BELEN-30 prototype for this experiment

In the present experiment, the BELEN-30 detector is used to detect and measure the neutrons produced after β-decays of the very neutron-rich nuclei implanted in SIMBA. The configuration for this experiment consists of 30 ^{3}He counters, each one of 2.54 cm diameter and 60 cm effective length, distributed in two rings, as shown in figure 3.16. The rings are concentric around the central hole hosting SIMBA, which is indeed the main constraint for the position of the rings. The inner ring has a radius of 14.5 cm and 10 counters with a pressure of 10 atm. The outer ring has a radius of 18.5 cm and comprises 20 counters at 20 atm. The operating voltages are of 1500 V and 2200 V, respectively. Counters are embedded in a polyethylene matrix of $90 \times 90 \times 80$ cm^3.

Figure 3.15: Left: BELEN-20 detector during the measurements in Jyväskylä (2009), with a HPGe detector. Right: BELEN-48 at the experimental hall of PTB in 2013.

Name	Number of ^{3}He counters	Pressure (atm)	Experiment	Central radius (cm)	Average efficiency up to 2 MeV	5 MeV
BELEN-20	20	20	JYFL-2009	5.5	30%	25%
BELEN-20	20	20	JYFL-2010	5.5	43%	38%
BELEN-30	20+10	20, 10	GSI-2011	11.5	38%	33%
BELEN-48	40+8	8, 10	PTB-2013 JYFL-2014	5.5	40%	39%

Table 3.4: Characteristics of the BELEN developed prototypes.

The outer layers of polyethylene act as a shielding against neutron background from the surroundings. The total weight of the detector is of about 600 kg.

3.3.4 Experimental efficiency calibration

According to MCNP simulations [77], the neutron efficiency for this BELEN prototype is estimated to be between 38 % and 40% depending on the Q_β-value of the analyzed isotope (see table 3.4). The energy dependency of the efficiency is rather flat in the range of interest from thermal to 2 MeV, as shown in figure 3.17 [77]. In order to confirm the simulated efficiency experimentally, during the experiment a measurement with a spontaneous fission source of ^{252}Cf was performed. The efficiency measured at 2.35 MeV, which is the average neutron energy is in agreement with the value of the simulation in this energy.

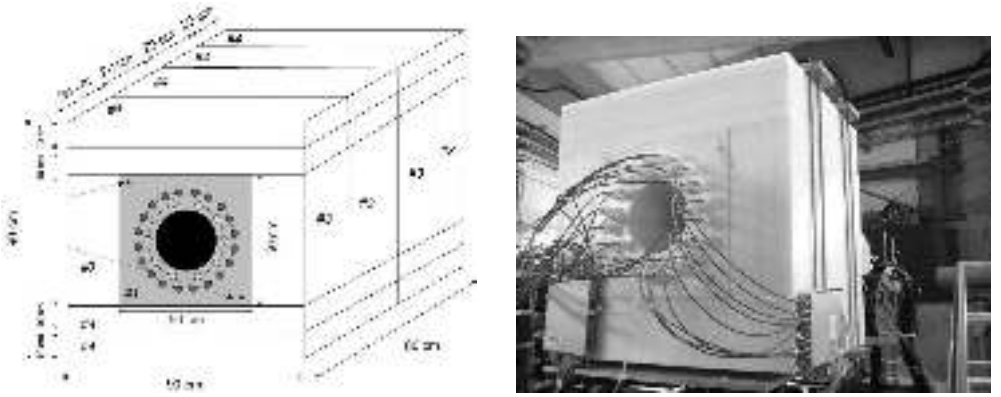

Figure 3.16: Left: Scheme of the 30 ^{3}He counters distributed in the polyethylene matrix. Right: Image of BELEN detector during the experiment. Red cables connect the counters and the preamplifiers.

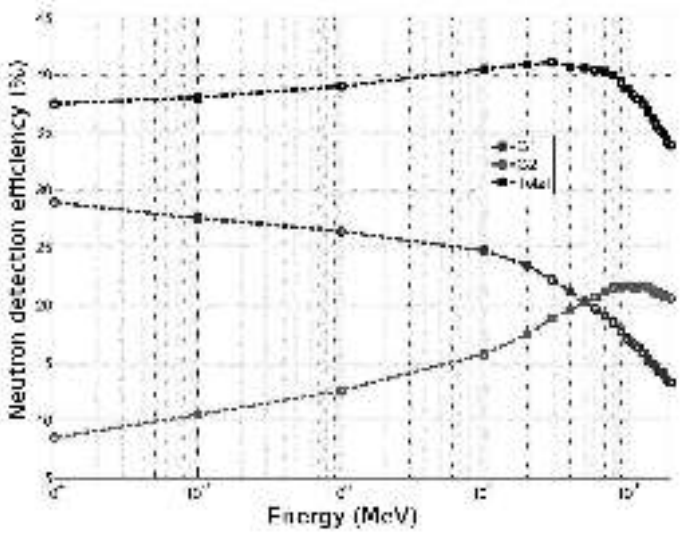

Figure 3.17: Neutron efficiency up to 2 MeV according to the MCNPX simulation of this BELEN prototype. Upper line is the total efficiency which can be considered flat up to 2 MeV with an average value of 38%. The other two curves correspond to the contribution of each ring, inner (higher at lower energies) and outer (increasing the efficiency at high energies).

3.3.5 BELEN signal processing and the Digital Data Acquisition System (DDAS)

The neutrons detected with BELEN were registered using a self triggered acquisition system specifically developed for the BELEN detector [50], named Digital Data Acquisition System (DDAS) in this experiment.

The pulses from the ^{3}He tubes are processed using an electronic chain which consisted of a preamplifier with a differential signal output, followed by an amplifier that gives an unipolar signal shape. The output of the amplifier is sent to the ADC digitizers of Struck SIS3302-VME, shown in figure 3.18. Digitizers store the energy deposited and the time of each neutron event, filling their memory buffer for each channel associated to an ^{3}He counter and saving the data in the disk. This innovative acquisition system allows to obtain an almost negligible dead-time, reduced to less than 0.5%, while at the same time providing accurate time-stamps of all events. The DDAS system was integrated into the Multi Branch System (MBS) [82], used at GSI for acquiring data of all FRS tracking detectors.

Apart from monitoring each neutron detection, DDAS also introduce a common time clock signal, with 10 ns repetition rate, to the MBS system as a time reference for all triggers.

On the other hand, during the experiment we used an online data visualizer software named GSI Object Oriented On-line Off-line system (GO4) [83]. It allowed to control all signals and to check for unexpected problems during the acquisition.

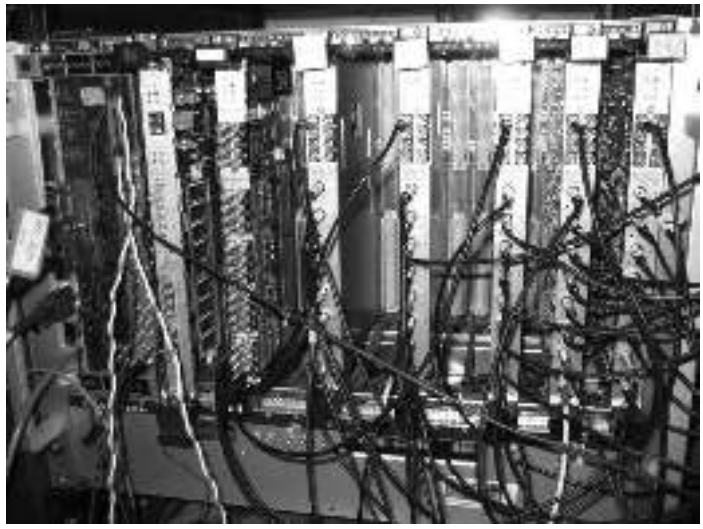

Figure 3.18: Image of the DDAS system VME crate where SIS3302 digitizers modules can be observed with their eight channels and other trigger and time signals connected.

3.4 Neutron contaminants and background characterization

Two different sources of neutron background were identified in test runs carried out at GSI-FRS few months before this experiment. The first background component is due to stray neutrons which are scattered around in the experimental hall and eventually reach the ^{3}He-tubes producing a contaminant signal. In order to suppress this background blocks of polyethylene with a thickness of 20 cm were placed around BELEN detector. The second component of neutron background is due to reactions induced by the charged ions along the last elements of the FRS, such as knockout reactions in the *sci*21, or the Al-degrader at S4. In order to reduce this background contribution a polyethylene wall with a thickness of 30 cm was placed a few cm in front of BELEN (see figures 3.1-left and 2.6). To let the ion beam fly into the implantation detector, a hole of 180 mm in X-direction and 70 mm in Y-direction was made in this shielding wall. In addition, to enhance the shielding efficiency of this polyethylene-wall, a rubber layer with boron was placed between the wall and the front face of BELEN.

Thanks to this twofold shielding approach, the neutron background conditions improved noticeably. A further reduction of background events was achieved at the analysis stage by setting a veto-time gate in the ion-neutron correlation distribution, as it is explained in the section below.

3.4.1 Neutrons induced by ions through FRS

In principle, contaminant neutrons induced by direct reaction of the ions passing through materials along the FRS could be excluded by using the signals from *sci*41 and building time correlations with the detected neutrons. After implementing this condition in the data analysis the background level improved remarkably, but there was still a certain amount of detected neutrons, which were not related to β-decays. The latter component was very efficiently suppressed by using the $TPC41$. Indeed, it turns out that the sensitive area of the TPC is larger than that of the *sci*41. Thus, although the intrinsic efficiency for ion detection of the *sci*41 is almost 100%, there is a fraction of ions (and possibly other charged particles) which are not detected in *sci*41, but still produce background neutrons. Most of these events could be rejected by building a time correlation between detected neutrons and the trigger signals from the TPC, as shown in figure 3.19. This was possible by feeding and time-stamping one of the TPC-signals in DDAS. Finally, a time-exclusion window of 600 μs (-100 to 500 μs) was used to avoid this kind of background events.

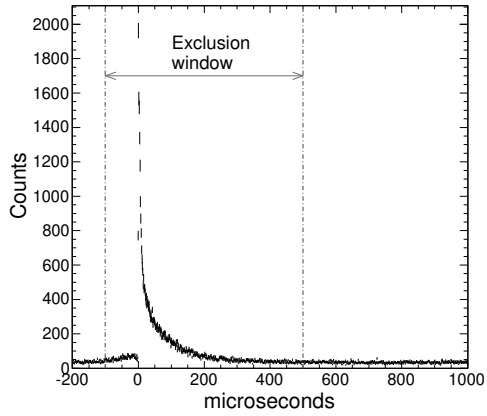

Figure 3.19: Ion through the FRS detected at TPC with the correlated neutrons

3.4.2 Neutron bunch correlated with the beam injection to ESR

Another unexpected neutron source was related to the parasitic beam delivered by another experiment at the ESR facility, located next to the S4 experimental hall. This was observed thanks to the high efficiency of BELEN that, when beam from the ESR was dumped to the extraction point of ESR, a short bunch of neutrons was detected in BELEN. Therefore an ESR trigger signal was also included in DDAS and correlated with neutrons. The neutron events related with this phenomenon were also discarded in the analysis. Figure 3.20 shows the periodicity of the spills generated by the ESR trigger, and a detailed zoom highlighting the region of a certain random spill.

3.4.3 Neutrons correlated with the spill

Despite the extra shielding and the neutron background rejection methods described above, the amount of neutrons detected during the spill, as shown in figure 3.21, was very large. For this reason only the β-neutron events during the off-spill periods were taken into account in the data analysis (see chapter 4). In order to do so, the time of trigger signals that indicate the stop of each beam spill was used.

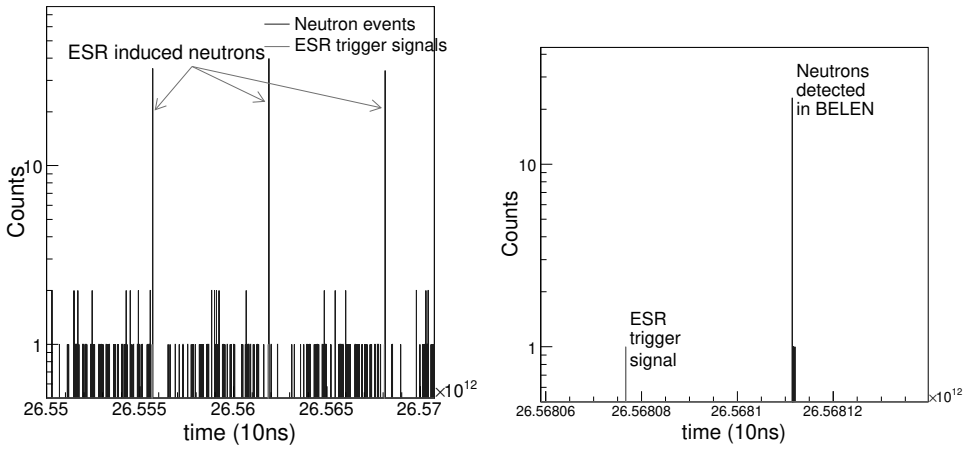

Figure 3.20: Left: Example of several ESR trigger signals (red) and neutrons (blue) for a random interval of time. The correlated neutrons appeared registered in DDAS just 347.2 ms after the ESR trigger. The right figure shows a zoom where the ESR trigger signal (in red) can be observed together with its correlated bunch of neutrons.

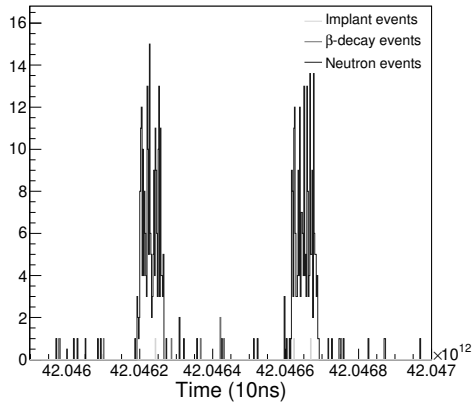

Figure 3.21: Implant, β-decays and neutron events in a random interval of time where it can be appreciated the bunch of background neutrons correlated with the beam spill.

Chapter 4
Analysis and results

The analysis methodology followed in this work to determine half-life and neutron branching ratios of implanted isotopes is similar to the approach successfully applied in previous works both at isol- and fragmentation facilities [39, 50, 72]. In order to establish a consistent analysis procedure adapted to the conditions of the GSI RIB facility and to the characteristics of our detection and acquisition systems, a systematic study of the influence of all possible parameters has been carried out. By order of relevance, the latter effects comprise,

i) background characterization,

ii) all and off-spill implant-β time-correlations,

iii) implant-β correlation area,

iv) bin time-width in the implant-β time distribution, and

v) total implant-β correlation time.

After a brief introduction to the analytical expression, which describes the time-dependency of the implant-β correlations, a detailed description of the aforementioned effects is presented together with the final half-life and neutron-branching results for each nucleus. In this chapter an experimental validation of the analysis method is reported, which is based on a comparison between implant-α and implant-β time correlations, in a similar fashion as reported in [84].

4.1 Analytical model for implant-β correlations

Using the PID described in section 2.3, implant events for one particular isotope can be selected. The position of each implanted nucleus is typically determined with an accuracy of ± 1 mm^2, i.e. one pixel in a silicon layer at SIMBA. Selecting β-events detected in SIMBA in a correlation region around the implant position, we can build time correlations. Contributions from decays of other nuclei implanted before or right after the isotope of interest, in the same correlation region can be neglected. The latter assumption is well justified by the very low total implantation rate of 0.114 ions/s, which means an average

of 20×10^{-6} ions/s/pixel. Due to a non-homogeneous implant distribution in SIMBA the rate per pixel varied between 100×10^{-6} ions/s and 10×10^{-6} ions/s.

In order to determine the value of the half-life several approaches were investigated. In all cases, the analysis is based on the Bateman equations [85]. It was assumed that only the parent and daughter decays are contributing to the activity decay curve (see equation (4.1)). This assumption is justified because all granddaughters correspond to stable nuclei or to very long lived isotopes.

$$\sum_{i=1}^{N} \lambda_i N_i(t) \approx (\lambda_1 N_1(t) + \lambda_2 N_2(t)) \tag{4.1}$$

$N_i(t)$ is the number of nuclei for each isotope i at certain time t, $\lambda_1 = ln(2)/T_{1/2}$ is the decay constant for the implanted nucleus with an unknown half-life $T_{1/2}$ and λ_2 is the decay constant for the daughter nucleus, which is known for all implanted species, with the only exception of ^{219,220}Bi, which is treated as described in subsection 4.7.2.

The first analysis strategy studied consisted of using implant-β time- correlations taking only the first β-event detected in the selected region around the implant location after each ion-implant (in the following 1^{st}-β method). Assuming a constant uncorrelated background rate b, the probability density-function, which describes the time-dependency of the correlation distribution, is given by equation (4.2) [86],

$$\begin{aligned} \rho(\lambda_1, t) = {} & (1-\varepsilon_\beta)^2 b \mathrm{e}^{-bt} \\ & + \varepsilon_\beta \left(1 - (1-\varepsilon_\beta)\frac{\lambda_2}{\lambda_1 - \lambda_2}\right)(b+\lambda_1)\mathrm{e}^{-(b+\lambda_1)t} \\ & + \varepsilon_\beta (1-\varepsilon_\beta)\frac{\lambda_1}{\lambda_1 - \lambda_2}(b+\lambda_2)\mathrm{e}^{-(b+\lambda_2)t} \end{aligned} \tag{4.2}$$

where ε_β is the β-detection efficiency in SIMBA. According to this probability density-function, for a certain number of implanted events ($N_1(0)$), the total number of detected β-particles N_β at a time t with respect to the implant time ($t = 0$) is given by equation (4.3).

$$\begin{aligned} N_\beta^{1^{st}\beta}(t) &= N_1(0) \cdot \rho(\lambda, t) \cdot \Delta t \\ &= (\varepsilon_\beta \lambda_1 N_1(t) + \varepsilon_\beta(1-\varepsilon_\beta)\lambda_2 N_2(t) + (1-\varepsilon_\beta)^2 b \mathrm{e}^{-bt}) \cdot \Delta t \end{aligned} \tag{4.3}$$

where Δt corresponds to the bin time-width used in the implant-β time-correlations.

However, for the present analysis, this correlation method has two main disadvantages. The first one is the dependency on the β-detection efficiency ε_β. This quantity depends on a number of experimental effects such as the precise implantation depth in the silicon layer or the electronic noise (threshold) of

the involved silicon strips. It also depends on physical properties of the decay such as its Q_β-value or even the details of the β-strength distribution. Monte Carlo simulations can be carried out in order to estimate the value of the β-detection efficiency, although with a relatively large systematic uncertainty. Additionally, correlations using only the first β event can be strongly biased when the β-background rate is high and also by time-dependent β-backgrounds characteristic of the pulsed beam-structure of GSI-FRS. Such, β-backgrounds may provide systematically low values for the value of the analyzed half-life.

Most of these disadvantages can be overcome when, instead, correlations with all detected beta-events over a sufficiently broad time-window ($\gg T_{1/2}$) are considered. In this case, the expression which describes the time-correlation probability function is also given by [86]:

$$\rho(\lambda_1, t) = \varepsilon_\beta b + \varepsilon_\beta \lambda_1 \mathrm{e}^{-\lambda_1 t} + \varepsilon_\beta \frac{\lambda_1 \lambda_2}{\lambda_1 - \lambda_2}\left(\mathrm{e}^{-\lambda_2 t} - \mathrm{e}^{-\lambda_1 t}\right) \tag{4.4}$$

The function which describes the accumulated distribution for implant-β correlations taking into account the β efficiency is presented in equation (4.5). In this case, all contributions are affected by the same β efficiency factor, including the β-background correlation, being the resulting correlation fit independent of it.

$$\begin{aligned} N_\beta^{All_\beta}(t) &= N_1(0) \cdot \rho(\lambda, t) \cdot \Delta t \\ &= (\varepsilon_\beta \lambda_1 N_1(t) + \varepsilon_\beta \lambda_2 N_2(t) + \varepsilon_\beta b) \cdot \Delta t \\ &= \varepsilon_\beta (\lambda_1 N_1(t) + \lambda_2 N_2(t) + b) \cdot \Delta t \end{aligned} \tag{4.5}$$

Where $N_\beta^{All_\beta}(t)$ is the total number of detected decays at a time t, N_i the number of nuclei of each isotope in the chain, b is the β-background corrected by ε_β and Δt the bin time-width of the implant-β time-correlations. $N_1(t) = N_1(0) \cdot \mathrm{e}^{-\lambda_1 t}$ and $N_2(t) = N_1(0) \cdot \frac{\lambda_1}{\lambda_1 - \lambda_2}\left(\mathrm{e}^{-\lambda_2 t} - \mathrm{e}^{-\lambda_1 t}\right)$. $N_1(0) \cdot \varepsilon_\beta$ is estimated by using the first bin of the implant-β correlation and distribution determined within the Maximum-Likelihood (ML) analysis (see below) and thus, the time dependent factor of the adjusted expression, $\lambda_1 N_1(t) + \lambda_2 N_2(t) + b$ does not depend on the β-efficiency. The latter represents the main advantage of this approach, when compared to the 1^{st}-β method (see equation (4.3)), where a time-dependency on ε_β exists. This is reflected in systematically more accurate results for the adjusted half-life value. Finally, the half-lives of the involved isotopes are particularly large, in some cases exceeding 100 s. The implemented digital acquisition system (section 3.3.5) is therefore well suited for the implementation of this analysis method, because every event is time-stamped and thus, a correlation over an arbitrarily long time-window can be performed.

As described above, there are several elements in the analysis, which may influence the sensitivity and the accuracy of the final result. For this reason

a thorough systematic study has been carried out, which is reported in the following sections.

4.2 ^{213}Tl analysis as method benchmark

In order to establish a reliable procedure for the data analysis, the thallium isotope ^{213}Tl is taken as reference owing to its relatively large implantation statistics (1015 implants). Its high statistics ensure that the analysis conditions thus determined are not affected by possible statistical fluctuations in the correlation spectra.

4.2.1 Background characterization

The background rate of β-like events during the experiment is the quantity that limits the attainable detection sensitivity and therefore, a proper treatment of it becomes important for the reliable analysis of the decay half-life. Furthermore, the pulsed beam-structure of GSI-FRS induces a very different background level during beam extraction from the SIS-synchrotron (spill on) and after it (spill off). For this reason, special care has been taken in the data analysis to understand the influence of the beam-structure in the implant-β correlation distributions and to properly handle such dependency.

In general terms, there are two different methods to characterize the background in this kind of experiments. The first one is based on the so-called virtual-implant approach (see e.g. [87,88]), which is schematically illustrated in figure 4.1-left. This method is based on the use of implant-β time-distributions built using β-events detected sufficiently far from the implant region. A sufficiently large implant-β distance ensures that such time-distribution corresponds to background events that are not correlated with the implanted ion. However, a simple inspection of the spatial distribution of β-events (figure 4.1-right) shows the deficiency of this approach for the present experiment. Since it is not a uniform distribution, the so-determined background level is not representative of the true background level in the implantation region, which in turns depends on each particular isotope.

In order to overcome this problem an alternative approach has been applied in this work. It is based on time-reversal or time backward implant-β correlations using only the pixels within the correlation region. The latter condition ensures that the so-determined background level becomes representative of the β-background in the area of interest used for time-forward implant-β correlations. The background level thus determined allows one to adjust the parameter b in equation (4.4), which has a flat dependency in time. This is demonstrated in figure 4.2, which shows implant-β time-correlations both in forward ($t > 0$) and backward ($t < 0$) time directions for ^{213}Tl. For the present discussion let us concentrate on the negative time-interval of these diagrams,

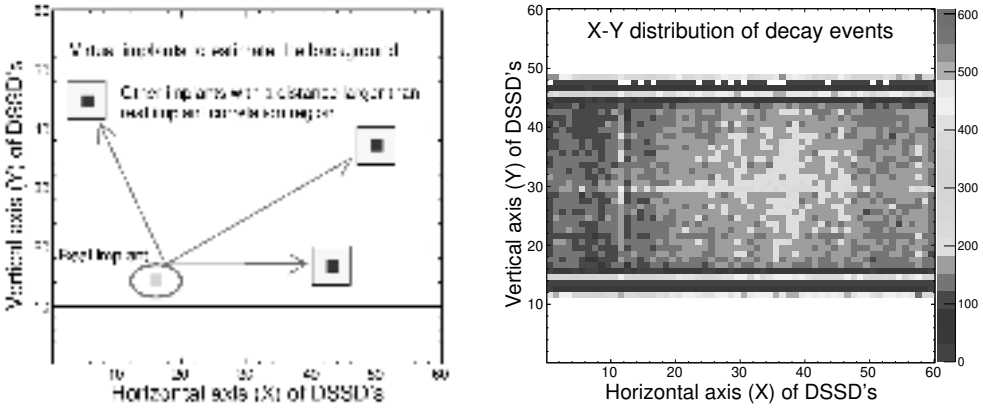

Figure 4.1: Left: scheme of implant-β correlations background analysis with the virtual implants method. Right: decay distribution along vertical and horizontal XY axis at SIMBA. It can be observed that decays are not homogeneous along the silicon.

which represents the backward (uncorrelated) background contribution. Figure 4.2-left shows implant-beta correlations including all β-events over a time window of $\pm$360 s for each implant event. In the following this approach will be designated as all-β correlations method. In this case of ^{213}Tl, an average background rate of $b = 2$ counts/s has been obtained using only the negative part of the diagram (-360 s to 0 s). Figure 4.2-right shows the same correlation using only beta-events outside of the beam-spill, in the following off-spill correlations method. In the latter case an average background rate of $b = 1.4$ counts/s is obtained for the same time interval. The higher background rate in the former case indicates the aforementioned effect of enhanced β-like background during the beam-spill interval.

4.2.2 All and off-spill correlation methods

Here the effect of the specific correlation approach in forward time direction, which includes both correlated and uncorrelated events, will be discussed. To this aim, the background parameter b previously determined will be fixed for each correlation distribution and will be used in order to adjust the value of the unknown parameter λ_1. Given the generally limited amount of statistics, the approach best suited for this analysis is the binned Maximum Likelihood (ML) algorithm [89]. In order to implement it, the present analysis equation (4.5) was included in a ROOT/C++ program in combination with the RooFit CERN-library [90]. Figure 4.3 shows the result of the analysis after the convergence of the ML algorithm for the same distributions already shown in figure 4.2.

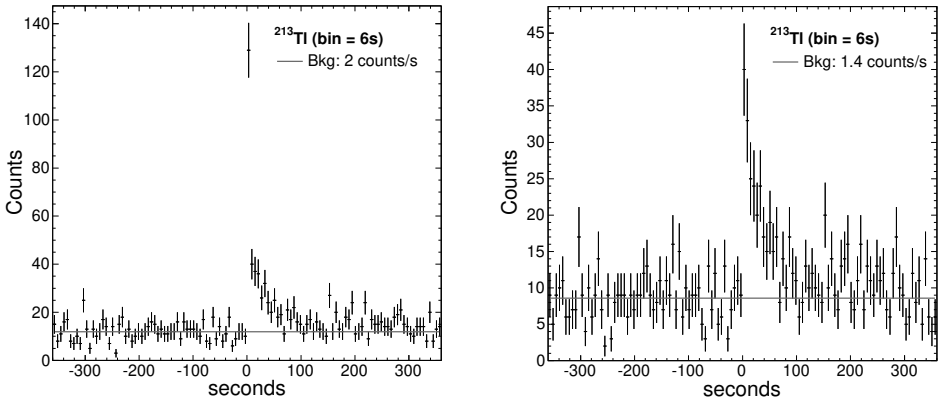

Figure 4.2: ^{213}Tl implant-β time correlations in a time-interval of $\pm$360 s around the implant-time. (Left) Correlations with all β-events. (Right) Correlations with all β-events outside of the spill-interval. See text for details.

This example corresponds to a symmetric correlation area using only the first closest pixel to the implant position, which corresponds to a total correlation area of 9 mm^2. The bin-width in this case is of 6 s. The effect of the correlation area and the bin-width will be described in the following sections.

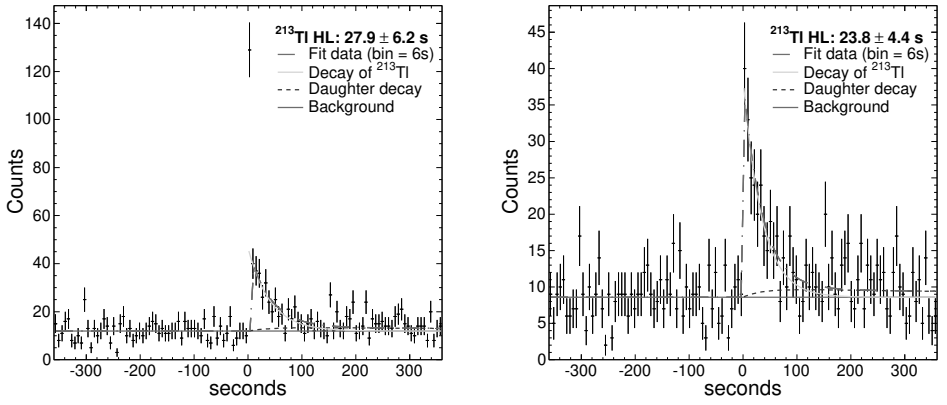

Figure 4.3: ML analysis of the ^{213}Tl implant-beta correlations. Left: All implant-β events. Right: implant-β events off-spill. See text for details. HL is defined as the half-life for this case and all shown correlations.

The first aspect that has to be discussed is the very large number of counts in the first bin of the all-correlation distribution (see figure 4.3-left). The discrepancy between this data-point and the analysis model is due to the fact that the difference between the β-background rate inside and outside the spill has

not been included in the analytical description. Thus, an important contribution from in-beam β-like events is observed in the first bin of the correlation spectrum, which is not accounted for in the model. This effect can be cured by excluding the first bin from the fit-range. The result shown in figure 4.3-left already includes this consideration. Indeed, the half-life value obtained using both correlation approaches, $T_{1/2} = 28\pm6$ s and $T_{1/2} = 24\pm4$ s respectively, are in perfect agreement within the quoted statistical uncertainty. The goodness of the analytical model in both cases is indicated by the reasonable reduced χ^2-value (χ^2/NDF) obtained, which is of 2.21 and 1.40, respectively.

4.2.3 Implant-β correlation area

Depending on the average range of β-particles in SIMBA silicon detectors (A, B and C), and the rate of β-like background events, an optimal correlation area can be determined, which maximizes the peak-to-background P/B ratio. In order to determine it, figure 4.4 shows the ^{213}Tl implant-β correlations for several symmetric correlation areas of 9 mm^2, 25 mm^2 and 49 mm^2 around the implant location and for both types of correlation, all-β-events (left) and spill-off β-events (right). These correlation areas correspond to the one-, two- and three-closest pixels around the implant location.

In order to evaluate the goodness of each correlation area the P/B ratio together with the χ^2-value (χ^2/NDF) obtained for each case are listed in table 4.1.

Correlation area (mm^2)	All β-events		Off-spill β-events	
	P/B	χ^2	P/B	χ^2
9	1.32	2.21	1.34	1.40
25	1.14	1.99	1.11	1.24
49	1.05	1.87	1.04	1.27

Table 4.1: Peak-to-Background ratio and χ^2-value (χ^2/NDF) for the implant-β correlation diagrams shown in figure 4.4.

In summary, it can be concluded that a correlation area of 9 mm^2 (the 3×3 pixels around the implant) seems the most convenient in terms of sensitivity to the decay curve. In this case the P/B-ratio becomes a factor about 20% larger than areas of 25 mm^2 and 49 mm^2. The case of 1 mm^2 has been also evaluated but the limited statistics of many isotopes makes this a worse option. It can be also concluded that 9 mm^2 off-spill correlations are better suited for the half-life determination than all β-events approach, mainly because of the slightly better χ2-values.

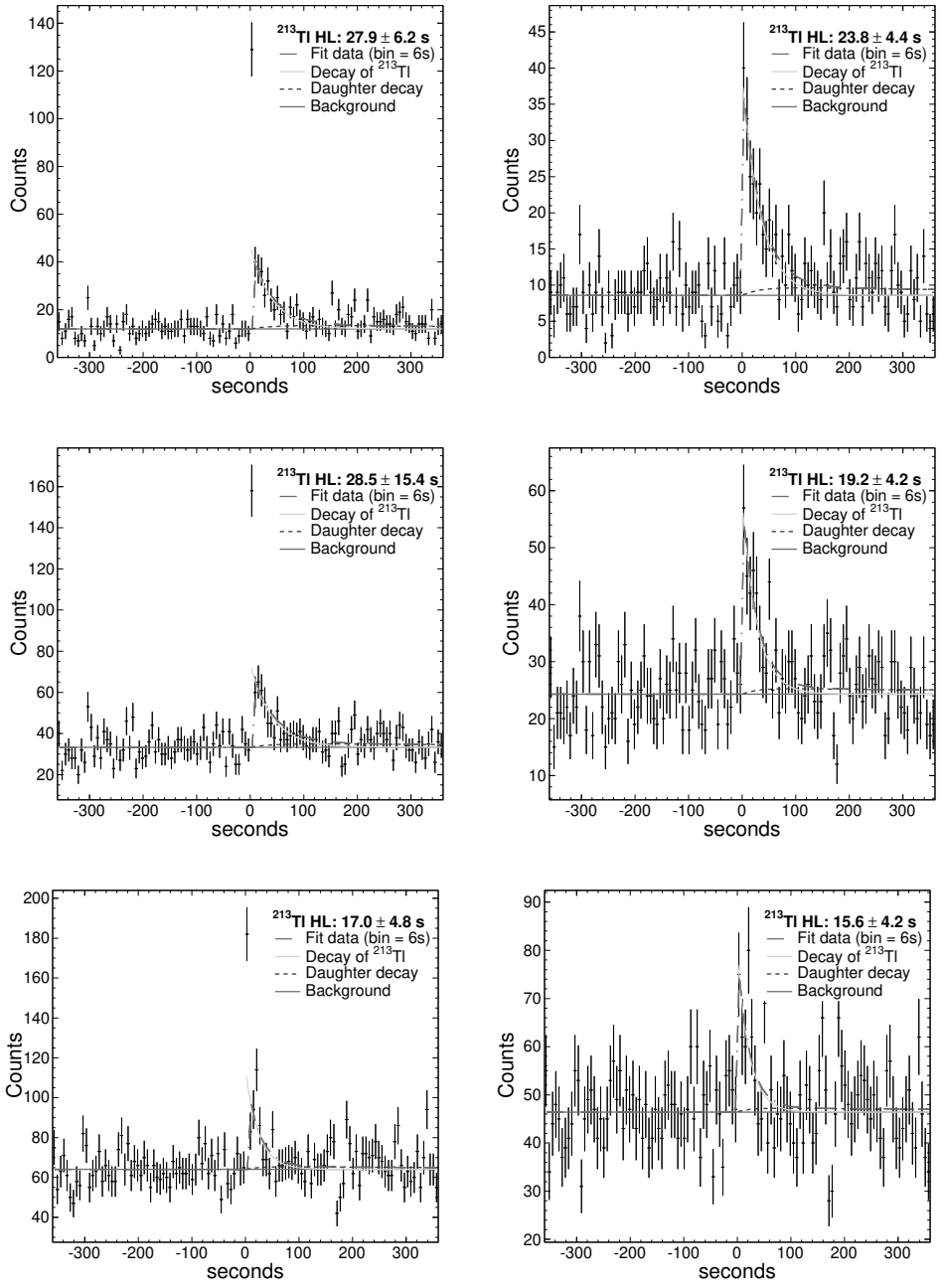

Figure 4.4: ^{213}Tl implant-β correlation distributions. Left: all β-events method. Right: Off-spill approach. From top to bottom the correlation areas are of 9 mm^2, 25 mm^2 and 49 mm^2.

Finally, it is worth emphasizing the consistency of the result obtained for the half-life of ^{213}Tl for all possible analysis conditions within the quoted statistical uncertainties.

4.2.4 Bin time-width in the implant-β time distribution

Another aspect to be considered in the analysis method is the binning time width, specially to show more clearly the effect of the β-decay curve in the correlation diagrams. Figure 4.5 shows four analysis for the implant-β correlation of ^{213}Tl with different bin widths. As can be observed all half-life values obtained are compatible within the quoted statistical uncertainties, even if a large bin width close to the half-life value (bottom-right) is used. Thus, the variation of the bin time-width within reasonable values, as expected, does not affect the half-life value obtained. Comparing all considered cases (2, 6, 8 and 18 s), one can conclude that, in general, for those isotopes with large statistics the optimum value is around $1/3 \sim 1/4$ times the expected half-life. In cases with low statistics a rather broad bin time-width will be preferred in order to better disentangle the decay curve from the background.

4.2.5 Total implant-β correlation time

For all isotopes it was found that a total correlation time between ten to fifteen times the half-life value provides consistent results. Figure 4.6 shows this consistency by comparing the ^{213}Tl fit results along 240 s (left) and 360 s (right) of correlation time, obtaining a $T_{1/2} = 22.5 \pm 4.1\ s$ ($\chi^2 = 1.07$) and a $T_{1/2} = 23.8 \pm 4.4\ s$ ($\chi^2 = 1.40$), respectively.

4.2.6 Other analysis aspects

The uncertainty in the daughter half-life parameter λ_2 in equation (4.4) has been consistently taken into account in the correlation analysis. Its impact on the adjusted parent half-life was negligible in all analyzed cases. It means that for all analyzed isotopes the variations of the daughter half-life within quoted uncertainties are not affecting the determination of the parent half-life.

To summarize the systematic method for the analysis of the isotopes in this experiment, the half-lives have been obtained with the following characteristics:

- A constant background value b determined according to the backward β-events, with the same time-range and area-correlation as for the forward β-events.
- Correlations with all β-events off-spill.
- Implant-β correlation area of 9 mm^2, i.e. one pixel around the implantation pixel.

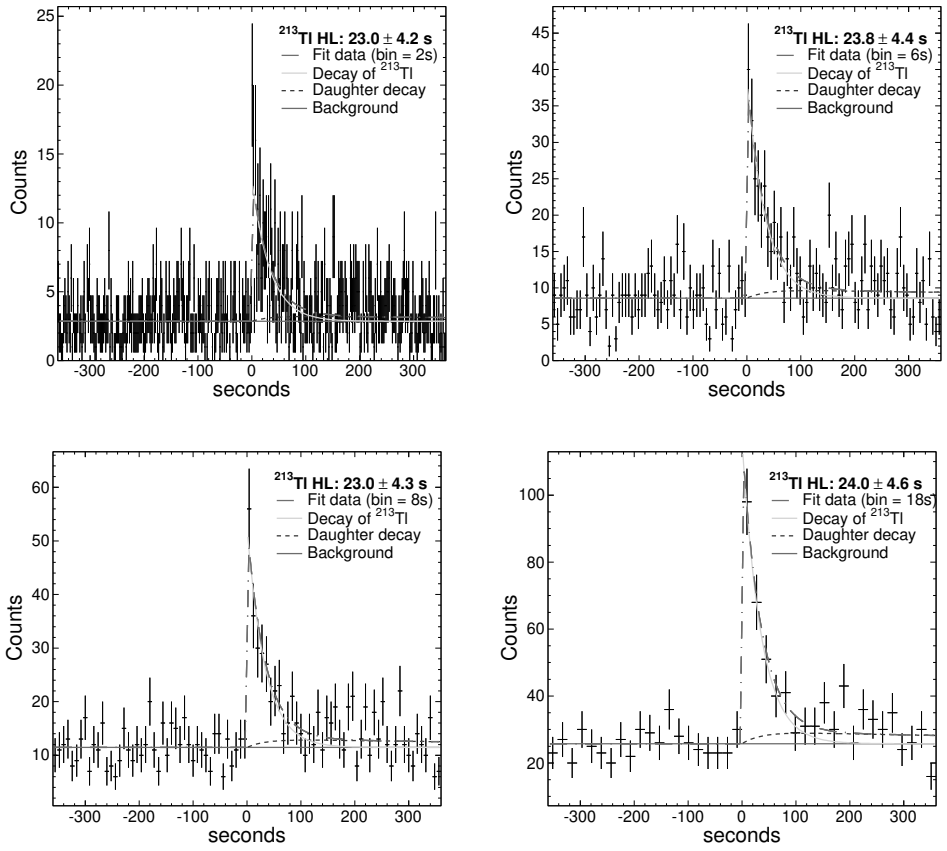

Figure 4.5: ^{213}Tl half-life fits of implant-β events off-spill with a 9 mm^2 correlation area around the implant. Top-left with a binning time width of 2 s, top-right 6 s, bottom-left 8 s and bottom-right 18 s.

- A bin time-width between 1/4 and 1/2 of the expected half-life, depending mainly on available statistics.
- A correlation time-range between 10 to 15 times the expected half-life.

Finally the half-life value for ^{213}Tl determined in this experiment is presented in figure 4.6-right and has the value $T_{1/2} = 23.8 \pm 4.4\ s$.

4.2.7 β-delayed neutron emission probability (P_n) determination for ^{213}Tl

In order to determine the P_n value, all implant-β correlation events have been analyzed by opening a correlation window of 400 μs forward and backward in

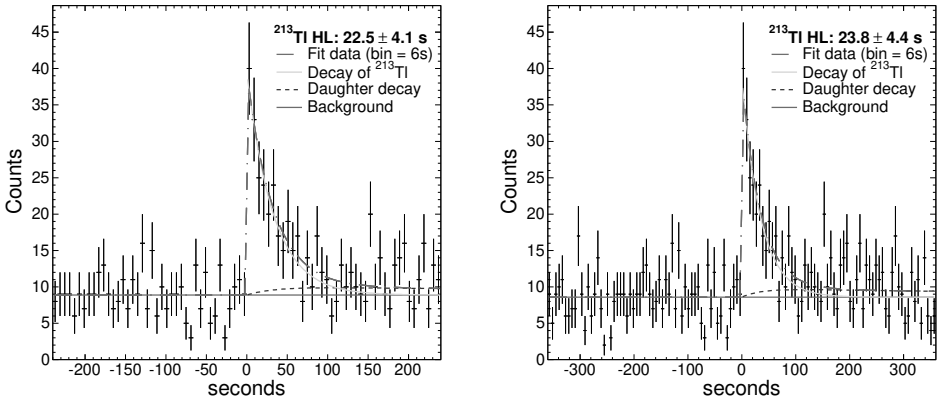

Figure 4.6: ^{213}Tl half-life fits varying the correlation time-range.

time to detect correlated neutron events. This time window is determined according to the expected neutron moderation time in polyethylene, to maximize the neutron detection efficiency.

Considering the β efficiency ε_β as a constant value along the range of energies, the P_n-value can be directly obtained from the subtraction of time-forward and time-backward β-neutron correlated events, representing the time-backward neutrons the background. Following equation (4.6), this subtraction, together with the amount of correlated implant-β decay events and the BELEN efficiency, provides P_n value:

$$P_n(\%) = \frac{1}{\varepsilon_n} \frac{N^{fwd}_{\beta-n} - N^{bkd}_{\beta-n}}{N_\beta} \cdot 100 \tag{4.6}$$

Where ε_n is the BELEN neutron efficiency, $N^{fwd}_{\beta-n}$ the number of forward correlated implant-β-neutron events and the N_β the number of parent β-decays. $N^{bkd}_{\beta-n}$ is the backward β-neutron correlations, considered as background. For the uncertainty calculation we take into account the contributions of statistical errors of $N^{fwd}_{\beta-n}$, $N^{bkd}_{\beta-n}$ and N_β, and the error of the BELEN detector efficiency ε_n. The latter can be considered flat along the energy range of interest according to the Q_{bn}-values of the implanted isotopes (100 keV - 2 MeV), with a constant value of 38% with an uncertainty of 5%, as detailed in subsection 3.3.4 in the previous chapter.

In all analyzed isotopes with $Q_{\beta n} < 0$ either no neutrons have been detected, or the subtraction of forward and backward events makes the result compatible with a $P_n = 0\%$. For those isotopes with very low neutron statistics, such that the one σ statistical uncertainty was larger than the measured value, an upper limit given by the P_n-value plus σ is provided.

In the analysis it was also checked that the neutrons detected with different implant-β correlation times and areas (9 to 25 mm^2), yield consistent results.

The data analysis confirms the ^{213}Tl as a clear neutron emitter. The P_n-value obtained is of 7.6 ± 3.4 %, which corresponds to 5 correlated neutrons with no single neutron event over the same time interval backward (figure 4.7).

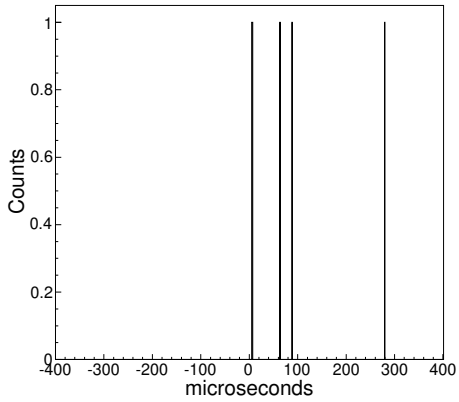

Figure 4.7: β-neutron correlation events during the ^{213}Tl implant-β correlation time within an area of 9 mm^2.

4.3 Thallium isotopes: $^{211-216}$Tl

4.3.1 Analysis of ^{211}Tl and ^{212}Tl

Both isotopes have good implantation statistics, with 483 events of ^{211}Tl and specially the case of ^{212}Tl with 1056 implants. The analysis of implant-β correlation diagrams is presented in figure 4.8. The left one shows the analysis of ^{211}Tl, obtaining a half-life of $T_{1/2} = 76.5 \pm 17.8$ s ($\chi^2 = 1.05$). The right shows the ^{212}Tl result, with a half-life of $T_{1/2} = 30.9 \pm 8.0$ s ($\chi^2 = 1.21$). The bin width is of approximately a quarter of the value expected for the half-life.

Concerning the neutron emission probability (P_n), both cases have a unique neutron event in forward time direction correlated with an implant-β measured with BELEN. No background event was registered over the same time window. Applying equation (4.6) and taking into account the corresponding uncertainties, P_n upper limits of 4.4 % and 3.7 % are estimated for ^{211}Tl and ^{212}Tl, respectively. Figure 4.9 shows the implant-β-neutron time distribution for ^{212}Tl, showing the single neutron event detected.

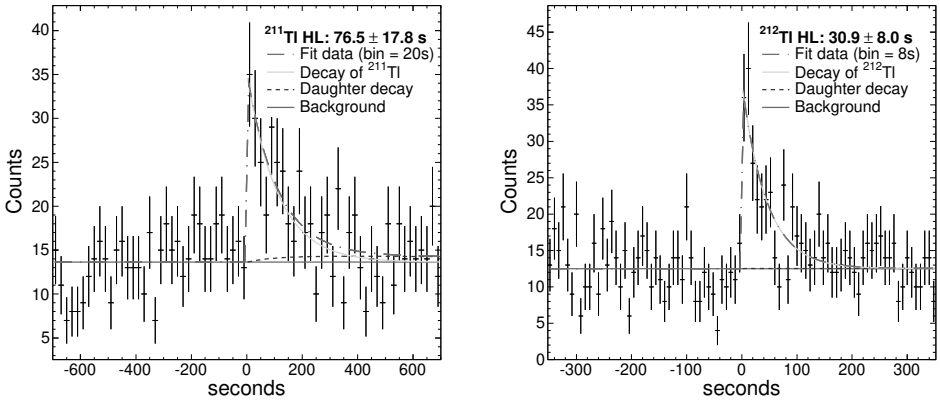

Figure 4.8: ^{211}Tl (left) and ^{212}Tl (right) implant-β correlation diagrams with the half-life fits.

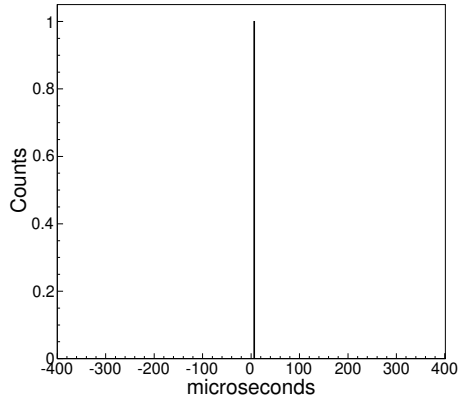

Figure 4.9: ^{212}Tl implant-β-neutron correlation events measured.

4.3.2 Analysis of ^{214}Tl

This isotope was implanted with sufficient statistics (598 implants), yielding the analysis of the decay curve a half-life of $T_{1/2} = 11.1 \pm 2.5$ s (see figure 4.10-left). Concerning the neutron branching ratio, as shown in figure 4.10-right, nine implant-β-neutron events have been detected during the implant-forward-time, and one event in backward-time. This gives a P_n of 27.4 ± 10.9 %, being the largest value measured in this work.

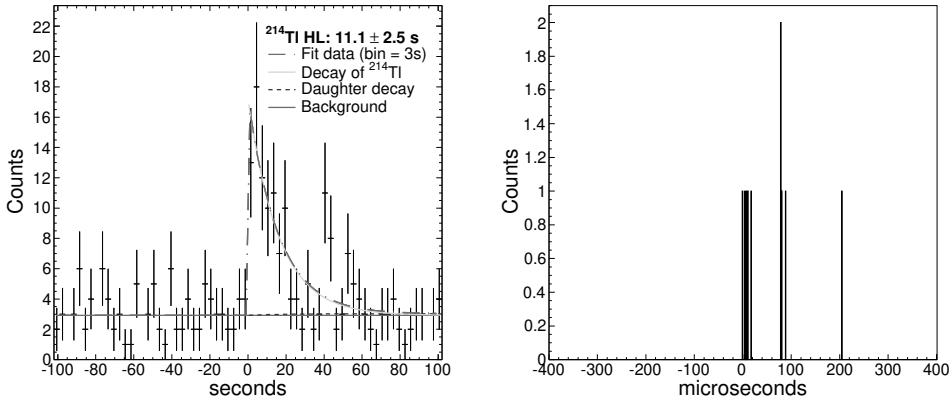

Figure 4.10: Left: ^{214}Tl implant-β correlation diagram and the determined half-life. Right: Events of β-neutron correlations inside the ^{214}Tl implant-β correlation time within an area of 9 mm^2.

4.3.3 Analysis of ^{215}Tl and ^{216}Tl

^{215}Tl and ^{216}Tl correspond to the most exotic thallium isotopes implanted in this experiment. Although their statistics are lower than in previous cases, 281 and 99 implants, respectively, using a correlation area of 25 mm^2 around the implants, it became possible to extract their β-decay half-lives. For the case of ^{215}Tl (figure 4.11-left) the resulting half-life is of $T_{1/2} = 9.7 \pm 3.8$ s. The unique implant-β-neutron correlation detected, gives an upper limit of 9.1 % for the neutron branching ratio.

The analysis of ^{216}Tl yields a half-life of $T_{1/2} = 5.9 \pm 3.3$ s (see figure 4.11-right) and, despite its rather large $Q_{\beta n}$-value of 2230 keV, no single event has been registered neither in the forward nor in the backward implant-β-neutron time-correlation diagrams. Within this information an upper limit of 17.3% has been calculated.

Table 4.2 summarizes the results for all thallium isotopes.

4.4 Lead isotopes: $^{215-218}$Pb

The lead isotopes $^{212-219}$Pb were identified and implanted in this experiment, and particularly $^{214-218}$Pb have good implantation statistics. However, the half-life of ^{214}Pb, 1608±54 s [10], is too long for the presented methodology and instrumentation. The heavier isotopes, $^{215-218}$Pb, could be analyzed reliably, as reported below for the βdecay half-lives. As all their $Q_{\beta n}$ values are negative, neutron branching ratios are not evaluated.

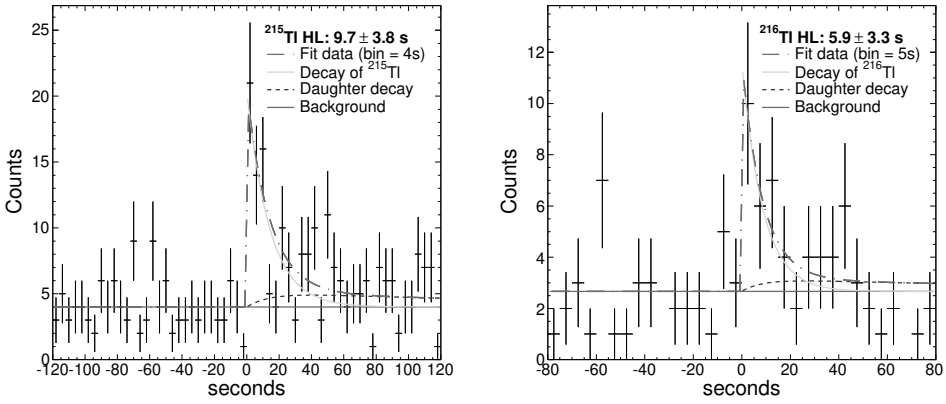

Figure 4.11: Implant-β correlation diagrams of ^{215}Tl (left) and ^{216}Tl (right), using a correlation area of 25 mm^2.

Nuclei	Implanted ions	$t_{1/2}^{exp}$(s)	P_n(%)
^{211}Tl	483	76.5±17.8	<4.4
^{212}Tl	1056	30.9±8.0	<3.7
^{213}Tl	1015	23.8±4.4	7.6±3.4
^{214}Tl	598	11.1±2.5	27.4±10.9
^{215}Tl	281	9.7±3.8	<9.1
^{216}Tl	99	5.9±3.3	<17.3

Table 4.2: Summary of the results obtained for the measured thallium isotopes $^{211-216}$Tl.

4.4.1 Analysis of ^{215}Pb

^{215}Pb has large implantation statistics, 1079 events, and following the method presented in section 4.2, its half-life is of $T_{1/2} = 98.4 \pm 30.7$ s ($\chi^2 = 1.31$). The measured decay curve is shown in figure 4.12.

4.4.2 Analysis of ^{216}Pb by means of two different methods

As detailed in the previous chapter, several α lines were observed in SIMBA. Such transitions correspond to α emitters produced in the decay chain of implanted isotopes. For ^{216}Pb it was also possible to determine its half-life by analyzing the α-decays of a descendant. A similar analysis has been recently reported for ^{215}Pb in [84]. In the present work this approach is possible for the analysis of ^{216}Pb by using the ^{216}Po α-peak at 6778.5 keV.

In order to analyze the implant-α correlation diagram, presented in fig-

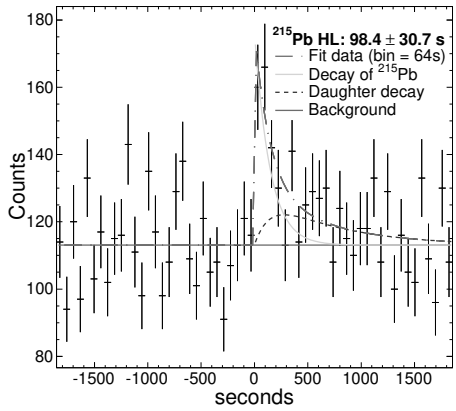

Figure 4.12: ^{215}Pb implant-β correlation diagram showing the contribution from parent (^{215}Tl) and daughter (^{215}Bi) decays.

ure 4.13-left, the Bateman approximation presented in equations (4.1) and (4.5) was used. Although α-particles are emitted by the granddaughter, ^{216}Po, its short half-life ($145\pm2\ ms$) compared with the daughter, ^{216}Bi ($T_{1/2} = 2.25$ minutes), makes the ^{216}Pb implant-α decay curve to be dominated by the decay of ^{216}Bi and ^{216}Pb. The α contribution of the parent decay is negligible, as expected. The resulting half-life, also shown in the same figure is $T_{1/2} = 99.43 \pm 11.69\ s$ ($\chi^2 = 0.74$).

On the other hand, the half-life determined via the conventional implant-β correlation method is obtained from the diagram presented in figure 4.13-right, which yields of $T_{1/2} = 99.44 \pm 17.52\ s$ ($\chi^2 = 1.34$).

The agreement of both independent results provides confidence on the analysis method used for the rest of nuclei analyzed in this work. In particular, the α-decay has a very clear signature (narrow peak) which is only marginally affected by backgrounds. This statement can be clearly appreciated by comparing figures 4.13-left and right, where the P/B ratios are of 6.2 and 1.1, respectively. Therefore, this good correspondence indicates that the treatment of the β-background in this work is well under control.

4.4.3 Analysis of ^{217}Pb and ^{218}Pb

The implantation statistics are lower than for previous isotopes, 436 for ^{217}Pb and 235 for ^{218}Pb. However, it is still possible to obtain a reliable analysis for the implant-β correlation diagrams. The resulting value for ^{217}Pb is of $T_{1/2} = 19.9\pm5.3\ s$ ($\chi^2 = 1.43$) (figure 4.14-left), and for ^{218}Pb is of $T_{1/2} = 14.8\pm6.8\ s$ ($\chi^2 = 1.34$) (figure 4.14-right).

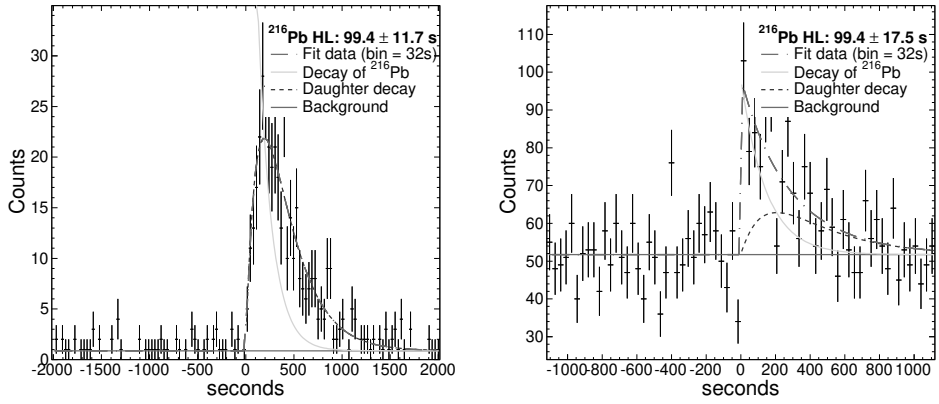

Figure 4.13: Left: Half-life analysis of ^{216}Pb via implant-α correlations. Right: Half-life analysis of ^{216}Pb via implant-β correlations.

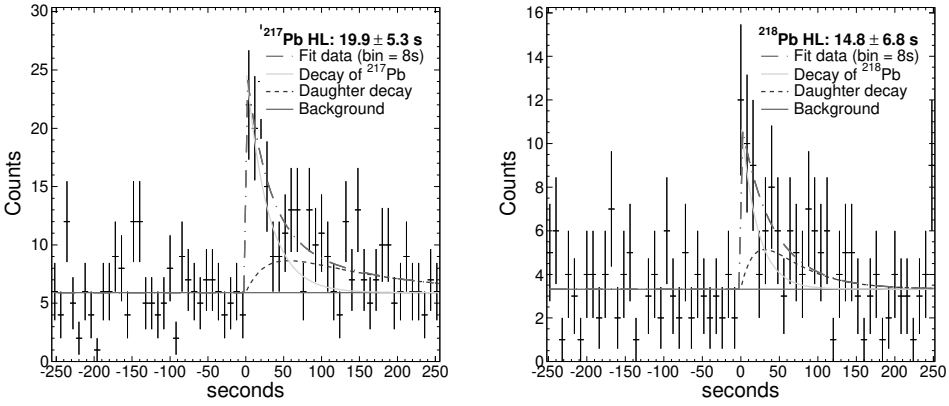

Figure 4.14: Implant-β correlation diagrams for ^{217}Pb (left) and ^{218}Pb (right).

The results obtained for the lead isotopes measured are summarized in table 4.3.

Nuclei	Implanted ions	$t_{1/2}^{exp}$(s)	P_n(%)
^{215}Pb	1079	98.4±30.7	-
^{216}Pb	1005	99.4±11.7	-
^{217}Pb	436	19.9±5.3	-
^{218}Pb	235	14.8±6.8	-

Table 4.3: Summary of the results obtained for the measured lead isotopes $^{215-218}$Tl.

4.5 Mercury isotopes: $^{208-211}$Hg

Eight mercury isotopes have been well identified ($^{206-213}$Hg), four of them, $^{208-211}$Hg, with sufficient statistics for a reliable analysis of the corresponding decay curves.

4.5.1 Analysis of ^{208}Hg

The implant-β correlation diagram for ^{208}Hg is shown in figure 4.15-left. The statistical fluctuations are relatively large due to the limited number of implants (220 events) and the rather long half-life. The Maximum-Likelihood analysis of the decay curve is also shown in the same figure, and yields a value of $T_{1/2} = 132.2 \pm 50.0\ s$ ($\chi^2 = 1.01$).

4.5.2 Analysis of ^{209}Hg

In this case the number of implants is relatively large (583) and the Maximum-Likelihood analysis of the decay curve, shown in figure 4.15-right, provides a rather accurate value (17 % of statistical uncertainty) for the half-life $T_{1/2} = 6.3 \pm 1.1\ s$ ($\chi^2 = 1.33$).

4.5.3 Analysis of ^{210}Hg

In the experiment 512 nuclei of ^{210}Hg were implanted. This has allowed to obtain the implant-β correlation diagram shown in figure 4.16-left, which provides a half-life of $T_{1/2} = 63.7 \pm 11.6\ s$. In the neutron emission analysis, one neutron event has been detected in a time-window of 400 μs with respect to the β-decays. This observation gives an upper limit for the neutron branching of 4.4 %.

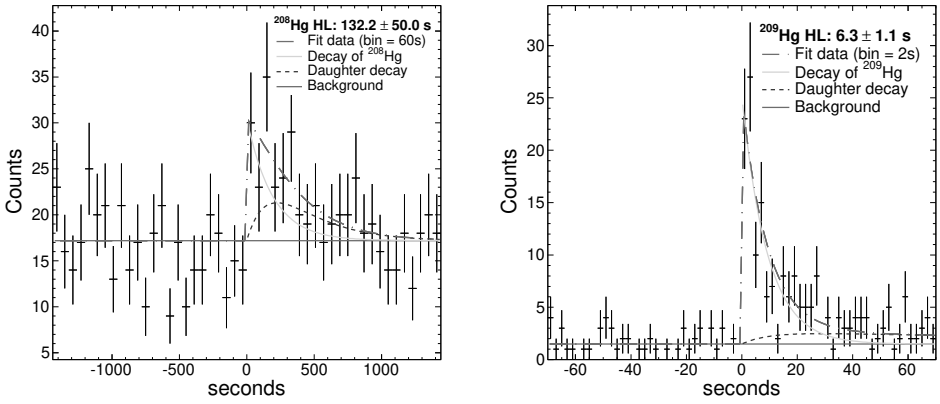

Figure 4.15: ^{208}Hg (left) and ^{209}Hg(right) implant-β correlation diagrams showing the parent and daughter contributions to the measured decay curve.

4.5.4 Analysis of ^{211}Hg

This is the most exotic isotope of mercury implanted with sufficient statistics, 253 events, for a reliable analysis. Taking for the daughter ^{211}Tl, the half-life obtained in section 4.3 of this work, 76.5±17.8 s, the result of the analysis of implant-β correlations is presented in figure 4.16-right, which yields $T_{1/2} = 26.4 \pm 8.1\ s$. Concerning the neutron emission probability P_n, one β-neutron event was measured inside the implant forward correlation time, which yields an upper limit of 12.5 %.

Table 4.4 shows a summary of the decay properties determined in this work for the mercury isotopes.

Nuclei	Implanted ions	$t_{1/2}^{exp}$(s)	P_n(%)
^{208}Hg	220	132.2±50.0	-
^{209}Hg	583	6.3±1.1	-
^{210}Hg	512	63.7±11.6	<4.4
^{211}Hg	253	26.4±8.1	<12.5

Table 4.4: Summary of the results obtained for the measured mercury isotopes $^{208-211}$Hg.

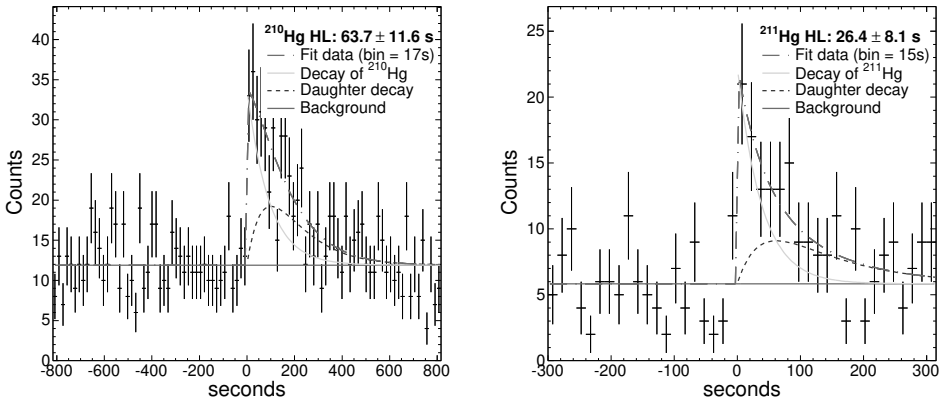

Figure 4.16: Left: ^{210}Hg implant-β correlations showing the contribution to the decay curve of the parent nucleus ^{210}Hg and the daughter ^{210}Tl. Right: Analysis of ^{211}Hg implant-β correlations using a daughter half-life parameter obtained in this work for ^{211}Tl.

4.6 Gold isotopes: $^{204-206}$Au

A total of seven gold isotopes, $^{203-209}$Au, have been identified in this experiment. For the three of them with largest implantation statistics, $^{204-206}$Au, it was possible to determine their half-life. The absence of implant-β-neutron correlations in all cases, was also expected from their negative $Q_{\beta n}$-values.

4.6.1 Analysis of ^{204}Au

For ^{204}Au the number of implanted ions was as small as 54 events. Taking into account this isotope was measured in previous experiments and it can be used to compare the results, in this particular case, although its low statistics implantation, we tried to obtain a decay curve. In figure 4.17-left, the diagram shows that the general equation cannot reproduce a consistent curve. This decay improved slightly when a larger correlation area of 25 mm^2 (instead of 9 mm^2) was used. In addition, it turned out that the correlation with all-β's method, including those detected during the spill time, provides a better sensitivity for the analysis, as shown in figure 4.17-right. The determined half-life is of $T_{1/2} = 33.7 \pm 14.9$ s, using the 25 mm^2 correlation area.

4.6.2 Analysis of ^{205}Au and ^{206}Au

In the case of ^{205}Au and ^{206}Au, despite their low implantation statistics (~ 100 events for each one), the conventional correlation area of 9 mm^2 provided sufficiently good implant-β correlation diagrams to be analyzed. Figures 4.18-

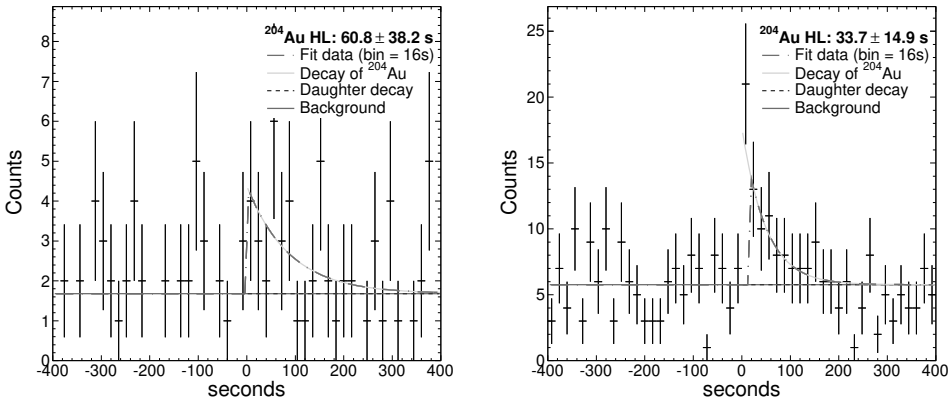

Figure 4.17: ^{204}Au implant-β diagrams. Left: correlation area of 9 mm^2. Right: correlation area of 25 mm^2 and extended with all β-particles including those inside the spill. See text for details.

left (^{205}Au) and 4.18-right (^{206}Au) show the diagrams with the Maximum-Likelihood analysis curves. The resulting half-life values are $T_{1/2} = 35.4 \pm 16.9$ s and $T_{1/2} = 55.7 \pm 16.7$ s, respectively.

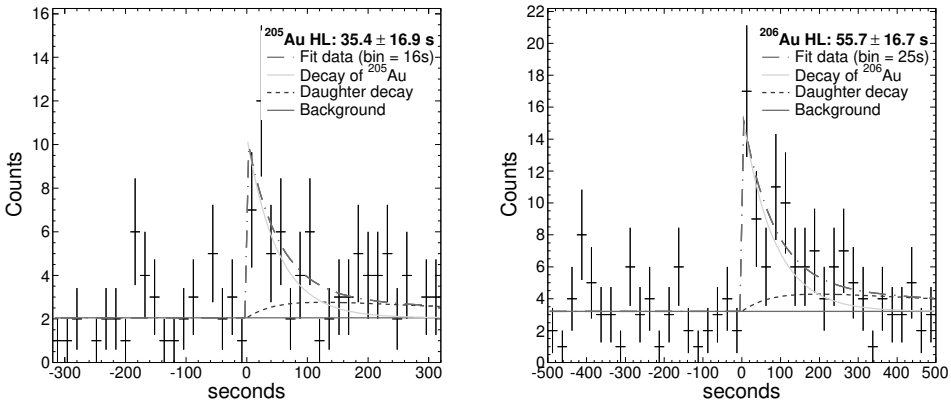

Figure 4.18: ^{205}Au (left) and ^{206}Au (right) implant-β correlation diagrams with the fit of the measured.

Table 4.5 summarizes the properties of these three isotopes obtained in this work.

Nuclei	Implanted ions	$t_{1/2}^{exp}$(s)	P_n(%)
^{204}Au	54	33.7±14.9	-
^{205}Au	103	35.4±16.9	-
^{206}Au	106	55.7±16.7	-

Table 4.5: Summary of the results obtained for the measured gold isotopes $^{204-206}$Au.

4.7 Bismuth isotopes: $^{218-220}$Bi

Bismuth was the heaviest element implanted. In particular nuclei of $^{218-220}$Bi isotopes could be reliably analyzed in terms of statistics. The remarkable isotopes $^{219-220}$Bi have been analyzed with some extra restrictions due to the unknown half-lives of their daughters, $^{219-220}$Po, which have not been determined experimentally yet.

4.7.1 Analysis of ^{218}Bi

For ^{218}Bi the β contribution comes only from its own decay, because its daughter (^{218}Pb) is an α emitter. Figure 4.19 shows the correlation diagram with the half-life value obtained, which is of $T_{1/2} = 38.5 \pm 21.6$ s.

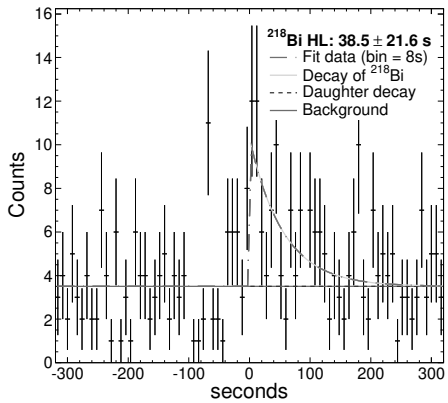

Figure 4.19: ^{218}Bi implant-β correlation diagram with the fit of the analyzed decay curve.

4.7.2 Analysis of ^{219}Bi and ^{220}Bi

In the ^{219}Bi and ^{220}Bi analysis, the value of λ_2 parameter in equation (4.5) is not yet experimentally known. Thus, for the present analysis theoretical predictions from [1] have been employed (17.47 s and 138.47 s for ^{219}Po and ^{220}Po respectively). Figures 4.20-left and 4.20-right show the correlation diagrams for ^{219}Bi and ^{220}Bi, respectively. The obtained results are $T_{1/2} = 3.8 \pm 1.6$ s for the ^{219}Bi and $T_{1/2} = 9.1 \pm 3.4$ s for ^{220}Bi. In these figures it can be also observed that the contribution of the daughter nucleus to the total decay curve is relatively small.

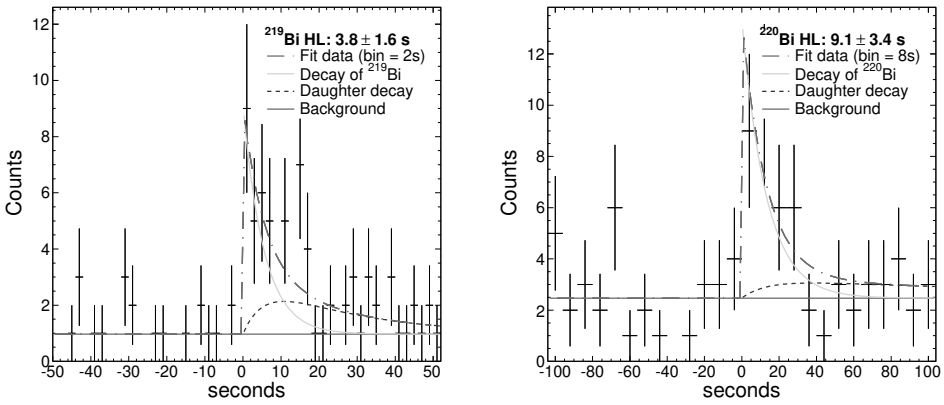

Figure 4.20: ^{219}Bi (left) and ^{220}Bi (right) implant-β correlation diagrams showing the analysis and half-lives obtained by using the decay predictions for the daughter nuclei (^{219}Po and ^{220}Po).

In order to establish a relationship between the half-lives of ^{219,220}Bi and their daughters, several analysis by varying the unknown value of daughters half-life have been done. In figures 4.21-left and -right, it is represented the variation of the half-life for both isotopes as a function of different values of the daughter half-lives. As can be observed it increases up to a plateau when daughters are long lived.

Table 4.6 summarizes the values determined for the properties of the analyzed bismuth isotopes.

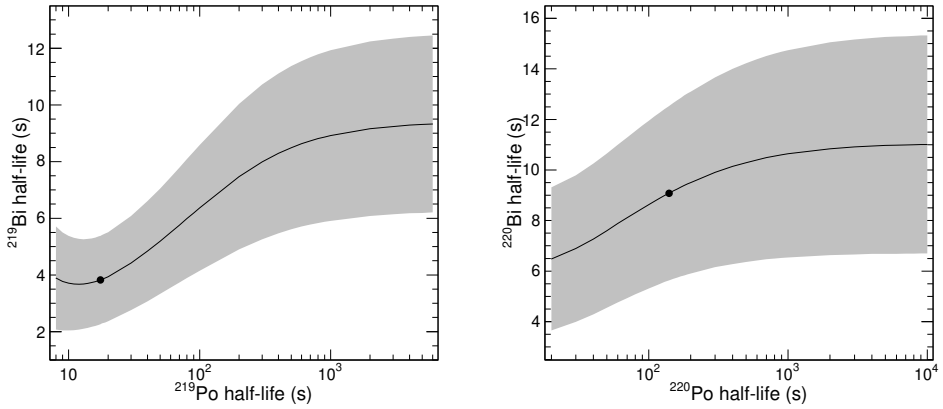

Figure 4.21: ^{219}Bi (left) and ^{220}Bi (right) half-lives, measured by varying the time of unknown daughter half-life in a wide range. In both diagrams are highlighted those analysis using the theoretical predictions.

Nuclei	Implanted ions	$t_{1/2}^{exp}$(s)	P_n(%)
^{218}Bi	294	38.5±21.6	-
^{219}Bi	306	3.8±1.6(*)	-
^{220}Bi	176	9.1±3.4(*)	-

Table 4.6: Summary of the results obtained for $^{218-220}$Bi. (*)Obtained using theoretical values from [1].

Chapter 5
Discussion of the results

The region of interest studied in this work comprises neutron-rich nuclei of five elements: gold, mercury, thallium, lead and bismuth. In addition, as detailed in chapter 2, heavier isotopes of polonium, astatine, radon and francium have also been identified. All these isotopes were previously identified by recent studies performed in 2010 [68] and 2012 [91]. However, only for few of them experimental values of the half-life were known, and the ^{210}Tl is unique isotope with a measured P_n [5].

5.1 Comparison of results with existing references and validation methods

The results reported in the previous chapter can be compared with other published experimental values and the predictions of different theoretical models. The half-lives of half of the analyzed nuclei have been reported in previous experiments, which allows one to compare them. The P_n-values determined in this measurement cannot be compared with any other experimental value, as this is the first time that these nuclei have been measured with a neutron detector. However, the results can be compared with theoretical predictions.

Below, for each element, the particularities observed from our results and the previous reported values are discussed. At the end of this chapter, tables 5.1 and 5.2 summarize the results of this work together with other experimental values and theoretical predictions of FRDM+QRPA [1] and the DF3+cQRPA [92] nuclear models.

5.1.1 Gold isotopes

Half-lives obtained for ^{204}Au and ^{205}Au are fully compatible (see table 5.1) with those reported by previous measurements [93, 94, 95]. In these isotopes the DF3+cQRPA model shows reasonable agreement with experiments. A graphical summary is shown in figure 5.1. In the latter figure and those reported for further elements, the dashed and dotted horizontal lines indicate the statistical uncertainty to the one and two standard deviation level, respectively. The relatively large half-life uncertainties of 30-40% of the present experiment are mainly of statistical origin. Because the main fragment settings were ^{215}Tl and ^{211}Hg, gold isotopes were only marginally implanted (see figure 3.11 and

table 4.5). For the case of ^{206}Au, no experimental values have been reported so far. In this isotope, a surprisingly large half-life is obtained, which is remarkably larger than the value predicted by both theoretical models compared. With this latter result, in future measurements, it would be interesting to study the half-lives beyond ^{206}Au to check the tend of the values and to determine the properties of $N = 126$ waiting point.

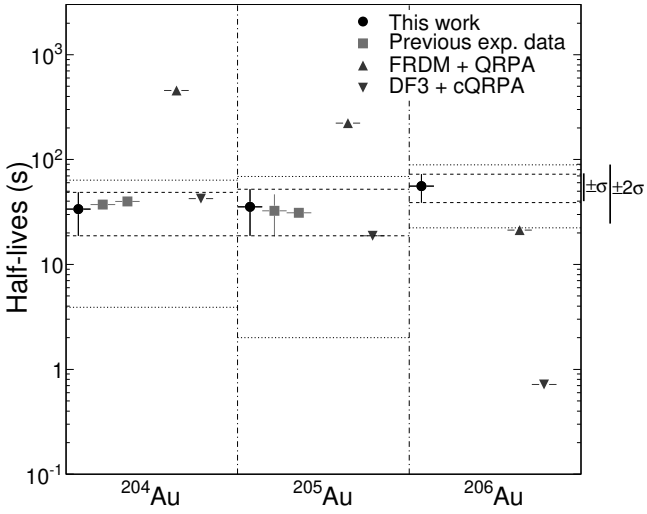

Figure 5.1: $^{204-206}$Au half-life values determined in this work compared with other experimental values and theoretical models published. See text and table 5.1 for details.

5.1.2 Mercury isotopes

The half-life values obtained for ^{208}Hg and ^{209}Hg are about one order of magnitude lower than those reported in literature [96]. This is the largest discrepancy observed between the present experiment and any other experimental work. It is worth noting the generally good agreement of all measured Hg half-life values and the FRDM+QRPA predictions, with the exception of ^{209}Hg. At variance with the measured gold isotopes, the FRDM+QRPA model performs better for the mercury isotopic chain than DF3+cQRPA calculations, also excepting ^{209}Hg. Figure 5.2 shows the results compared with the other referenced values, with ^{210}Hg and ^{211}Hg half-lives reported for the first time.

The upper limits for the P_n-values of ^{210}Hg and ^{211}Hg, and no P_n emission for ^{208}Hg and ^{209}Hg, are compatible with predictions of FRDM+QRPA. The upper limit for ^{211}Hg is also compatible with DF3+cQRPA. Figure 5.3 shows P_n values obtained for mercury isotopes.

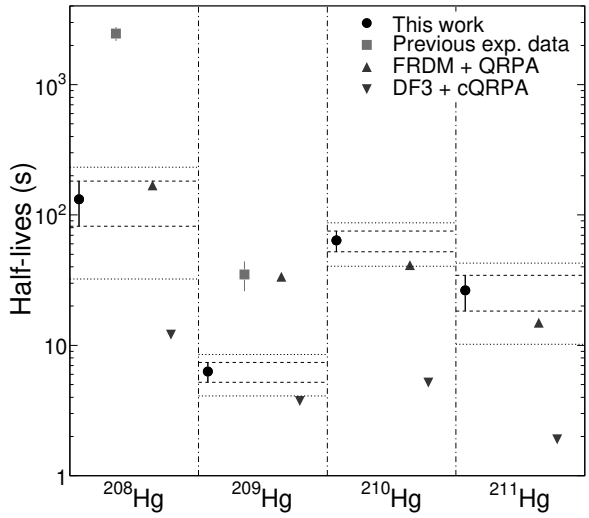

Figure 5.2: $^{208-211}$Hg half-life values determined in this work compared with previous experimental values and theoretical models published. See text and table 5.1 for details.

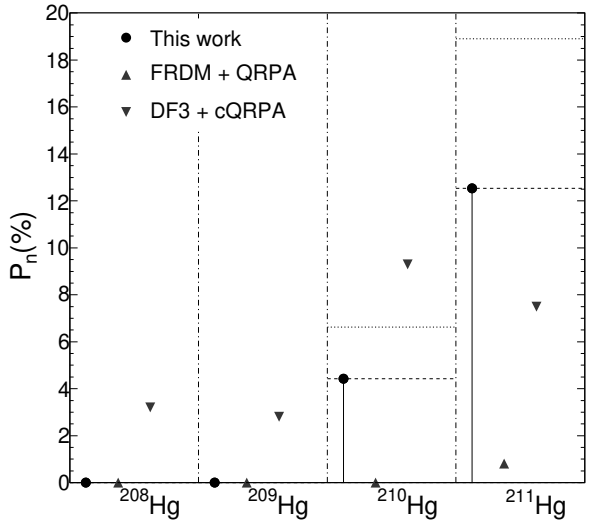

Figure 5.3: Results for the neutron branching ratios of mercury isotopes and the theoretical values reported so far.

5.1.3 Thallium isotopes

From the six half-lives of thallium isotopes measured in this work ($^{211-216}$Tl), $^{211-213}$Tl were also reported before using a similar experimental setup but a fully different analysis approach implemented for high-background conditions [97, 98]. In addition, ^{213}Tl was also measured by using a different experimental technique [69] based in Schottky spectrometry.

For ^{211}Tl, all experimental results are in perfect agreement. On the other hand, the ^{212}Tl and ^{213}Tl half-life values reported here are a factor of 3 and 2 lower, than the previous half-lives [97], respectively. In all cases the uncertainties have been reduced substantially.

It is worth emphasizing the overall rather good agreement for the thallium-chain between the present results and FRDM + QRPA predictions. The statement applies even for the most exotic nuclei reported for the first time, $^{214-216}$Tl. Figure 5.4 and table 5.1 show this comparison and the literature values.

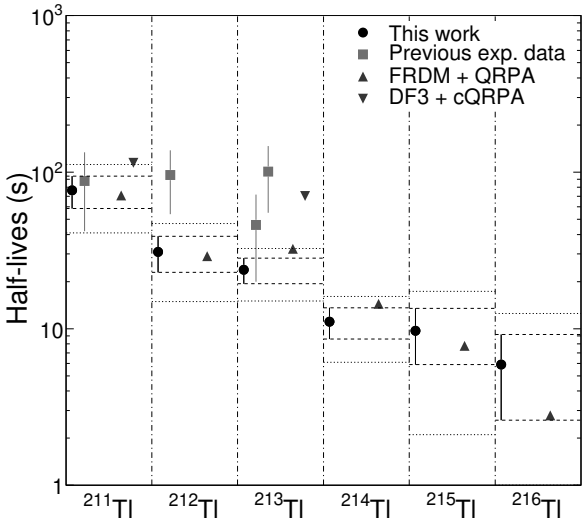

Figure 5.4: $^{211-216}$Tl half-life values determined in this work compared with others previously published from experimental analysis and theoretical models. See text and table 5.1 for details.

Neutron branching ratios have been obtained for ^{213}Tl and ^{214}Tl. The predictions of DF3+cQRPA reports a lower value for ^{213}Tl and FRDM-QRPA overestimates the value for ^{213}Tl and underestimates the one for ^{214}Tl. The large uncertainties provided, around 40%, are due to the low statistics available. In addition to these isotopes, upper limits for ^{211,212}Tl and ^{215}Tl have also been reported, all of them calculated with a single β-neutron event for-

ward correlated. Comparing with theoretical calculations, values reported for ^{211,212}Tl are inside the predicted range, while the most exotic ones, ^{215,216}Tl, present a large discrepancy; FRDM+QRPA estimates P_n-values around 55% and this analysis reports an upper limit lower than 10% for ^{215}Tl. For the case of ^{216}Tl, although the number of detected neutrons is null, assuming the very low statistics, an upper limit of 17.3% is determined considering one neutron event in a further decay. Results and theory values are shown in figure 5.5 and detailed in table 5.2.

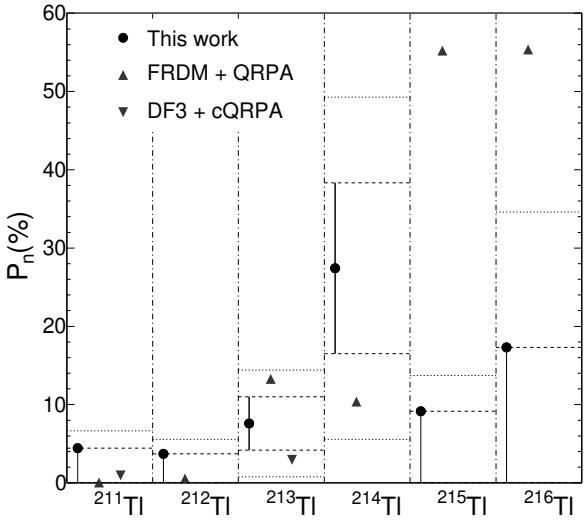

Figure 5.5: Neutron branching ratios obtained compared with predictions of theoretical models.

5.1.4 Lead isotopes

The analysis of lead isotopes allowed three new half-lives for $^{216-218}$Pb and an additional value for the less exotic, ^{215}Pb, which is close with the previous measurements [99, 84]. Comparing with both theoretical models, FRDM+QRPA overestimates the values obtained experimentally by a factor between 3 and 9. For DF3+cQRPA the values are slightly closer to the measured half-lives, however the $^{215-217}$Pb are underestimated with an average deviation of 60%, and ^{218}Pb is overestimated by a factor of 2, see figure 5.6.

Benchmark for the analysis method via ^{216}Pb decay

In the present experiment, the half-life measured for several isotopes can be compared with previous independent values and, in addition, in the case of

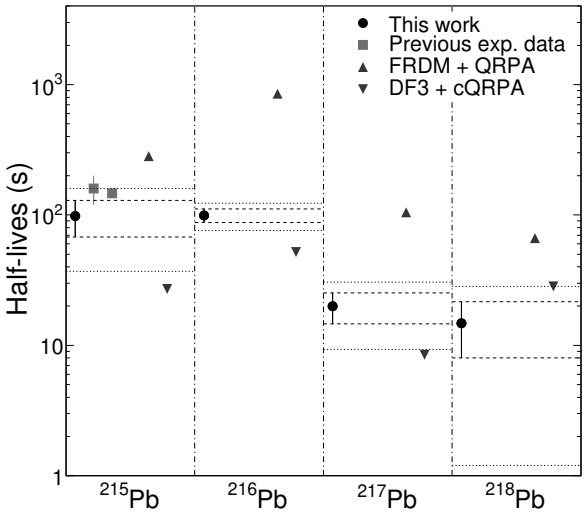

Figure 5.6: $^{215-218}$Pb half-life values determined in this work compared with others previously published from experimental analysis and theoretical models. See text and table 5.1 for details.

^{216}Pb it was possible to determine its half-life by using two independent methods. As detailed in the previous chapter (subsection 4.4.2), the ^{216}Pb half-life can be obtained via the β-decay analysis and by means of the granddaughter ^{216}Po α-peak at 6778.5 keV. Both methods give fully consistent results of $T_{1/2} = 99.44 \pm 17.52$ s and $T_{1/2} = 99.43 \pm 11.69$ s, respectively.

5.1.5 Bismuth isotopes

The results obtained for the bismuth isotopes $^{218-220}$Bi are displayed in figure 5.7. This figure also shows the good agreement with the previous measurements of ^{218}Bi [97], all of them about one order of magnitude higher than FRDM+QRPA predictions.

For the ^{219}Bi our half-life result is in clear discrepancy with both the previous experimental value [97], and theoretical FRDM+QRPA predictions.

Finally, the half-life value obtained for ^{220}Bi in this work appears compatible with the theoretical expectation. It is worth noting that the two half-life values determined for ^{219}Bi and ^{220}Bi have been obtained using the equation (4.5), where the λ_2 parameter is unknown, i.e., no experimental value exists yet for the half-lives of ^{219}Po and ^{220}Po. For this reason, theoretical half-lives from [1] have been employed in the analysis.

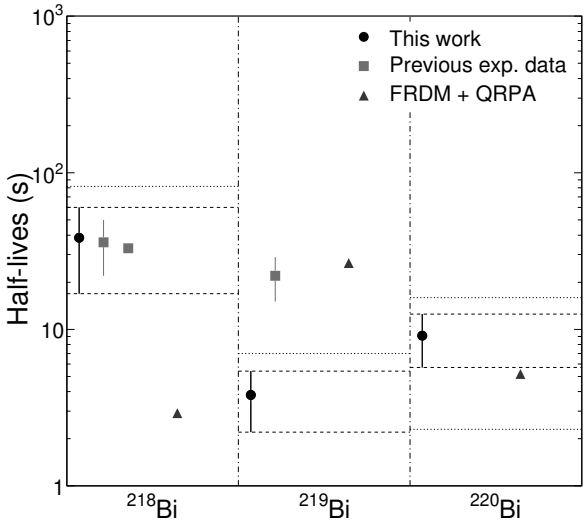

Figure 5.7: Comparison of the ^{218}Bi half-life value determined in this work with other experimental and theoretical values. (*) Estimation of ^{219,220}Bi half-lives by using the half-life of their daughters. See text and table 5.1 for details.

Nuclei	Z	N	$T_{1/2}^{exp}$ (s) (this work)	Previous $T_{1/2}^{exp}$ (s)	FRDM+ QRPA(s) [1]	DF3+ cQRPA(s) [92]
^{204}Au	79	125	33.7 ±14.9	39.8 ±0.9 [93] 37.2 ±0.8 [94]	455.3	42.4
^{205}Au	79	126	35.4 ±16.7	31.0 ±0.2 [95] 32.5 ±14.0 [94]	222.0	18.7
^{206}Au	79	127	55.7 ±16.7	>300 ns	21.3	0.72
^{208}Hg	80	128	132.2 ±50.0	2460^{+300}_{-240} [96]	168.9	12.1
^{209}Hg	80	129	6.3 ±1.1	35.0^{+9}_{-6} [96]	33.6	3.7
^{210}Hg	80	130	63.7 ±11.6	>300 ns	41.2	5.2
^{211}Hg	80	131	26.4 ±8.1	>300 ns	14.9	1.9
^{211}Tl	81	130	76.5 ±17.8	88^{+46}_{-29} [97]	70.9	114.9
^{212}Tl	81	131	30.9 ±8.0	96^{+42}_{-38} [97]	29.0	-
^{213}Tl	81	132	23.8 ±4.4	101^{+486}_{-46} [69] 46^{+55}_{-26} [97]	32.4	70.4
^{214}Tl	81	133	11.1 ±2.5	>300 ns	14.4	-
^{215}Tl	81	134	9.7 ±3.8	>300 ns	7.8	-
^{216}Tl	81	135	5.9 ±3.3	>300 ns	2.8	-
^{215}Pb	82	133	98.4 ±30.7	147 ±12 [99] 160 ±40 [84]	282.5	27.1
^{216}Pb	82	134	99.4 ±11.7	>300 ns	852.2	52.0
^{217}Pb	82	135	19.9 ±5.3	>300 ns	104.9	8.5
^{218}Pb	82	136	14.8 ±6.8	>300 ns	66.3	28.4
^{218}Bi	83	135	38.5 ±21.6	33 ±1 [10] 36 ±14 [97]	2.92	-
^{219}Bi	83	136	3.8 ±1.6*	22 ±7 [97]	26.54	-
^{220}Bi	83	137	9.1 ±3.4*	>300 ns	5.17	-

* Values determined assuming theoretical daughter $T_{1/2}$ from [1].

Table 5.1: Half-lives ($T_{1/2}$) results, previous experimental data and theoretical predictions.

Nuclei	Z	N	P_n(%) (this work)	FRDM+ QRPA(%) [1]	DF3+ cQRPA(%) [92]	Q_{bn} (keV)
^{204}Au	79	125	-	0.0	0.0	-3450 ±200
^{205}Au	79	126	-	0.0	0.0	-2150 ±196
^{206}Au	79	127	-	0.0	0.0	2.00 ±298
^{208}Hg	80	128	-	0.0	3.2	-303 ±31.2
^{209}Hg	80	129	-	0.0	2.8	34 ±149
^{210}Hg	80	130	<4.4	0.0	9.3	201 ±196
^{211}Hg	80	131	<12.5	0.81	7.5	551 ±196
^{211}Tl	81	130	<4.4	0.04	0.95	578 ±41.9
^{212}Tl	81	131	<3.7	0.56	-	869 ±200
^{213}Tl	81	132	7.6 ±3.4	13.26	2.93	1250 ±27.1
^{214}Tl	81	133	27.4 ±10.9	10.38	-	1590 ±196
^{215}Tl	81	134	<9.1	55.24	-	2020 ±298
^{216}Tl	81	135	<17.3	55.36	-	2230 ±315
^{215}Pb	82	133	-	0.0	0.0	-2450 ±102
^{216}Pb	82	134	-	0.0	0.0	-2240 ±196
^{217}Pb	82	135	-	0.0	0.0	-1700 ±298
^{218}Pb	82	136	-	0.0	0.0	-1340 ±299
^{218}Bi	83	135	-	0.0	-	-740 ±27.7
^{219}Bi	83	136	-	0.06	-	-148 ±196
^{220}Bi	83	137	-	0.01	-	66.0 ±298

Table 5.2: P_n results compared with theoretical predictions of measured isotopes.

Chapter 6
Conclusions

This PhD work comprises the first measurement and analysis of the decay properties of several nuclei beyond the neutron shell closure N=126. To this aim, the fragment separator (FRS) facility at the GSI heavy ion research center (Germany) was combined with an active stopper (SIMBA), a ^{3}He-based neutron detector (BELEN-30) and an advanced digital data-acquisition system (DDAS). A total of 35 species of exotic nuclei in the neutron rich region from gold to radon were clearly identified. The β-decay half-lives of ^{206}Au, ^{210,211}Hg, $^{214-216}$Tl and $^{216-218}$Pb have been determined for the first time. In addition, new half-life values were obtained for ^{204,205}Au, ^{208,209}Hg, $^{211-213}$Tl, ^{215}Pb and ^{218}Bi, which could be compared with previous experimental data. In general, a good agreement with respect to previous half-life measurements was found, thus allowing for a more complete systematic study of the nuclear decay- and structure-properties in the $N \geq$126 $A \sim$205-220 mass region.

Apart from this new set of half-life values, the main experimental result of the present work concerns the first determination of the heaviest β-delayed neutron emitting isotopes reported so far. The β-delayed neutron emission probability (P_n) has been measured with an uncertainty-level of around 40% for ^{213}Tl and ^{214}Tl. In addition, upper limits for the P_n-value have been determined for ^{210}Hg, ^{211}Hg, ^{211}Tl, ^{212}Tl, ^{215}Tl and ^{216}Tl. Prior to the present results, the only experimental P_n-value available in this mass-region was reported in 1962 for ^{210}Tl [5]. It is worth noting that, apart from the latter value and those reported in the present work, all previous measurements concentrated mainly on fission products, being ^{150}La the heaviest neutron emitter reported before [6].

The half-life results obtained here have been compared on one hand with values of previous measurements, and on the other hand with theoretical predictions based on FRDM+QRPA [1] and DF3+cQRPA [21] models. Concerning the β-decay half-life values, FRDM+QRPA calculations provide a reasonable agreement for ^{208}Hg,^{210,211}Hg and $^{211-216}$Tl, whereas large deviations are found for ^{209}Hg and the isotopes of gold, lead and bismuth analyzed. In some particular cases, such as ^{204,205}Au and ^{216}Pb, this discrepancy reaches a factor of 10. DF3+cQRPA predictions are available only for some of the measured nuclei, being the agreement good for ^{204,205}Au, and again discrepancies of up to a factor of 10 for ^{211}Hg or 100 for ^{206}Au. The measured neutron branching ratios can be compared with FRDM+QRPA calculations, and some available values for the more recent DF3+cQRPA model. It is worth emphasizing the

case of ^{213}Tl, which is overestimated with a factor of 2 for FRDM+QRPA and underestimated by 2 for DF3+cQRPA. For ^{214}Tl, FRDM+QRPA underestimates a factor 3 the measured P_n. On the other hand, the 55.24% P_n-value predicted for ^{215}Tl is far above our measured upper limit of 9.13%. This effect probably reflects an overestimation of the β-strength distribution towards high excitation energies in the FRDM+QRPA model.

Finally, the "gross" decay-properties determined here are of interest for astrophysical nucleosynthesis studies aiming at identifying the site and environment conditions of the rapid neutron-capture process (r-process). Recent nucleosynthesis studies based on long-term hydrodynamical evolution of supernova explosions [44] have difficulties to reproduce the observed solar system r-process abundances in the region around N=126, which has been the focus of research in the present work. It is expected that the results reported here will help to guide theoretical models in the heavy mass region far from stability. In turn, improved models can be more reliably applied to r-process model calculations in order to mitigate the impact of the uncertainties in the nuclear physics input. With the advent of the new generation of radioactive ion beam facilities such as FAIR-NUSTAR (Germany) or GANIL-SPIRAL2 (France), one can expect that future similar experimental studies will provide additional information, closer to the r-process path at N=126.

Appendix A

^{205}Bi isomeric γ level scheme

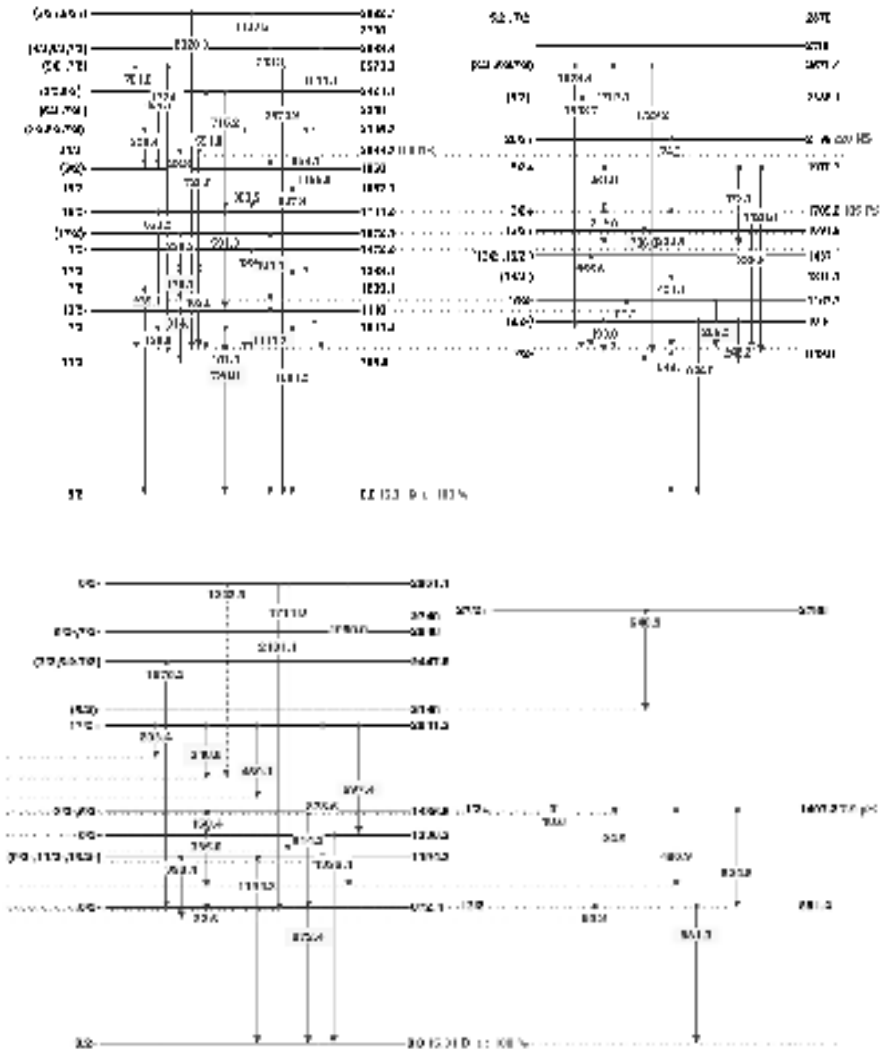

Detected γ's in figure 2.13-right are highlighted. Information from [10].

Appendix B

Consistency study of the tracking detectors values via detector correlations

In order to avoid artifacts in the PID due to instrumental limitations such as pile-up, response saturation, non-linearity regimes and edge effects, the inter-consistency of the response function of the tracking detectors was investigated. To this aim, specific correlation diagrams are built and analyzed for the position, time-of-flight and ΔE measurements. The four diagrams presented below show some examples of correlation between these quantities and calculated parameters. They allow to implement graphical selections according to coherent detection in the region of nuclei of interest and this implies an improvement in terms of background which in turn to disregard wrongly identified ions. The examples in the presented are:

- Top-left: Correlation of the time-of-flight (t_{TOF}) measured in both sides of the beam line between *sci*21 and *sci*41. The selected ions correspond to those events with a compatible t_{TOF} in the left and in the right photomultipliers.
- Top-right: Correlation between the energy loss ΔE at MUSIC 1 and the measured t_{TOF}. The selected events correspond to the region of nuclei of interest. Fission fragments can be appreciated on the left side and t_{TOF} variations along the range.
- Bottom-left: Correlation between the energy loss ΔE at MUSIC 1 and calculated charge with equation (2.7). The selection is according to good events in the region of interest, which corresponds to the calibrated zone.
- Bottom-right: Coherent position selection between two TPC's. Example for X axis at S4. Saturated signals of events for one TPC of them and edge effects can be observed.

Correlation between the response of different FRS tracking detectors. Selection of the coherent events.

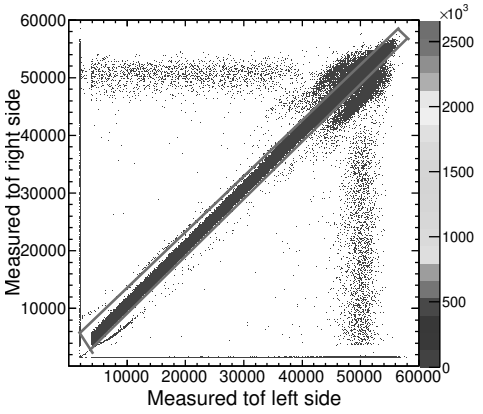
Measured tof right side
Measured tof left side
×10^3

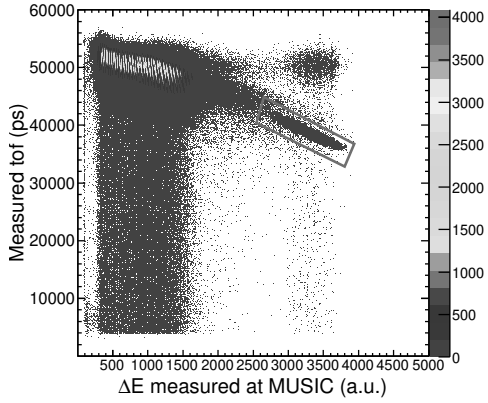
Measured tof (ps)
ΔE measured at MUSIC (a.u.)

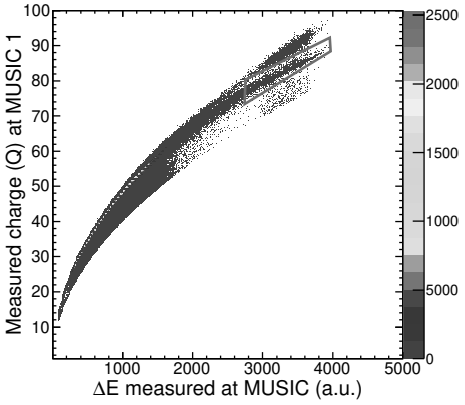
Measured charge (Q) at MUSIC 1
ΔE measured at MUSIC (a.u.)

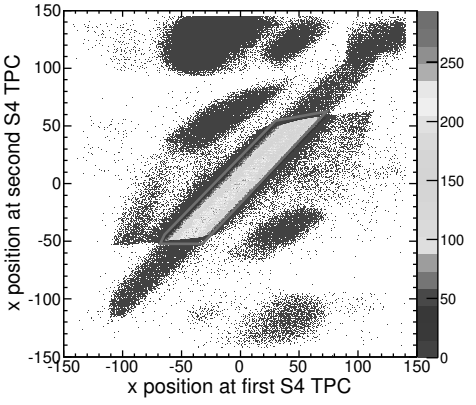
x position at second S4 TPC
x position at first S4 TPC

Appendix C

During the period in which this thesis has been realized, several international meetings and conferences have been attended to disseminate the work to the community, via talks, posters and publications.

Publications: Articles and Conference Proceedings

Published articles, documents and conference proceedings related to the experiments I participated are listed below:

Main publications

- R. Caballero-Folch, C. Domingo-Pardo, G. Cortès, J.L. Taín, J. Agramunt, et al. β-decay and β-delayed Neutron Emission Measurements at GSI-FRS Beyond N=126, for r-process Nucleosynthesis. *Nuclear Data Sheets*, Volume 120, June 2014, Pages 81-83. doi:10.1016/j.nds.2014.07.012

- C. Domingo-Pardo, R. Caballero-Folch, et al. Approaching the precursor nuclei of the third r-process peak with RIBs. *Nuclear Physics in Astrophysics VI*, NPA VI, Lisbon 2013, May 19-24, 2013. Conference Proceedings arXiv:1309.3047v2

- R. Caballero-Folch, C. Domingo-Pardo, J. L. Taín, G. Cortès, J. Agramunt, et al. β-delayed neutron emission measurements around the third r-process abundance peak. *AIP Conference Proceedings.* 1541, 137 (2013); Conference date: 9-13 September 2012. Location: La Rábida, Spain. dx.doi.org/10.1063/1.4810816

- R. Caballero-Folch, C. Domingo-Pardo, J. L. Taín, G. Cortès, J. Agramunt, et al. β-delayed neutron emission measurements around r-process peak. *Proceedings of the XII International Symposium on Nuclei in the Cosmos (NIC XII).* August 5-12, 2012. Cairns, Australia. ISBN 1824-8039. Published online at: http://pos.sissa.it/archive/conferences/146/109/NIC XII 109.pdf

- R. Caballero-Folch, et al. Measurement of β-delayed neutrons around the third r-process peak. *GSI Scientific report 2013* pp. 102. doi:10.15120/GR-2014-1-NUSTAR-FRS-05

- Caballero-Folch R. Experimental determination of the activity of a ^{252}Cf source. *Master thesis work.* Màster en Enginyeria en Energia. EUETIB UPC, 2011.

- J. Kurcewicz, et al. Discovery and cross-section measurement of neutron-rich isotopes in the element range from neodymium to platinum with the FRS. *Physics Letters B*, Volume 717 - 4-5, 31 October 2012, Pages 371-375. ISSN 0370-2693. doi:10.1016/j.physletb.2012.09.021.

- D. Jordan, J.L. Taín, et al. Measurement of the neutron background at the Canfranc Underground Laboratory LSC. *Astroparticle Physics*, Volume 42, February 2013, Pages 1-6. ISSN 0927-6505. doi:10.1016/j.astropartphys.2012.11.007

Other publications

- J. Agramunt, J.L.Taín, et al. New Beta-delayed Neutron Measurements in the Light-mass Fission Group. *Nuclear Data Sheets*, Volume 120, June 2014, Pages 74-77. doi:10.1016/j.nds.2014.07.010

- A. Algora, E. Valencia, et al. Total Absorption Study of Beta Decays Relevant for Nuclear Applications and Nuclear Structure. *Nuclear Data Sheets*, Volume 120, June 2014, Pages 12-15. doi:10.1016/j.nds.2014.06.129

- E. Valencia, A. Algora, et al. Gamma neutron competition above the neutron separation energy in delayed neutron emitters. International Nuclear Physics Conference (INPC) 2013. *EPJ Web of Conferences* 66, 02002 (2014). dx.doi.org/10.1051/epjconf/20146602002

- A.-A. Zakari-Issoufou, A. Porta, M. Fallot, A. Algora, et al. Results of fission products β-decay properties measurement performed with a total absorption spectrometer. International Nuclear Physics Conference (INPC) 2013. *EPJ Web of Conferences* 66, 10019 (2014). dx.doi.org/10.1051/epjconf/20146610019

- A.-A. Zakari-Issoufou, et al. Measurement of fission products β-decay properties using a total absorption spectrometer. Fission 2013 - Fifth International Workshop on Nuclear Fission and Fission Product Spectroscopy. *EPJ Web of Conferences* 62, 01007 (2013). dx.doi.org/10.1051/epjconf/20136201007

- A.-A. Zakari-Issoufou, A. Algora, et al. The Total Absorption Spectroscopy technique for reactor technology and basic nuclear physics. *Nuclear Science Symposium and Medical Imaging Conference (NSS/MIC)*,

2013 IEEE. Seoul (2013). Print ISBN:978-1-4799-0533-1. doi:10.1109/NSSMIC.2013.6829546

- E. Valencia, A. Algora, et al. Total absorption γ-ray spectroscopy of beta delayed neutron emitters. *AIP Conference Proceedings* 1541, 161 (2013); La Rbida 2012, International Scientific Meeting on Nuclear Physics. La Rbida (Spain). Conference date: 9-13 September 2012. dx.doi.org/10.1063/1.4810827

- M.B. Gómez-Hornillos, J. Rissanen, J.L. Taín, et al. β-delayed neutron emission studies. *Hyperfine Interactions*, January 2014, Volume 223, Issue 1-3, pp 185-194. Print ISSN 0304-3843 (2014). Online ISSN 1572-9540 (2012). doi:10.1007/s10751-012-0617-4

- M.B. Gómez-Hornillos, V.Gorlychev, J.L.Taín, et al. Monte Carlo simulations for the study of a moderated neutron detector. *Journal of the Korean Physical Society.* 59(23), pp. 1573 - 1576 (2011). ISSN 0374-4884. Proceeding of the International Conference on Nuclear Data for Science and Technology 2010. Jeju island, Korea.

- J.L. Tain, et al. Beta Decay Studies of Neutron Rich Nuclei Using Total Absorption Gamma-ray Spectroscopy and Delayed Neutron Measurements. *Journal of the Korean Physical Society.* 59 (23), pp. 1499 - 1502 (2011). ISSN 0374-4884. Proceeding of the International Conference on Nuclear Data for Science and Technology 2010. Jeju island, Korea. doi: 10.3938/jkps.59.1499

- M.B.Gómez-Hornillos, J.Rissanen, J.L.Taín, et al. First Measurements with the BEta deLayEd Neutron Detector (BELEN-20) at the JYFL Penning Trap. *Journal of Physics: Conference Series. pp.1-6. IOPScience.* Proceedings of the International Nuclear Physics Conference INCP 2010. TRIUMF - Vancouver, Canada. July 4-9 2010.

Schools of nuclear specific training

Apart of the subjects and lectures related to the nuclear field coursed in the Master in energy engineering, during the thesis period I attended several schools focused in nuclear technologies and astrophysics:

- XVII Euroschool on Exotic Beams 2010. USC, Santiago de Compostela, Spain (2010).

- FRS Training (LISE & MOCADI), GSI. Darmstadt, Germany (2010).

- MCNP and the Monte Carlo Method course, Assistance on the Master on Nuclear Engineering, UPC, Barcelona, Spain (2012).

- ANU Satellite school of Nuclei in the Cosmos School, Australian National University (ANU), Canberra, Australia (2012).
- La Rábida 2012, International Scientific Meeting on Nuclear Physics, La Rábida, Spain (2012).
- Satellite School of The Origin of Cosmic Elements Past and Present Achievements, Future Challenges Conference. Space Studies Institute of Catalonia (IEEC). Barcelona, Spain (2013).

Experiments and collaborations

- Test of the first prototype of Beta delayed neutron (BELEN) detector. UPC laboratory, Barcelona, Spain (2009).
- First experiment with BELEN-20 detector measuring beta delayed neutron emitters in the neutron-rich region (^{88}Br,^{94,95}Rb,^{138}I). JYFL facility at Jyväskylä University, Finland (2009).
- Beta decay studies of neutron rich nuclei using total absorption gamma-ray spectroscopy and delayed neutron measurements at JYFL facility (^{87,88}Br, ^{93,94}, ^{138}I). Jyvskyl University, Finland (2009).
- Measurement of beta delayed neutron emitters with an update of BELEN-20 detector (^{85,86}Ge ^{85}As ^{88,91}Br ^{137}I ^{95}Rb). JYFL facility at Jyväskylä University, Finland (2010).
- Neutron background test at GSI S4 experimental hall with 3He counters. GSI, Darmstadt, Germany (2010).
- S392 collaboration experiment at GSI. GSI, Darmstadt, Germany (2010).
- Neutron Background measurements at LSC (Underground Laboratory of Canfranc) with CUNA collaboration. Laboratorio Subterrneo de Canfranc, Canfranc, Spain (2011).
- S323 & S410 (main experiment of PhD) GSI experiments. Measurements on different neutron rich regions (N 82 & N 126). Experimental determination of beta decay half-lives and beta delayed neutron emission branching properties. GSI, Darmstadt, Germany (2011).
- BELEN detector calibration measurements. PTB, Braunschweig, Germany (2013).
- I162 & I181 experiments at IGISOL facility with BELEN detector. JYFL, Jyväskylä, Finland (2014).

Bibliography

[1] P. Möller, B. Pfeiffer, and K-L. Kratz. New calculations of gross β-decay properties for astrophysical applications: Speeding-up the classical r-process. *Physical Review C*, 67(5):055802, 2003.

[2] Henri Becquerel. Sur les radiations émises par phosphorescence. *Comptes rendus hebdomadaires des séances de l'Académie des sciences*, 122(1):420–421, 1896.

[3] Jochen Erler, Noah Birge, Markus Kortelainen, Witold Nazarewicz, Erik Olsen, Alexander M Perhac, and Mario Stoitsov. The limits of the nuclear landscape. *Nature*, 486(7404):509–512, 2012.

[4] L.I.Rusinov A.V.Kogan. Neutron emission by excited rad nuclei. *Soviet Phys. JETP*, 5:365, 1957.

[5] G. Stetter. Investigation of the Decay of Tl-210 (RaC) Abstr. 10963 Nucl. In *Sci. Abstr*, volume 16, page 1409, 1962.

[6] B. Pfeiffer, K-L. Kratz, and P. Möller. Status of delayed-neutron precursor data: Half-lives and neutron emission probabilities. *Progress in Nuclear Energy*, 41(1):39–69, 2002.

[7] B. Pritychenko, E. Běták, M.A. Kellett, B. Singh, and J. Totans. The Nuclear Science References (NSR) database and Web Retrieval System. *Nuclear Instruments and Methods in Physics Research Section A: Accelerators, Spectrometers, Detectors and Associated Equipment*, 640(1):213–218, 2011.

[8] R.B. Roberts, R.C. Meyer, and P. Wang. Further observations on the splitting of uranium and thorium. *Physical Review*, 55(5):510, 1939.

[9] Niels Bohr and John Archibald Wheeler. The mechanism of nuclear fission. *Physical Review*, 56(5):426, 1939.

[10] National Nuclear Data Center (NNDC), Evaluated Nuclear Structure Data. *Brookhaven National Laboratory, USA*.

[11] R.E. Azuma, K.L. Kratz, H.L. Ravn, S. Mattsson, W. Ziegert, A. Schröder, B. Jonson, L.C. Carraz, H. Ohm, P.G. Hansen, et al. First

observation of beta-delayed two-neutron radioactivity. *Phys. Rev. Lett.*, 43(CERN-EP-79-98):1652–1654, 1979.

[12] M.J.G. Borge. Beta-delayed particle emission. *Physica Scripta*, 2013(T152):014013, 2013.

[13] K. Miernik, K.P. Rykaczewski, C.J. Gross, R. Grzywacz, M. Madurga, D. Miller, J.C. Batchelder, I.N. Borzov, N.T. Brewer, C. Jost, et al. Large β-delayed One and Two Neutron Emission Rates in the Decay of ^{86}Ga. *Physical review letters*, 111(13):132502, 2013.

[14] P.L. Reeder, R.A. Warner, T.R. Yeh, R.E. Chrien, R.L. Gill, M. Shmid, H.I. Liou, and M.L. Stelts. Beta-delayed two-neutron emission from/sup 98/rb. *Phys. Rev. Lett.;(United States)*, 47(7), 1981.

[15] B. Jonson. Proceedings of the 4th international conference on nuclei far from stability, helsingør, 1981. 1981.

[16] C.L. Duke, P.G. Hansen, O.B. Nielsen, G. Rudstam, Isolde Collaboration, et al. Strength-function phenomena in electron-capture beta decay. *Nuclear Physics A*, 151(3):609–633, 1970.

[17] P. Möller, J.R. Nix, and K-L. Kratz. Nuclear properties for astrophysical and radioactive-ion-beam applications. *Atomic Data and Nuclear Data Tables*, 66(2):131–343, 1997.

[18] P. Möller. Nuclear ground-state masses and deformations. *Atomic Data and Nuclear Data Tables*, 59(2):185 – 381, 1995.

[19] Kohji Takahashi and Masami Yamada. Gross theory of nuclear β-decay. *Progress of Theoretical Physics*, 41(6):1470–1503, 1969.

[20] Kohji Takahashi. Gross theory of first forbidden β-decay. *Progress of Theoretical Physics*, 45(5):1466–1492, 1971.

[21] I.N. Borzov. Gamow-Teller and first-forbidden decays near the r-process paths at N= 50, 82, and 126. *Physical Review C*, 67(2):025802, 2003.

[22] I.N. Borzov. Beta-decay rates. *Nuclear Physics A*, 777:645–675, 2006.

[23] E.A. McCutchan, A.A. Sonzogni, T.D. Johnson, D. Abriola, M. Birch, and B. Singh. Improving systematic predictions of β-delayed neutron emission probabilities. *Physical Review C*, 86(4):041305, 2012.

[24] K. Miernik. Phenomenological model of β-delayed neutron-emission probability. *Physical Review C*, 88(4):041301, 2013.

[25] Q. Zhi, E. Caurier, J.J. Cuenca-García, K. Langanke, G. Martínez-Pinedo, and K. Sieja. Shell-model half-lives including first-forbidden contributions for r-process waiting-point nuclei. *Physical Review C*, 87(2):025803, 2013.

[26] Toshio Suzuki, Takashi Yoshida, Toshitaka Kajino, and Takaharu Otsuka. β decays of isotones with neutron magic number of N= 126 and r-process nucleosynthesis. *Physical Review C*, 85(1):015802, 2012.

[27] E.M. Burbidge, G.R. Burbidge, W.A. Fowler, and F. Hoyle. B2FH. *Synthesis of elements in stars," Rev. Mod. Phys*, 29:547–650, 1957.

[28] K. Lodders. Solar system abundances and condensation temperatures of the elements. *The Astrophysical Journal*, 591(2):1220, 2003.

[29] Paul W Merrill. Spectroscopic observations of stars of class. *The Astrophysical Journal*, 116:21, 1952.

[30] Alastair GW Cameron. Origin of anomalous abundances of the elements in giant stars. *The Astrophysical Journal*, 121:144, 1955.

[31] F Sanner. Observations of technetium stars. *The Astrophysical Journal*, 219:538–542, 1978.

[32] C. Freiburghaus, S. Rosswog, and F-K. Thielemann. R-process in neutron star mergers. *The Astrophysical Journal Letters*, 525(2):L121, 1999.

[33] J.J. Cowan and F.K. Thielemann. R-Process Nucleosynthesis in Supernovae. *Physics Today*, pages 47–53, October 2004.

[34] H. Ohm et al. Beta-delayed neutrons and high-energy gamma-rays from decay of ^{137}i. *Zeitschrift für Physik A Hadrons and Nuclei*, 296:23–33, 1980.

[35] K-L Kratz, A Schröder, H Ohm, G Jung, B Pfeiffer, and F Schussler. Observation of beta-delayed neutron decay to excited 0+ states in the residual nucleus: The case 97rb (βnγ) 96sr. *Physics Letters B*, 103(4):305–308, 1981.

[36] K-L. Kratz et al. Beta-delayed neutron emission from ^{93100}rb to excited states in residual sr isotopes. *Zeitschrift für Physik A Hadrons and Nuclei*, 306:239–257, 1982.

[37] H. Gabelmann et al. P_n-values of short-lived sr, y, ba and la precursors. *Zeitschrift für Physik A Hadrons and Nuclei*, 308:359–360, 1982.

[38] J.C. Wang, P. Dendooven, M. Hannawald, A. Honkanen, M. Huhta, A. Jokinen, K-L. Kratz, G. Lhersonneau, M. Oinonen, H. Penttilä, et al.

β-delayed neutron decay of 104 y, 112 tc, 113 tc and 114 tc: test of half-life predictions for neutron-rich isotopes of refractory elements. *Physics Letters B*, 454(1):1–7, 1999.

[39] F. Montes, A. Estrade, P.T. Hosmer, S.N. Liddick, P.F. Mantica, A.C. Morton, W.F. Mueller, M. Ouellette, E. Pellegrini, P. Santi, et al. β-decay half-lives and β-delayed neutron emission probabilities for neutron rich nuclei close to the N= 82 r-process path. *Physical Review C*, 73(3):035801, 2006.

[40] J. Pereira, S. Hennrich, A. Aprahamian, O. Arndt, A. Becerril, T. Elliot, A. Estrade, D. Galaviz, R. Kessler, K-L. Kratz, et al. β-decay half-lives and β-delayed neutron emission probabilities of nuclei in the region a 110, relevant for the r process. *Physical Review C*, 79(3):035806, 2009.

[41] Karl-Ludwig Kratz, Jean-Philippe Bitouzet, Friedrich-Karl Thielemann, Peter Moeller, and Bernd Pfeiffer. Isotopic r-process abundances and nuclear structure far from stability-implications for the r-process mechanism. *The Astrophysical Journal*, 403:216–238, 1993.

[42] Karlheinz Langanke and Hendrik Schatz. The role of radioactive ion beams in nuclear astrophysics. *Physica Scripta*, 2013(T152):014011, 2013.

[43] Karlheinz Langanke and G. Martinez-Pinedo. Nuclear weak-interaction processes in stars. *Reviews of Modern Physics*, 75(3):819, 2003.

[44] A. Arcones and G. Martínez-Pinedo. Dynamical r-process studies within the neutrino-driven wind scenario and its sensitivity to the nuclear physics input. *Physical Review C*, 83(4):045809, 2011.

[45] GSI Helmholtzzentrum für Schwerionenforschung. https://www.gsi.de.

[46] C. Domingo-Pardo et al. Measurement of β-delayed neutrons around the third r-process peak. 2009. GSI-S410 Experiment proposal.

[47] A. Jokinen, T. Eronen, U. Hager, I. Moore, H. Penttilä, S. Rinta-Antila, and J. Äystö. Precision experiments on exotic nuclei at IGISOL. *International Journal of Mass Spectrometry*, 251(2):204–211, 2006.

[48] Juha Äystö. Development and applications of the IGISOL technique. *Nuclear Physics A*, 693(1):477–494, 2001.

[49] M.B. Gómez-Hornillos, J. Rissanen, J.L. Taín, A. Algora, K.L. Kratz, G. Lhersonneau, B. Pfeiffer, J. Agramunt, D. Cano-Ott, V. Gorlychev, R. Caballero-Folch, T. Martínez, L. Achouri, F. Calvino, G. Cortès, T. Eronen, A. García, M. Parlog, Z. Podolyak, C. Pretel, and E. Valencia. β-delayed neutron emission studies. *Hyperfine Interactions*, 223(1-3):185–194, 2014.

[50] J. Agramunt, A.R. Garcia, A. Algora, J. Äystö, R. Caballero-Folch, F. Calvino, D. Cano-Ott, G. Cortes, C. Domingo-Pardo, T. Eronen, et al. New Beta-delayed neutron measurements in the light-mass fission group. *Nuclear Data Sheets*, 120:74–77, 2014.

[51] H. Geissel, P. Armbruster, K.H. Behr, A. Brünle, K. Burkard, M. Chen, H. Folger, B. Franczak, H. Keller, O. Klepper, et al. The GSI projectile fragment separator (FRS): a versatile magnetic system for relativistic heavy ions. *Nuclear Instruments and Methods in Physics Research Section B: Beam Interactions with Materials and Atoms*, 70(1):286–297, 1992.

[52] M. Steiner, K. Blasche, H-G. Clerc, H. Eickhoff, B. Franczak, H. Geissel, G. Münzenberg, K-H. Schmidt, H. Stelzer, and K. Sümmerer. Preliminary measurements of SIS 18 beam parameters. *Nuclear Instruments and Methods in Physics Research Section A: Accelerators, Spectrometers, Detectors and Associated Equipment*, 312(3):420–424, 1992.

[53] A.I. Morales. *β-delayed γ-ray spectroscopy of heavy neutron-rich nuclei produced by cold-fragmentation of ^{208}Pb.* PhD thesis, Universidade de Santiago de Compostela, 2011.

[54] http://www-w2k.gsi.de/frs-setup/ and http://www-w2k.gsi.de/frs/technical/daq/frs-algorithms.asp.

[55] O.B. Tarasov and D. Bazin. LISE++: Radioactive beam production with in-flight separators. *Nuclear Instruments and Methods in Physics Research Section B: Beam Interactions with Materials and Atoms*, 266(19):4657–4664, 2008.

[56] D. Bazin, O. Tarasov, M. Lewitowicz, and O. Sorlin. The program LISE: a simulation of fragment separators. *Nuclear Instruments and Methods in Physics Research Section A: Accelerators, Spectrometers, Detectors and Associated Equipment*, 482(1):307–327, 2002.

[57] Naohito Iwasa, H. Geissel, G. Münzenberg, C. Scheidenberger, Th. Schwab, and H. Wollnik. MOCADI, a universal Monte Carlo code for the transport of heavy ions through matter within ion-optical systems. *Nuclear Instruments and Methods in Physics Research Section B: Beam Interactions with Materials and Atoms*, 126(1):284–289, 1997.

[58] N. Iwasa H. Geissel and H. Weick. MOCADI. 2013.

[59] R. Janik, A. Prochazka, B. Sitar, P. Strmen, I. Szarka, H. Geissel, K-H. Behr, C. Karagiannis, C. Nociforo, H. Weick, et al. Time Projection Chambers with C-pads for heavy ion tracking. *Nuclear Instruments and Methods in Physics Research Section A: Accelerators, Spectrometers, Detectors and Associated Equipment*, 640(1):54–57, 2011.

[60] R. Schneider and A. Stolz. Technical Manual Ionization Chamber MUSIC80. Technical report, Technische Universität München., 2000.

[61] H. Bethe und J. Ashkin. *Experimental Nuclear Physics, ed. E. Segr, J. Wiley, New York*, page 253, 1953.

[62] C. Amsler, M. Doser, M. Antonelli, D.M. Asner, K.S. Babu, H. Baer, H.R. Band, R.M. Barnett, E. Bergren, J. Beringer, et al. Review of particle physics. *Physics Letters B*, 667(1):1–6, 2008.

[63] B. Jäckel, W. Westmeier, and P. Patzelt. On the photopeak efficiency of germanium gamma-ray detectors. *Nuclear Instruments and Methods in Physics Research Section A: Accelerators, Spectrometers, Detectors and Associated Equipment*, 261(3):543–548, 1987.

[64] http://www-win.gsi.de/charms/seetraminfo/seetram2.htm.

[65] E. Casarejos Ruiz. *Measurement and study of the residual nuclides produced in fragmentation reactions of ^{238}U at 1 A GeV with deuterium.* PhD thesis, Universidade de Santiago de Compostela, 2001.

[66] F. Farinon. *Unambiguous identification and investigation of uranium projectile fragments and discovery of 63 new neutron-rich isotopes in the element range 61 less-than or equal to Z less-than or equal to 78 at the FRS.* PhD thesis, Ph.D. thesis, Justus-Liebig-Universitt., 2011.

[67] J. Kurcewicz, F. Farinon, H. Geissel, S. Pietri, C. Nociforo, A. Prochazka, H. Weick, J.S. Winfield, A. Estradé, P.R.P. Allegro, et al. Discovery and cross-section measurement of neutron-rich isotopes in the element range from neodymium to platinum with the FRS. *Physics Letters B*, 717(4):371–375, 2012.

[68] H. Alvarez-Pol, J. Benlliure, E. Casarejos, L. Audouin, D. Cortina-Gil, T. Enqvist, B. Fernández-Domínguez, A.R. Junghans, B. Jurado, P. Napolitani, et al. Production of new neutron-rich isotopes of heavy elements in fragmentation reactions of ^{238}U projectiles at 1 A GeV. *Physical Review C*, 82(4):041602, 2010.

[69] Lixin Chen, W.R. Plass, H. Geissel, R. Knöbel, C. Kozhuharov, Yu. A. Litvinov, Z. Patyk, C. Scheidenberger, K. Siegień-Iwaniuk, B. Sun, et al. Discovery and investigation of heavy neutron-rich isotopes with time-resolved schottky spectrometry in the element range from thallium to actinium. *Physics Letters B*, 691(5):234–237, 2010.

[70] K. Steiger. *Diploma thesis: Effizienzbestimmung des Detektoraufbaus fur die Zerfallsspektroskopie von ^{100}Sn.* PhD thesis, Technische Universität München., 2009.

[71] C.B.Hinke. *Spectroscopy of the doubly magic nucleus ^{100}Sn and its decay.* PhD thesis, Technische Universität München., 2010.

[72] C.B. Hinke, M. Böhmer, P. Boutachkov, T. Faestermann, H. Geissel, J. Gerl, R. Gernhäuser, M. Górska, A. Gottardo, H. Grawe, et al. Super-allowed Gamow-Teller decay of the doubly magic nucleus ^{100}Sn. *Nature*, 486(7403):341–345, 2012.

[73] K.I. Smith. *β-delayed neutron emission studies of neutron-rich Palladium and Silver isotopes.* PhD thesis, Notre Dame, Indiana, 2014.

[74] A. Kastenmüller. 64 Channel Analog Multiplexing Frontend. 1996.

[75] J.C. Santiard, W. Beusch, S. Buytaert, C.C. Enz, E. Heijne, P. Jarron, F. Krummenacher, K. Marent, and F. Piuz. GASSIPLEX, a low noise analog signal processor for readout of gaseous detectors. In *Sixth Pisa Meeting on Advanced Detector, La Biodola, Isola dElba, Italy*, 1994.

[76] V. Gorlychev. *Design of a 4π neutron detector for β-delayed neutron detection experiments.* PhD thesis, Universitat Politcnica de Catalunya, Barcelona (Spain)., 2014.

[77] A. Riego. *Optimization and validation method to design a 4πneutron detector for wide energy range with flat and high detection efficiency.* PhD thesis, Universitat Politcnica de Catalunya, Barcelona (Spain)., In progress.

[78] A. Torner, J. Agramunt, A. Algora, Ll. Batet, R. Caballero-Folch, F. Calviño, D. Cano-Ott, A. García, G. Cortés, I. Dillmann, C. Domingo-Pardo, M.B. Gómez-Hornillos, V. Gorlychev, M. Marta, T. Martínez, A. Poch, C. Pretel, A. Riego, and J.L. Taín. Technical Design Report of the Beta-Delayed Neutron Detector (BELEN) for NUSTAR (DESPEC). Technical report, Universitat Politcnica de Catalunya, Barcelona (Spain)., 2014.

[79] M.B. Gómez-Hornillos, J. Rissanen, J.L. Taín, A. Algora, D. Cano-Ott, J. Agramunt, V. Gorlychev, R. Caballero, T. Martínez, L. Achouri, J. Äysto, G. Cortès, V.V. Elomaa, T. Eronen, A. García, J. Hakala, A. Jokinen, P. Karvonen, V.S. Kolhinen, I. Moore, M. Parlog, H. Penttilä, Z. Podolyak, C. Pretel, M. Reponen, V. Sonnenschein, and E. Valencia. First measurements with the BEta deLayEd Neutron Detector (BELEN-20) at JYFLTRAP. *Journal of Physics: Conference Series*, 312(5):052008, 2011.

[80] JL.Taín et al. Delayed neutron measurements for advanced reactor technologies and astrophysics. 2010. JYFL-I162 Experiment proposal.

[81] I. Dillmann. Measurement of the beta-delayed two-neutron emitter 136sb with the BELEN detector. 2012. JYFL-I181 Experiment proposal.

[82] H.G.Essel N.Kurz. GSI Data Acquisition System MBS, Release Notes v5.1, 2010.

[83] S.Linev J.Adamczewski. http://www-win.gsi.de/go4/.

[84] A.I. Morales, G. Benzoni, A. Gottardo, J.J. Valiente-Dobón, N. Blasi, A. Bracco, F. Camera, F.C.L. Crespi, A. Corsi, S. Leoni, et al. β-decay studies of neutron-rich Tl, Pb, and Bi isotopes. *Physical Review C*, 89(1):014324, 2014.

[85] H. Bateman. *Proc. Camb. Philos. Soc.*, 15(1):423–427, 1910.

[86] M. Bernas, P. Armbruster, J.P. Bocquet, R. Brissot, H. Faust, Ch. Kozhuharov, and J.L. Sida. Beta-decay half-lives of neutron rich Cu and Ni isotopes produced by thermal fission of ^{235}U and ^{239}Pu. *Zeitschrift für Physik A Atomic Nuclei*, 336(1):41–51, 1990.

[87] F.G. Molina Palacios. *Beta Decay of Tz = -1 nuclei and Comparison with Charge Exchange Reaction Experiments*. PhD thesis, IFIC-UV, 2011.

[88] F. Molina, B. Rubio, Y. Fujita, W. Gelletly, J. Agramunt, A. Algora, J. Benlliure, P. Boutachkov, L. Cáceres, R.B. Cakirli, et al. T z=- 1 0 β decays of Ni 54, Fe 50, Cr 46, and Ti 42 and comparison with mirror (He 3, t) measurements. *Physical Review C*, 91(1):014301, 2015.

[89] John G. Proakis, Masoud Salehi, Ning Zhou, and Xiaofeng Li. *Communication systems engineering*, volume 1. Prentice-hall Englewood Cliffs, 1994.

[90] http://root.cern.ch.

[91] L. Chen, W.R. Plaß, H. Geissel, R. Knöbel, C. Kozhuharov, Yu. A. Litvinov, Z. Patyk, C. Scheidenberger, K. Siegień-Iwaniuk, B. Sun, et al. New results on mass measurements of stored neutron-rich nuclides in the element range from Pt to U with the FRS-ESR facility at 360-400 MeV/u. *Nuclear Physics A*, 882:71–89, 2012.

[92] I.N. Borzov. DF3-cQRPA half-lives and Pn-values calculations - priv. communication 2014.

[93] D.A. Craig and H.W. Taylor. Spectroscopy of Gamma Rays from the Decay of ^{202,204}Au. *Journal of Physics*, G10:1133, 1984.

[94] A.I. Morales, J. Benlliure, T. Kurtukián-Nieto, K-H. Schmidt, S. Verma, P.H. Regan, Z. Podolyák, M. Górska, S. Pietri, R. Kumar, et al. Half-life Systematics across the N= 126 Shell Closure: Role of First-Forbidden Transitions in the β Decay of Heavy Neutron-Rich Nuclei. *Physical review letters*, 113(2):022702, 2014.

[95] Ch. Wennemann, W-D. Schmidt-Ott, T. Hild, K. Krumbholz, V. Kunze, F. Meissner, H. Keller, R. Kirchner, and E. Roeckl. Investigation of new neutron-rich gold isotopes ^{203}Au and ^{205}Au. *Zeitschrift für Physik A Hadrons and Nuclei*, 347(3):185–189, 1994.

[96] Zhang Li, Zhao Jinhua, Zheng Jiwen, Wang Jicheng, Qin Zhi, Yang Youngfeng, Zhang Chun, Jin Genming, Guo Guanghui, Du Yifei, et al. Neutron-rich heavy residues and exotic multinucleon transfer. *Physical Review C*, 58(1):156, 1998.

[97] G. Benzoni, A.I. Morales, J.J. Valiente-Dobón, A. Gottardo, A. Bracco, F. Camera, F.C.L. Crespi, A.M. Corsi, S. Leoni, B. Million, et al. First measurement of beta decay half-lives in neutron-rich Tl and Bi isotopes. *Physics Letters B*, 715(4):293–297, 2012.

[98] T. Kurtukian-Nieto, J. Benlliure, and K-H. Schmidt. A new analysis method to determine β-decay half-lives in experiments with complex background. *Nuclear Instruments and Methods in Physics Research Section A: Accelerators, Spectrometers, Detectors and Associated Equipment*, 589(3):472–483, 2008.

[99] H. Sagawa, A. Arima, and O. Scholten. Nuclear compression modulus and isotope shifts of Pb nuclei. *Nuclear Physics A*, 474(1):155–172, 1987.